Multicomponent Crystallization of Energetic Materials

by

Jonathan Caird Bennion

A dissertation submitted in partial fulfillment
of the requirements for the degree of
Doctor of Philosophy
(Chemistry)
in the University of Michigan
2017

Doctoral Committee:

Professor Adam J. Matzger, Chair
Professor Jinsang Kim
Professor E. Neil G. Marsh
Professor John Montgomery

For my parents

Bill and Sheila Bennion.

Acknowledgments

First and foremost, I would first like to thank my research advisor Professor Adam Matzger. He has been a constant source support and encouragement throughout my graduate career. His passion and love for teaching are just a few of the aspects that I truly admire and respect about him. When first given a research project he challenges you to take the topic and shape it into your own idea, and this process has helped to make me into the scientist that I am today. He has devolved a lab atmosphere where we can all have fun and still be productive.

I am also very thankful to my dissertation committee members Professor Jinsang Kim, Professor E. Neil G. Marsh, and Professor John Montgomery for serving on my thesis committee.

I would also like to thank my collaborators in the MURI for providing me with excellent feedback during every monthly meeting. I want to thank Professor Steve Son for his helping with my first manuscript and allowing for me to scale up some of our novel material at Purdue University. I want to especially thank Dr. Leslie Vogt and Professor Mark Tuckerman at New York University, who have helped to provide insight onto the formation of multicomponent materials. I have always been appreciated that Leslie is always willing and eager to accept any challenge that I give her.

I am also very thankful for all members of the Matzger lab, both past and present, for being a source of constant support, guidance and friendship: Laura, Ping, Ananya, Ly, Raj, Yiyang, Preet, Saona, Nipuni, LiZi, Jake, Kortney, Jialiu, Kyle, Cheng, Rosalyn, Ren, Derek, Shantel and

Zohaib. Our lab atmosphere is unlike any other and I will truly miss you all. Thank you to Dr. Antek Wong-Foy for always being there to listen and let me bounce ideas off of him. He has always been willing to assist each and every one of us with any questions or help us to trouble shoot any issues that we run into and I am truly thankful for this. Thank you for keeping the lab light hearted and for the countless lunches that we have shared. Thank you to the former lab members Kira and Onas, who laid the ground work for my project and helped pave the way before me. Thank you to Laura and Ping for being wonderful friends and putting up with my shenanigans in lab. You two are the best brunch dates that I could have asked for. Thank you to Laura who helped to teach me the crystallization and materials science techniques that I needed start my graduate career. I also appreciated our coffee breaks and especially the ones that didn't end where we intended. Thank you to Jake, Jialiu and Cheng for the countless lunches that we shared and the numerous board game nights that ended with Cheng not listening to the rules. Thank you to Raj for being a great deskmate/friend and for our discussion on science and other random topics.

I would also like to thank my friends both in and out of the department: Matt, Paige, Kevin, Cassie, Kyle, BJ, Kortney, Joe, Casey, Laura, Brian, Ty, Andrea, Zheng and Eric. I am thankful to my original friend group at Michigan (Matt, Paige, Kevin, Cassie and Kyle), which has managed to stick together and even grow over the years. I am especially thankful to Matt who was my roommate for all four years of undergrad and two years in grad school, and has been one of my closest friends. I am thankful for the many adventures that we have had over the years and the many more to come. Matt is one of the few people to know what I am thinking without anything needing to be said and I have cherished our friendship. I thank Casey for not only being a good friend, but for putting up with Matt and my sense of humor. Thank you to all of my

roommates (Matt, Zheng, Kevin, BJ and Kyle) over the years and to the countless fun we have had.

And last but certainly not least I am thankful for the love and support of my family. My parents have always supported me and my older brother in whatever we have chosen to pursue and have instilled a determination to succeed. Thank you to mom, dad and Nick, I would not be the person I am without you. Lastly, I must thank my amazing girlfriend Candace. She has been a constant source of support and love while finishing this thesis. She brightens my day every time that we are together.

Table of Contents

Dedication ii
Acknowledgments iii
List of Figures ix
List of Tables xiv
List of Appendices xv
Abstract xvi
Chapter 1: Introduction 1
1.1 Energetic Materials – An overview 1
1.2 Important Properties of Energetic Materials 3
1.3 Methods to Modify Energetic Materials 7
1.4 Multicomponent Crystallization 9
1.5 Multicomponent Energetics in the Literature 11
1.5.1 Multicomponent Materials With Non-Energetic Coformers 11
1.5.2 Multicomponent Energetic-Energetic Materials 12
1.6 Outline of the Thesis 19
1.6.1 Chapter 2: Design and Synthesis of a Series of Nitrogen-Rich Energetic Cocrystals of 5,5'-Dinitro-2H,2H'-3,3'-bi-1,2,4-triazole (DNBT) 19
1.6.2 Chapter 3: Isostructural Cocrystals of 1,3,5-Trinitrobenzene Assembled by Halogen Bonding 19
1.6.3 Chapter 4: Hydrogen Peroxide Solvates of 2,4,6,8,10,12-Hezanitro-2,4,6,8,10,12-Hexaazaisowurtzitane 20
1.7 References 20
Chapter 2: Design and Synthesis of a Series of Nitrogen-Rich Energetic Cocrystals of 5,5'-Dinitro-2H,2H'-3,3'-bi-1,2,4-triazole (DNBT) 25
2.1 Introduction 25
2.2 Results and Discussion 27
2.3 Conclusion 36
2.4 Experimental Procedures 36
2.4.1 Materials 36
2.4.2 Crystallization 37

2.4.3 Raman Spectroscopy 38
2.4.4 Powder X-ray Diffraction (PXRD) 38
2.4.5 Single Crystal Structure Determination 39
2.4.6 Differential Scanning Calorimetry (DSC) 39
2.5 References 40
Chapter 3: Isostructural Cocrystals of 1,3,5-Trinitrobenzene Assembled by Halogen Bonding 43
3.1 Introduction 43
3.2 Results and Discussion 45
3.3 Conclusion 53
3.4 Experimental Procedures 54
3.4.1 Materials 54
3.4.2 Crystallization 54
3.4.3 Raman Spectroscopy 55
3.4.4 Powder X-ray Diffraction (PXRD) 55
3.4.5 Single Crystal Structure Determination 56
3.4.6 Differential Scanning Calorimetry (DSC) 56
3.4.7 Computational Optimization of Molecules and Unit Cells 57
3.5 References 58
Chapter 4: Hydrogen Peroxide Solvates of 2,4,6,8,10,12-Hexanitro-2,4,6,8,10,12-Hexaazaisowurtzitane 63
4.1 Introduction 63
4.2 Results and Discussion 65
4.3 Conclusion 72
4.4 Experimental Procedures 73
4.4.1 Materials 73
4.4.2 Crystallization 73
4.4.3 Raman Spectroscopy 74
4.4.4 Powder X-ray Diffraction (PXRD) 75
4.4.5 Single Crystal Structure Determination 75
4.4.6 Differential Scanning Calorimetry (DSC) 76
4.4.7 Thermogravimetric Analysis (TGA) 76
4.4.8 Drop Weight Impact Sensitivity Analysis 77
4.5 References 77
Chapter 5: Conclusion 80

5.1 Summary of Work..... 80
Appendices..... 83

List of Figures

Figure 1.1 Examples of common energetic materials: a) primary energetics, b) secondary energetics. 2

Figure 1.2 Calculated oxygen balance (OB) values for common energetic materials. 5

Figure 1.3 Examples of insensitive energetic materials. 6

Figure 1.4 Examples of graphite-like sheets formed through strong inter- and intramolecular hydrogen bonding in insensitive energetics: a) 1,3,5-triamino-2,4,6-trinitrobenzene (TATB) and b) 1,1-diamino-2,2-dinitroethene (DADNE/Fox-7). 6

Figure 1.5 Examples of energetics featuring high ring strain. 7

Figure 1.6 Polymorphism: different packing/conformation of the same molecule or compound. Multicomponent crystal formation: a cocrystal is formed between two solid components, whereas a solvate is formed between solid and liquid components. 9

Figure 1.7 Examples of π-effects with an aromatic ring: a) face-to-face, b) slipped stack and c) edge-to-face 11

Figure 1.8 Examples of intermolecular interactions present in the energetic cocrystals formed with non-energetic coformers: a) π-π interactions of TNT/naphthalene, b) C-H···nitro and C-H···S hydrogen bonding in HMX/thieno[3,2-*b*]thiophene, and c) hydrogen bonding in CL-20/dihydrofuran-2(3*H*)-one 12

Figure 1.9 Chemical structure of the pure energetic components for the CL-20 cocrystals. 13

Figure 1.10 Key intermolecular interactions present in the CL-20 cocrystals: a) nitro-π interactions of CL-20/TNT, b) C-H···nitro hydrogen bonding in CL-20/HMX, c) C-H···nitro in CL-20/DNB, and d) nitro-π and C-H···nitro interactions of CL-20/MDNT. 14

Figure 1.11 Chemical structure of the pure energetic components for the BTF cocrystals. 15

Figure 1.12 Key nitro-π interactions present in the BTF cocrystals: a) CL-20/BTF, b) BTF/TNT, c) BTF/TNB, d) BTF/TNA, e) BTF/MATNB, and f) BTF/TNAZ 15

Figure 1.13 Chemical structure of the pure energetic components for the DADP cocrystals. 16

Figure 1.14 Key intermolecular interactions present in the DADP cocrystals: a) peroxy-π interactions of DADP/TCTNB, b) peroxy-π interactions of DADP/TBTNB, and c) iodo-peroxide halogen bonding interactions of DADP/TITNB. 17

Figure 1.15 Chemical structure of the pure energetic components for the DNPP and NTO cocrystals..... 18

Figure 1.16 Key hydrogen bonding interactions between the amines and heterocyclic rings present in the DNPP and NTO cocrystals: a) DNPP/3-AT, b) DNPP/4-AT, and c) DNPP/4-AT. 18

Figure 2.1 Chemical structures of the pure components for each the of three DNBT cocrystals (**1-3**): (a) 2:1 ANTA/DNBT cocrystal (**1**), chemical structures of DNBT and ANTA; (b) 1:1 DNPP/DNBT cocrystal (**2**), chemical structures of DNBT and DNPP; (c) 2:1 3,4-DNP/DNBT cocrystal (**3**), chemical structures of DNBT and 3,4-DNP. 28

Figure 2.2 Typical plate habit morphology of the three DNBT cocrystals (**1-3**): (a) 2:1 ANTA/DNBT cocrystal (**1**); (b) 1:1 DNPP/DNBT cocrystal (**2**); (c) 2:1 3,4-DNP/DNBT cocrystal (**3**). 29

Figure 2.3 Hydrogen bonding motifs utilized in the formation of all three cocrystals **1-3**, all contain three H-bonding interactions between the two respective energetic components in the heterocyclic rings. 31

Figure 2.4 Extended packing of each DNBT cocrystals **1-3**: (a) sheet packing of **1**, 2:1 ANTA/DNBT; (b) herringbone packing of **2** (looking down the c-axis), 1:1 DNPP/DNBT; (c) packing interactions between the most twisted nitro groups of 3,4-DNP in the heterotrimer and the biaryl linkage of DNBT in **3**, 2:1 3,4-DNP/DNBT. 32

Figure 2.5 Packing coefficients (C_k) of each pure component and DNBT cocrystal **1-3**, are calculated from the room temperature (298 K) crystal lattices of each material. 33

Figure 2.6 Detonation velocities of each pure component and DNBT cocrystal **1-3**, are predicted with Cheetah 6.0 software and use the room temperature (298 K) crystallographic densities of each material. 35

Figure 3.1 Electrostatic potential at the molecular surface (ρ=0.002 a.u.) for a) TITNB, b) TBTNB, and c) TCTNB calculated using Density Functional Theory (see Methods for details). The oxygens of the nitro group are shown in red and the halogen atoms (I, Br, and Cl) are shown in blue..... 44

Figure 3.2 Chemical structures of the pure components for both TNB cocrystals **1** and **2**: (a) 2:1 TNB/TITNB cocrystal (**1**), chemical structures of TNB and TITNB; (b) 2:1 TNB/TBTNB cocrystal (**2**), chemical structures of TNB and TBTNB. 46

Figure 3.3 The TNB/TITNB cocrystal. a) Halogen bonding interaction between the nitro and iodine of the coformers. b) Infinite tape of TITNB iodine-nitro interactions in TNB/TITNB. c) Unit cell viewing down the b-axis. 48

Figure 3.4 The TNB/TBTNB cocrystals. a) Halogen bonding interaction between the nitro and bromine of the coformers. b) Infinite tape of TBTNB bromine-nitro interactions in TNB/TBTNB. c) Unit cell viewing down the b-axis. 49

Figure 3.5 DFT-optimized unit cells of 2:1 TNB/TXTNB cocrystals, where X = I (purple), Br (orange), or Cl (green). 50

Figure 3.6 Packing coefficients (C_k) of each pure component and TNB cocrystals **1** and **2**, are calculated from the room temperature (298 K) crystal lattices of each material. 51

Figure 4.1 Chemical structures of the pure components for the CL-20 polymorphic solvates (**1** and **2**): CL-20 and HP. 65

Figure 4.2 Raman spectra (700-1000 cm^{-1}) of α-CL-20, concentrated HP, **1** and **2**. Pure HP O-O peak is at 879 cm^{-1}. 67

Figure 4.3 The 2:1 CL-20/HP orthorhombic solvate (**1**). a) Hydrogen bonding interaction between CL-20 and HP. b) Unit cell viewing down the *a*-axis. c) Typical rhombic habit morphology of the orthorhombic polymorph. 69

Figure 4.4 The 2:1 CL-20/HP monoclinic solvate (**2**). a) Hydrogen bonding interaction between CL-20 and HP. b) Unit cell viewing down the *a*-axis. c) Typical polyhedron habit morphology of the monoclinic polymorph. 69

Figure 4.5 Detonation parameters (velocity and pressure) of ε-CL-20, α-CL-20, **1**, **2**, β-HMX and 2:1 CL-20/HMX are predicted with Cheetah 7.0 using the room-temperature (295 K) crystallographic densities of each material; detonation parameters for **1** at 2.033 g/cm^3 were calculated by extrapolating the detonation velocity vs. density and detonation pressure vs. density squared from the values determined at 99-90% of the crystallographic density given that the theoretical max density (%TMD) maxed out at only 2.013 g/cm^3. 71

Figure A1.1 Raman spectra of **1**, α-ANTA and DNBT (from top to bottom). 83

Figure A1.2 Raman spectra of **2**, DNPP and DNBT (from top to bottom). 84

Figure A1.3 Raman spectra of **3**, 3,4-DNP and DNBT (from top to bottom). 84

Figure A1.4 PXRD patterns of **1**, α-ANTA and DNBT (from top to bottom). 85

Figure A1.5 PXRD patterns of **2**, DNPP and DNBT (from top to bottom). 85

Figure A1.6 PXRD patterns of **3**, 3,4-DNP and DNBT (from top to bottom). 86

Figure A1.7 ORTEP diagram for **1** collected at 85 K with thermal ellipsoids of 50% probability. 86

Figure A1.8 ORTEP diagram for **2** collected at 85 K with thermal ellipsoids of 50% probability. 87

Figure A1.9 ORTEP diagram for **3** collected at 85 K with thermal ellipsoids of 50% probability. 87

Figure A1.10 Typical DSC traces of **1**, ANTA and DNBT (from top to bottom). 88

Figure A1.11 Typical DSC traces of **2**, DNPP and DNBT (from top to bottom). 88

Figure A1.12 Typical DSC traces of **3**, 3,4-DNP and DNBT (from top to bottom). 89

Figure B1.1 Raman spectra of **1**, TITNB, and TNB (from top to bottom). 90

Figure B1.2 Raman spectra of **2**, TBTNB, and TNB (from top to bottom). 91

Figure B1.3 PXRD patterns of **1**, TITNB, and TNB (from top to bottom). 91

Figure B1.4 PXRD patterns of **1** and the simulated structure of **1** from the CIF (from top to bottom). 92

Figure B1.5 PXRD patterns of **2**, TBTNB, and TNB (from top to bottom) 92

Figure B1.6 PXRD patterns of **2** and the simulated structure of **2** from the CIF (from top to bottom). 93

Figure B1.7 ORTEP diagram for **1** collected at 85 K with thermal ellipsoids of 50% probability. 93

Figure B1.8 ORTEP diagram for **2** collected at 85 K with thermal ellipsoids of 50% probability. 94

Figure B1.9 Typical DSC traces of **1**, TITNB, and TNB (from top to bottom). 94

Figure B1.10 Typical DSC traces of **2**, TBTNB, and TNB (from top to bottom). 95

Figure C1.1 Powder patterns of **1** and the simulated structure of **α-CL-20** from the CIF (from top to bottom). 98

Figure C1.2 Powder patterns of **1** and the simulated structure of **1** from the CIF (from top to bottom). 99

Figure C1.3 Powder patterns of **2** and the simulated structure of **2** from the CIF (from top to bottom). 99

Figure C1.4 Full range (100-4000 cm^{-1}) Raman spectra of α-CL-20, **1** and **2** (from bottom to top). 100

Figure C1.5 Zoomed in (100-1650 cm^{-1}) Raman spectra of α-CL-20, **1** and **2** (from bottom to top). Pure HP O-O peak is at 879 cm^{-1}. 100

Figure C1.6 ORTEP diagram for **α-CL-20** collected at 85 K with thermal ellipsoids of 50% probability. 101

Figure C1.7 ORTEP diagram for **1**, orthorhombic, collected at 85 K with thermal ellipsoids of 50% probability. 101

Figure C1.8 ORTEP diagram for **2**, monoclinic, collected at 85 K with thermal ellipsoids of 50% probability. 102

Figure C1.9 Typical DSC traces of α-CL20, **1** and **2** (from bottom to top). 102

Figure C1.10 Typical TGA traces of **1**. 103

Figure C1.11 Typical TGA traces of **2**. 103

List of Tables

Table 1.1 Density and detonation velocity (V_d) values for the four CL-20 polymorphs (α-, β-, γ- and ε-). Detonation velocity is predicted with Cheetah 7.0 using the crystallographic densities... 8

Table 2.1 Crystallographic Data for DNBT Cocrystals (Collected at 85 K) 30

Table 3.1 Crystallographic Data for TNB Cocrystals (Collected at 85 K) 47

Table 4.1 Crystallographic Data for α-CL20 and CL-20 Solvates (Collected at 85 K)..... 76

Table B1.1 Optimized Cell Parameters for TNB Polymorphs..... 96

Table B1.2 Optimized Cell Parameters for TXTNB Crystals..... 96

Table B1.3 Optimized Cell Parameters for TNB/TXTNB Cocrystals..... 97

Table B1.4 Calculated System Energy per Asymmetric Molecule Unit..... 97

List of Appendices

Appendix A: Design and Synthesis of a Series of Nitrogen-Rich Energetic Cocrystals of 5,5'-Dinitro-2H,2H'-3,3'-bi-1,2,4-triazole (DNBT) Supplemental Information 83

Appendix B: Isostructural Cocrystals of 1,3,5-Trinitrobenzene Assembled by Halogen Bonding Supplemental Information..... 90

Appendix C: Hydrogen Peroxide Solvates of 2,4,6,8,10,12-Hexanitro-2,4,6,8,10,12-Hexaazaisowurtzitane Supplemental Information 98

Abstract

Multicomponent crystallization (cocrystallization and solvate formation) offers the unique ability to post-synthetically alter the properties of a materials through noncovalent interactions between two or more molecular components. Significant application of multicomponent crystallization within pharmaceuticals, organic semiconductors, non-linear optical materials has more recently been joined by energetic materials. For energetic compounds, both cocrystallization and solvate formation have been shown to modify critical performance properties such as a materials density, impact/thermal sensitivity, and detonation velocity/pressure. The design and synthesis of multicomponent crystals derived from two energetic components will be discussed with detailed analysis of the crystal structures for each novel energetic and the effect of packing/intermolecular interaction on materials properties. The impact sensitivity of the materials, analyzed through small-scale impact drop tests, will be used to stress the significance of multicomponent crystallization for its ability to design both primary and secondary energetic materials.

In Chapter 1, a series of three energetic cocrystals containing 5,5'-dinitro-2H,2H'-3,3'-bi-1,2,4-triazole (DNBT) were obtained. These incorporate a class of energetic materials that has seen significant synthetic work, the azole family (tetrazoles, triazole, pyrazole, etc.), and yet have struggled to see broad application. A cocrystal was obtained with the triazole 5-amino-3-nitro-1H-1,2,4-triazole (ANTA) in a stoichiometry of 2:1 (ANTA:DNBT). Two cocrystals were obtained with the pyrazoles 1H,4H-3,6-dinitropyrazolo[4,3-c]pyrazole (DNPP) and 3,4-

dinitropyrazole (3,4-DNP) in ratios of 1:1 (DNPP:DNBT) and 2:1 (3,4-DNP:DNBT). All three cocrystals, 2:1 ANTA/DNBT (**1**), 1:1 DNPP/DNBT (**2**), and 2:1 3,4-DNP/DNBT (**3**), have high densities (>1.800 g/cm^3) and high predicted detonation velocities (>8000 m/s). In small-scale impact drop tests cocrystals **1** and **2** were both found to be insensitive, whereas cocrystal **3** possesses sensitivity between that of its two pure components 3,4-DNP and DNBT. The hydrogen bonding motif of the three components with DNBT is preserved among all three cocrystals, and this observation suggests a generally useful motif to be employed in the development of other energetic-energetic cocrystals. These cocrystals represent an area of energetic materials that have yet to be explored for cocrystalline materials.

Chapter 2 describes two isostructural energetic cocrystals containing 1,3,5-trinitrobenzene (TNB) that were obtained with the energetic materials 1,3,5-triiodo-2,4,6-trinitrobenzene (TITNB) and 1,3,5-tribromo-2,4,6-trinitrobenzene (TBTNB) in ratios of 2:1 TNB/TITNB (**4**) and 2:1 TNB/TBTNB (**5**). These materials contain the shortest nitro-iodo and second shortest nitro-bromo interactions seen in the Cambridge Structural Database (CSD) for organohalides. Computational studies indicate that the cocrystals are more stable than their respective component crystals by 11.5 kJ/mol for **4** and 8.2 kJ/mol for **5**. While the formation of an isostructural 2:1 cocrystal with 1,3,5-trichloro-2,4,6-trinitrobenzene (TCTNB) was calculated to be favorable by 8.5 kJ/mol, only a physical mixture of the two coformers was obtained experimentally. Both **4** and **5** possess high crystallographic densities (2.203 and 1.980 g/cm^3 respectively) and were found to be insensitive in small-scale impact drop tests, possessing sensitivity between that of TNB and TXTNB (X = I or Br). The halogen content of the two cocrystals suggests application as insensitive biocidal energetics. Halogen bonding, facilitated by the strong polarization induced by aromatic ring nitration, plays a critical role in the formation of

these cocrystals and offers one of the most promising routes to the development of new energetic cocrystals.

In Chapter 4, two polymorphic hydrogen peroxide (HP) solvates of 2,4,6,8,10,12-hexanitro-2,4,6,8,10,12-hexaazaisowurtzitane (CL-20) were obtained using the hydrated α-CL-20 as a guide. These novel HP solvates have high crystallographic densities (1.96 and 2.03 g/cm^3 respectively), high predicted detonation velocities/pressures (with one solvate possessing greater performance than that of ε-CL-20) and sensitivity similar to that of ε-CL-20. The use of hydrated materials as a guide will be important in the development of other energetic materials with hydrogen peroxide. These solvates represent an area of energetic materials that have yet to be explored.

Chapter 1: Introduction

1.1 Energetic Materials – An overview

The term energetic material describes any organic or inorganic compound or mixture that reacts rapidly to release chemically stored energy within their bonds to create light, heat and gas. In the cases of explosives, these materials combine, generally through covalent bonding, both the fuel (backbone systems) and the oxidizers (-NO_2, perchlorates, etc.) necessary for a detonation to occur. Different from a purely combustible material (i.e. gasoline), energetic materials do not need external oxygen. The general class of energetic materials can be further broken down into three separate categories: explosives, propellants and pyrotechnics. Explosives release energy solely through detonation to provide destructive power for both civilian and military applications. Propellants provide sustained thrust through a burning process known as deflagration. Pyrotechnics, often a combination of both explosive and propellants, are designed to produce an effect such as smoke, light, sound (i.e. signal flares and fireworks). The major difference between explosives and propellants is the speed and duration of the reaction after initiation. A detonation event propagates at supersonic speeds via compression-induced heating of unreacted material by a shock wave, whereas a deflagration event propagates below the speed of sound via burning of unreacted material. An energetic material can be utilized as either an explosive or a propellant depending upon how the material is formulated for a potential application into a munition.

Explosives can be further classified into primary and secondary explosives based upon both the detonation properties (detonation velocity/pressure) and sensitivities to external stimuli (static, heat, impact, friction). Primary explosives are often extremely sensitive to external stimuli, with low to moderate detonation velocities that typically range from 3500-5500 m/s.[1] Some common examples of primary explosives include lead azide (LA), lead styphnate (LS) and copper(I) 5-nitrotetrazolate (DBX-1), see Figure 1.1a.[2] In contrast, secondary explosives are more insensitive to external stimuli and typically require a primary explosive charge to initiate detonation. The performance of secondary explosives is generally greater than that of primary explosives and ranges between 5500-9000 m/s.[1] Some common examples of secondary explosives include 2,4,6-trinitrotoluene (TNT), pentaerythritol tetranitrate (PETN), octahydro-1,3,5,7-tetranitro-1,3,5,7-tetrazocine (HMX) and 2,4,6,8,10,12-hexanitro-2,4,6,8,10,12-hexaazaisowurtzitane (CL-20), see Figure 1.1b.[2] Current research has focused on the development of greener/lead-free primary explosives and secondary explosives that are less sensitive with greater performance.

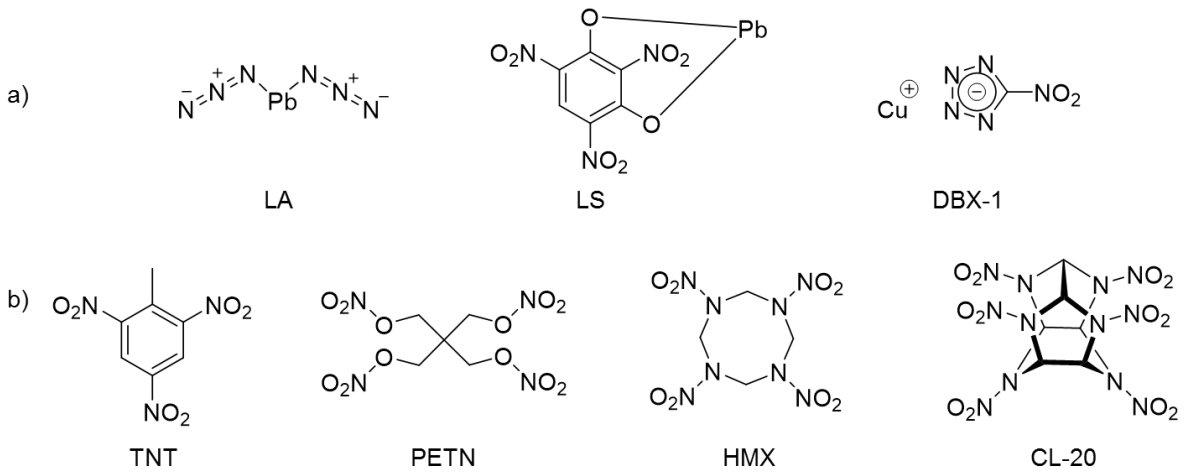

Figure 1.1 Examples of common energetic materials: a) primary energetics, b) secondary energetics.

1.2 Important Properties of Energetic Materials

When designing novel materials for energetic applications important factors to consider prior to implementation are: power, safety and processability. The power of an energetic material arises from a combination of both density and chemical composition (heat of formation, oxygen balance and chemical formula) of the material. The sensitivity of a material to external stimuli not only affects safety in regards to handling, but affects the long term stability of a material, which needs to be maintain its performance ability even over decades of storage. An economical total synthesis is one important factor for an energetic material to be processable on scale, as well as through understanding of the mechanical and thermal properties for formulation and casting. The performance of an energetic material is thus a delicate balance between the safety, the power and the processability.

The power associated with an energetic material is quantified through analysis of both the detonation velocity and pressure. Detonation velocity (V_d), in m/s or km/s, is defined as the rate of propagation of a shock wave through an explosive, while detonation pressure (P_d), in Gpa, is defined as the pressure produced at the shock wave front of an explosive. Both of these properties can be experimentally determined through large scale detonations or theoretically calculated with knowledge of chemical and thermodynamic properties of a novel material. The Kamlet-Jacobs equations have been used for determining these values and they relate the density of the material, number of moles of gas released per gram of energetic and the heat of formation:

$$V_d = 1.01(1 + 1.30\rho_0)\sqrt{N_g\sqrt{M_g Q}} \qquad \text{(Eqn 1.1)}$$

$$P_d = 15.58 p_0^2 N_g \sqrt{M_g Q} \qquad \text{(Eqn 1.2)}$$

For a given energetic: ρ_0 is the loading density (g/cm^3), N_g is the number of moles of gas released per gram, M_g is the mass of gas in gram per mole of gas, and Q is the heat of detonation (cal/g).[3]

As seen in both the detonation velocity and pressure equations, the density of an energetic material plays a significant role in the performance; the V_d increases proportionally and the P_d increases to the power of two based on the loading density. In general, the highest loading density corresponds to the greatest power. It should be noted that the theoretical maximum density (TMD) is achieved through the crystallographic density obtained from single crystal analysis, but the loading density from typical processing methods such as pressing, melt casting, or extruding, cannot typically reach the TMD. To a lesser degree, the performance of an energetic material is also affected by the heat of detonation (Q) of the materials, which is directly dependent on the heat of formation (ΔH_f°) of the molecule (Eqn. 1.3) based on Hess's Law.[2]

$$Q = \Sigma \Delta H_{f\,(detonation\ products)}^\circ - \Sigma \Delta H_{f\,(energetic)}^\circ \qquad \text{(Eqn 1.3)}$$

Another important property to consider with the performance of energetic materials is the oxygen balance (OB) of the system. Oxygen balance is the weight percent of oxygen released as a result of the complete conversion to neutral molecular components (CO_2, H_2O, N_2, etc.) upon detonation.[4] The oxygen balance for an organic material ($C_aH_bN_cO_d$) can be calculated using the following equation:

$$OB = -\frac{1600}{MW}\,(2a + b/2 - d) \qquad \text{(Eqn 1.4)}$$

where a, b, c, and d are the number of carbon, hydrogen, nitrogen and oxygen atoms, respectively, and MW is the molecular weight of the material. A positive OB denotes that there is excess oxygen in the system after full conversion, whereas a negative OB refers to an insufficient amount of oxygen and typically results in the generation of carbon soot and lower oxidized, toxic gases (CO, NO). The more negative the OB, the less gas that is generated from the detonation and as a result, the brisance or shattering effect of the material is diminished.[5, 6] The vast majority of traditional energetic materials possess a negative OB with respect to CO_2:

PETN, (-10%), CL-20 (-11%), HMX (-22%) and TNT (-74%), with nitroglycerin [NG] (+4%) and hexanitroethane [HNE] (+43) being two examples of the few explosives possessing a positive OB, see Figure 1.2. A perfect oxygen balance would be 0%, indicating complete conversion to the neutral molecular components, but is difficult to achieve in practice. The formulation of an energetic with an additional energetic and/or oxidizers allows for a more neutral oxygen balance to be achieved, i.e. closer to 0%.

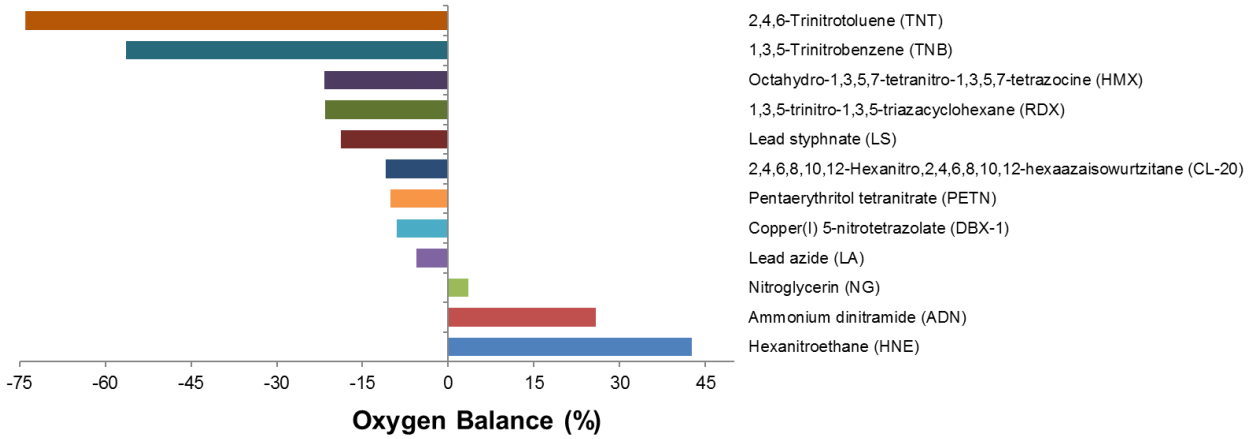

Figure 1.2 Calculated oxygen balance (OB) values for common energetic materials.

The sensitivity influences safety and handling of a material and is affected by factors including the intermolecular and intramolecular bonding interactions and the packing of molecules in the crystal structure. The initiation of an energetic material from an external stimulus is predominantly a thermal process and is thought to occur through the formation of hotspots, small pockets of hot gas, from the presence of crystal defects (cracks, fractures, etc.).[2] Hotspots can be mitigated by strong and extensive inter-/intramolecular bonding between respective molecules, which help to reduce the strain applied to the covalent bonds. A material that possesses high sensitivity to a stimulus, will typically possess weak intermolecular bonds. The packing structure of a molecule in the crystal structure can also play a significant effect in the sensitivity of the material. It has been well studied that materials which form sheet-like or wave-like structures can

reduce hotspot formation through dissipation of thermal energy through slipping of these planes.[7, 8] The insensitivity of an energetic has been associated with the vast network of strong inter- and intramolecular hydrogen bonding in the crystal and the formation of a graphite-like sheets, such is the case with the insensitive energetics 1,3,5-triamino-2,4,6-trinitrobenzene (TATB), 2,6-diamino-3,5-dinitropyrazine-1-oxide (LLM-105) and 1,1-diamino-2,2-dinitroethene (DADNE/Fox-7), see Figure 1.4.

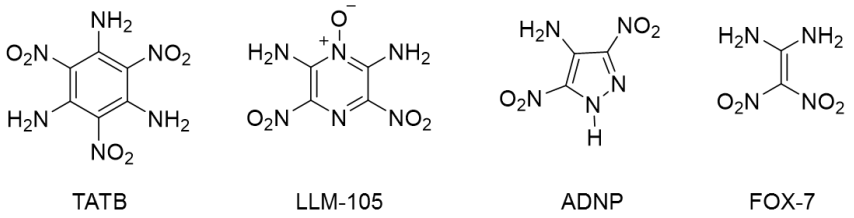

Figure 1.3 Examples of insensitive energetic materials.

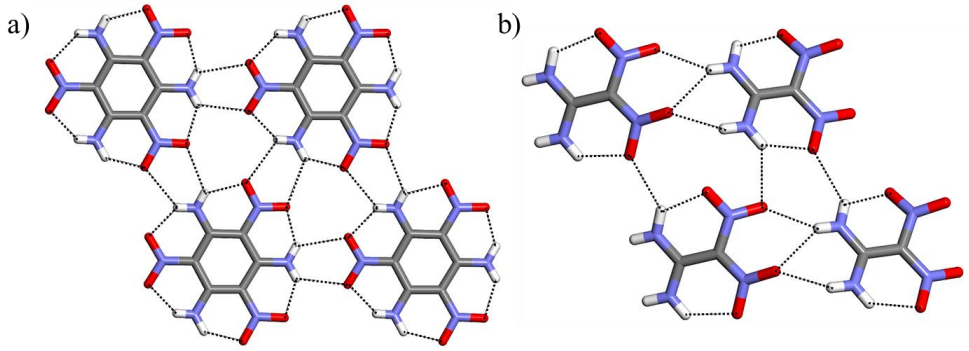

Figure 1.4 Examples of graphite-like sheets formed through strong inter- and intramolecular hydrogen bonding in insensitive energetics: a) 1,3,5-triamino-2,4,6-trinitrobenzene (TATB) and b) 1,1-diamino-2,2-dinitroethene (DADNE/Fox-7).

The thermal properties of an energetic are important from a sensitivity standpoint, but can also affect the processability of the molecule. A significant processing method that has been utilized to allow for easy and efficient loading of an energetic into a munition is the process of melt casting. A melt castable material should possess the following properties: a low melting point (between 70 to 120 °C), large range between the melting point and the start of decomposition, and high loading density.[9] Materials that display minimal shrinkage during the cooling phase are

preferred since the formation of defects and cracks can occur within a casted material that contracts upon cooling, leading to decreases in performance and higher sensitivities to external stimuli (thermal, impact, static and friction). TNT, one of the most recognizable energetic materials, has seen significant applications in both as a military and industrial explosive since it was first synthesized back in 1863. While TNT is considered to be of relatively low performance with a detonation velocity of 6900 m/s, its continued use as an important explosive nearly 150 year later is the result of the low production cost, insensitivity to external stimuli and low melting point (81 °C) allowing for melt casting.[4]

1.3 Methods to Modify Energetic Materials

The traditional methods for improving on the performance and sensitivity properties of an energetic material have focused on the synthesis of novel compounds. The performance and sensitivity of modern energetic materials has surpassed many of the traditional materials through the addition of polynitration, use of highly strained ring systems and/or the introduction of heterocyclic ring systems.[2, 10-12] CL-20 and octanitrocubane (ONC) represent two of the highest performing energetics (>9000 m/s) synthesized over the past 30 years that utilize both high ring strain and polynitration, but have not seen extensive application due to significant synthetic costs, see Figure 1.5.[2, 12] 4,10-dinitro-2,6,8,12-tetraoxa-4,10-diazaisowurtzitane (TEX) is a CL-20 derivative that is cheaper to produce and still possesses a high performance.

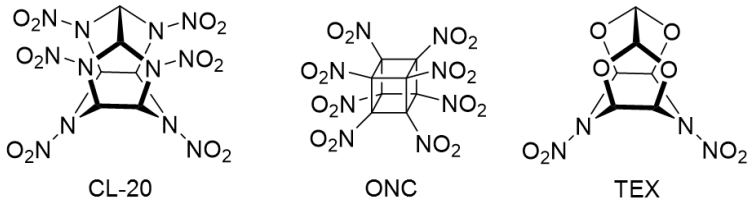

Figure 1.5 Examples of energetics featuring high ring strain.

There has been a general push throughout the field of energetics to develop materials that have high crystalline densities, but are also insensitive to external stimuli. The azole 4-Amino-3,5-dinitropyrazole (ADNP/LLM-116) is an example of a molecule that was designed as an analogue of TATB, the gold standard for insensitive energetics, with the ultimate goal of improving the oxygen balance in the system through incorporation of nitrogen from the heterocycle. ADNP possesses a high density (1.900 g/cm^3) and low sensitivity to impact, but its development has been hindered by poor thermal sensitivity (melts before decomposing around 180 °C).[12, 13] Though considerable resources have been applied towards the synthesis of novel energetics, few materials have seen significant scale up due to the rigorous requirements for performance, safety and economical production. As a result, many of the energetic compounds that are used in our military today are those established during WWII or well before (TNT, PETN, RDX and HMX).

Table 1.1 Density and detonation velocity (V_d) values for the four CL-20 polymorphs (α-, β-, γ- and ε-). Detonation velocity is predicted with Cheetah 7.0 using the crystallographic densities.[14]

Compound	Density (g/cm^3)	V_d (m/s)*
γ-CL20	1.92	9085
α-CL20	1.97	9271
β-CL20	1.99	9333
ε-CL20	2.04	9511

*Predicted by Cheetah 7.0

The vast majority of energetic materials are crystalline in the solid state and exhibit long range order of molecules or atoms which has a profound effect on important materials physical properties, such as density and stability. When more than one arrangement is possible for the assembly of molecules into a crystal lattice, this is termed polymorphism, see Figure 1.6. Due to

differences in the inter-/intramolecular interactions and packing of the molecules, various polymorphs of an energetic material differ in their density and sensitivity. Most energetic materials exhibit multiple polymorphs, for example, the high explosives CL-20 and HMX both have four thermodynamically stable polymorphs, with other metastable forms accessible through high pressure and/or high temperature crystallization methods.[15] The impact of polymorphs on the performance of a material is highlighted in Table 1.1 for the four CL-20 polymorphs. The polymorph that displays the highest density and lowest sensitivity is utilized for applications as an explosive. The differences in the physical properties of polymorphs is often subtle, so for more dramatic alteration of properties research has investigated novel methods such as multicomponent crystallization to achieve desired materials properties.

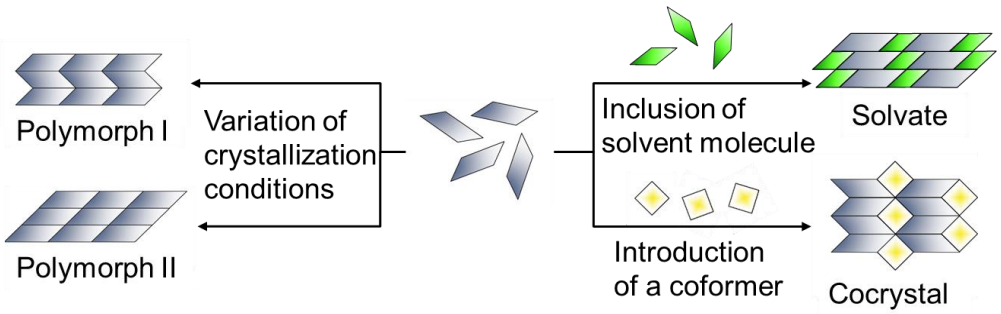

Figure 1.6 Polymorphism: different packing/conformation of the same molecule or compound. Multicomponent crystal formation: a cocrystal is formed between two solid components, whereas a solvate is formed between solid and liquid components.

1.4 Multicomponent Crystallization

The crystal engineering tool of multicomponent crystallization (cocrystallization or solvate formation) has been used to significantly modify physical properties of pharmaceuticals[16-19] and organic electronic materials[20-25], and more recently has been applied to energetic materials[26-28]. A multicomponent crystal forms through noncovalent interactions between two or more neutral molecular components, that ultimately possess different physical properties as compared to a physical mixture of the pure components, see Figure 1.6. Like single component crystals,

multicomponent crystals will typically rely on the formation of a various different types of noncovalent interactions, including electrostatic interactions and π-effects.

Hydrogen bonding is a short and directional electrostatic interaction that occurs between a covalently-bonded hydrogen atom and an electronegative atom. Because they are one of strongest and most robust intermolecular interactions, hydrogen bonds have been often been utilized by crystal engineers.[29] An alternative electrostatic interaction that is gaining more traction as a crystal engineering tool is halogen bonding (XB). Halogen bonding occurs between a nucleophile and the σ-hole of a highly polarized halogen atom. The σ-hole is a region of positive electrostatic potential, whose size and strength increases upon descending the periodic table (Cl < Br < I).[30] Neighboring functionality will directly influence the polarization of the halogen atom in the molecule, and as a result will alter the size of the σ-hole and strength of a halogen bond. Electron-withdrawing groups will increase strength of the interaction by increasing the σ-hole, whereas electron-donating groups have the opposite effect. Halogen bonds are highly directional and have strength similar to that of a typical hydrogen bond, 2-5 kcal/mol.[31]

Another significant noncovalent interaction often seen in materials containing conjugation or aromatic ring systems are various π-effects. These π-effects occur through donation of electron density from electron rich π-systems into electron poor π-systems, and with the observed arrangements including face-to-face, slipped stack and edge-to-face for aromatic rings, see Figure 1.7.[32, 33]

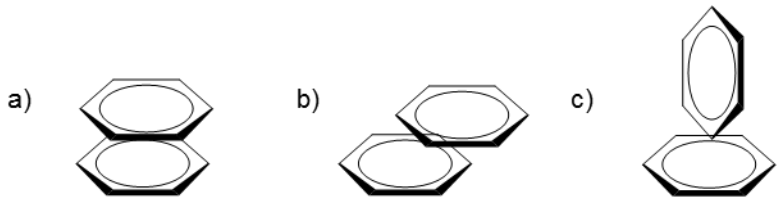

Figure 1.7 Examples of π-effects with an aromatic ring: a) face-to-face, b) slipped stack and c) edge-to-face.

Thorough understanding of the potential interactions available to a particular coformer will allow for novel materials to be designed from robust synthons. Multicomponent crystals have seen significant success in pharmaceutical development, which is a direct result of most drugs molecule possessing diverse functional groups as well as the large library of acceptable coformers. The functional groups that are present in most energetic compounds are more limited and include various nitro groups (nitroesters, nitramines, etc.), amines, aromatic/heterocyclic rings, and, occasionally, carbonyls. The presence of these weak hydrogen bond acceptors and lack of traditional hydrogen bond donors has led to difficulties in crystal engineering of energetic materials.

1.5 Multicomponent Energetics in the Literature

1.5.1 Multicomponent Materials With Non-Energetic Coformers

Early work in multicomponent energetic materials focused on the identification of molecular characteristics that would facilitate the formation of energetic cocrystals of non-energetic cocrystal formers. For the initial study in 2010, researchers in the Matzger group focused on the cocrystallization of prototypical energetic, TNT.[26] TNT served as a good starting point to understanding the formation of multicomponent energetic materials because it is one of the most-studied and well-understood energetic materials. A total of 17 novel TNT cocrystals were discovered, whose formation relied heavily upon donor-acceptor π-π interactions. Secondary interactions included various hydrogen bonding interactions with the nitro groups on the TNT.

Two additional studies in 2012 on energetic cocrystal with non-energetic coformers were performed with HMX[27] in the Matzger group and CL-20[28] in the Pulham group, resulting in 7 and 4 novel materials respectively. These HMX and CL-20 cocrystals relied upon hydrogen bonding with traditional hydrogen bond donating groups and the weaker C-H···nitro interactions. While these materials all suffer from poor performance due to the underoxidation of the non-energetic components, the insight gained on the intermolecular interactions necessary for cocrystallization of energetic materials could be broadly applied to many multi-energetic systems, see Figure 1.8.

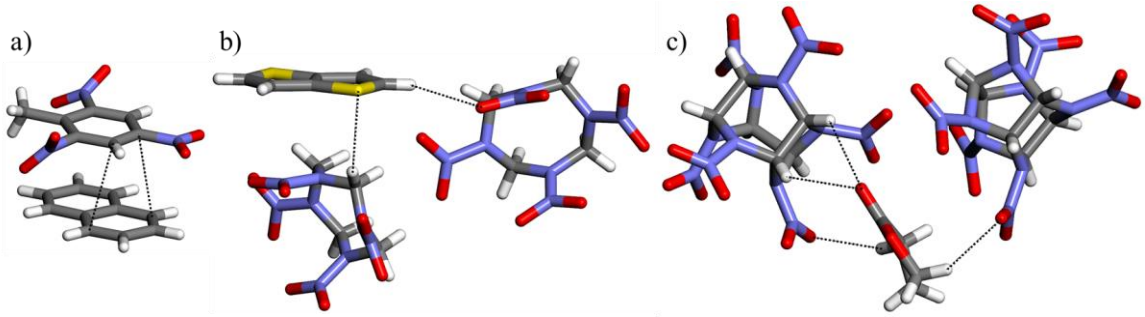

Figure 1.8 Examples of intermolecular interactions present in the energetic cocrystals formed with non-energetic coformers: a) π-π interactions of TNT/naphthalene, b) C-H···nitro and C-H···S hydrogen bonding in HMX/thieno[3,2-*b*]thiophene, and c) hydrogen bonding in CL-20/dihydrofuran-2(3*H*)-one.

1.5.2 Multicomponent Energetic-Energetic Materials

The first example of a cocrystal involving two energetic materials was reported in 2011 by the Matzger group, involving TNT and CL-20 in a 1:1 ratio.[34] The TNT/CL-20 cocrystal showed that the high sensitivity of CL-20 could be drastically reduced through the formation of intermolecular interactions with the insensitive TNT through nitro-π and C-H···nitro as key interactions. An intriguing thermal property associated with the TNT/CL-20 cocrystal, is that the material can be heat "activated" to the sensitivity of CL-20 through the melting the cocrystal (MP = 136 °C). Upon melting the cocrystal phase separates into the two respective components,

liquid TNT and either the β- or γ-Cl-20 polymorphs, allowing for the material be transported as the insensitive cocrystal and "activated" prior to usage. In 2014, the Li group reported a CL-20 cocrystal with 1,3-dinitrobenzene (DNB) that has similar properties to the TNT/CL-20 cocrystal.[35] By applying insight on the intermolecular interactions discovered in the TNT/CL-20 cocrystal, the Matzger group was able to synthesize a 2:1 cocrystal between CL-20 and HMX in 2012.[36] The pure components HMX and CL-20 represent the highest performing energetics currently fielded by the US military, but as previously stated CL-20 possesses high sensitivity. The 2:1 CL-20/HMX cocrystal possesses the sensitivity of β-HMX, with the performance of CL-20 and highlights the synergy that can be achieved through cocrystallization. Scientists at Nalas Engineering recently discovered a cocrystal between CL-20 and 1-methyl-3,5-dinitro-1,2,4-triazole (MDNT), which possessed lower friction sensitivity compared to pure CL-20.[37] Researcher in the Sinditskii lab out of Russia were able to utilize the linear nitramines 2,4-dinitro-2,4-diazapentane (DNP) and 3,5-dinitro-3,5-diazaheptane (DNG) to form two novel CL-20 cocrystals.[38] The various bonding motifs that have been identified with CL-20 demonstrate that a thorough understanding of weak intermolecular interactions like the C-H···nitro are vital in the design of multicomponent energetics, see Figure 1.10.

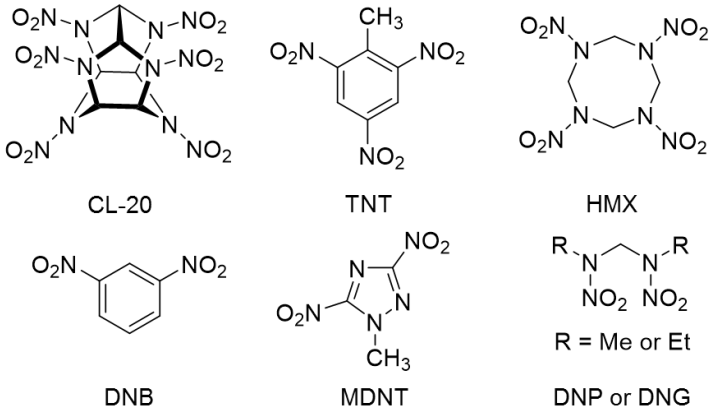

Figure 1.9 Chemical structure of the pure energetic components for the CL-20 cocrystals.

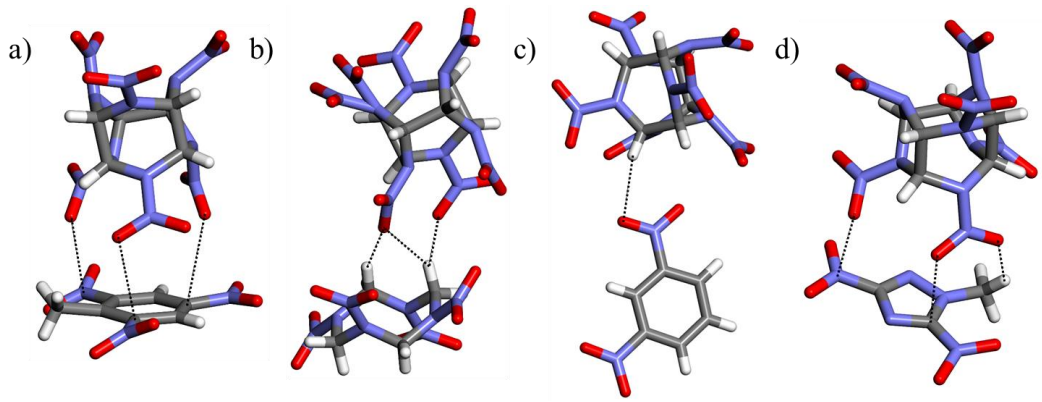

Figure 1.10 Key intermolecular interactions present in the CL-20 cocrystals: a) nitro-π interactions of CL-20/TNT, b) C-H···nitro hydrogen bonding in CL-20/HMX, c) C-H···nitro in CL-20/DNB, and d) nitro-π and C-H···nitro interactions of CL-20/MDNT.

Around the same time of the discovery of the 2:1 CL-20/HMX cocrystals, the Huang group out of China published two papers on a series of six novel energetic cocrystal containing benzotrifuroxan (BTF).[39, 40] All of the cocrystals in this series relied upon nitro-π interactions with the electron poor ring of BTF, similar to those observed in the non-energetic cocrystals of TNT, as well weaker C-H interactions between the respective components. The first cocrystal published in this series formed between BTF and CL-20, which was predicted to have higher performance compared to pure BTF.[39] In the second publication, the Huang group presented five novel cocrystals of BTF with TNT, 1,3,5-trinitrobenzene (TNB), 2,4,6-trinitroaniline (TNA), 2,4,6-trinitrobenzene methylamine (MATNB) and 1,3,3-trinitroazetinine (TNAZ), which possessed varying degrees of sensitivity to impact.[40] The BTF/TNB cocrystals showed not only decreased sensitivity, but also had performance comparable to that of 1,3,5-trinitro-1,3,5-triazacyclohexane (RDX), suggesting that BTF/TNB could be a potential replacement for RDX. In 2014, the Li group reported an additional BTF cocrystal with DNB possessing good performance and insensitivity to impact.[41] This diverse list of cocrystal above demonstrates BTF as a robust and reliable coformer for energetic cocrystals, and the information gained from these

materials will be useful in the discovery of addition cocrystals in the furazan family, see Figure 1.12.

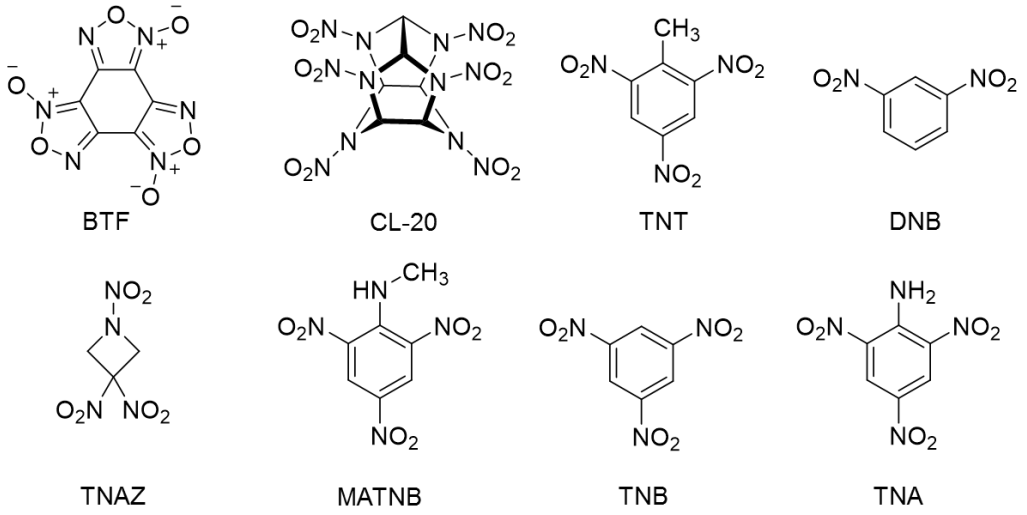

Figure 1.11 Chemical structure of the pure energetic components for the BTF cocrystals.

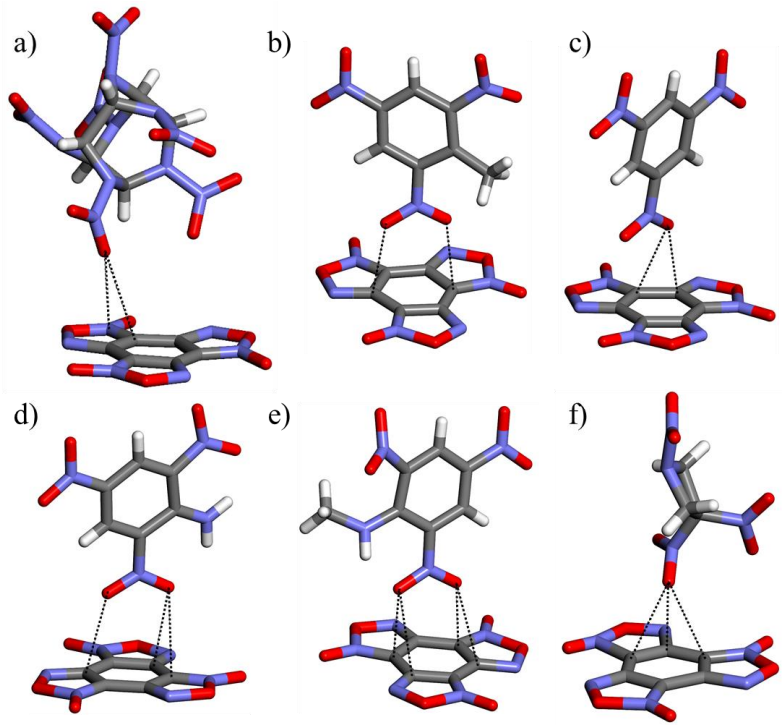

Figure 1.12 Key nitro-π interactions present in the BTF cocrystals: a) CL-20/BTF, b) BTF/TNT, c) BTF/TNB, d) BTF/TNA, e) BTF/MATNB, and f) BTF/TNAZ

In an effort to expand upon the available molecular synthons for cocrystallization of energetics the Matzger group looked into the cocrystallization of some exotic energetic materials, such as diacetone diperoxide (DADP). In 2013 and 2015 the group reported a series of energetic cocrystals of DADP with 1,3,5-trihalo-2,4,6-trinitrobenze's (TXTNB, where X = Cl, Br or I) in 1:1 ratios.[42, 43] The cocrystals of 1,3,5-trichloro-2,4,6-trinitrobenzene (TCTNB) and 1,3,5-tribromo-2,4,6-trinitrobenzene (TBTNB) were both isostructural and were formed through peroxy-π interactions. Both of these materials maintained the high sensitivity to impact of the pure component DADP. The cocrystal with 1,3,5-triiodo-2,4,6-trinitrobenzene (TITNB) was determined to not be isostructural to the other two TXTNBs and showcased a different intermolecular interaction between the iodo-peroxide, first example of preferential halogen bonding in energetic cocrystals. The TITNB cocrystal showed, for the first time, two primary energetics cocrystallizing to make a secondary energetic.[43] The addition of a halogen atom onto a the backbone of an energetic offers a reliable and robust intermolecular interactions in the formation of energetic cocrystals, without degradation to the performance properties, see Figure 1.14. Halogens are useful for biocidal applications and act oxidizers in a detonation, which helps to improve the oxygen balance, see Chapter 3.

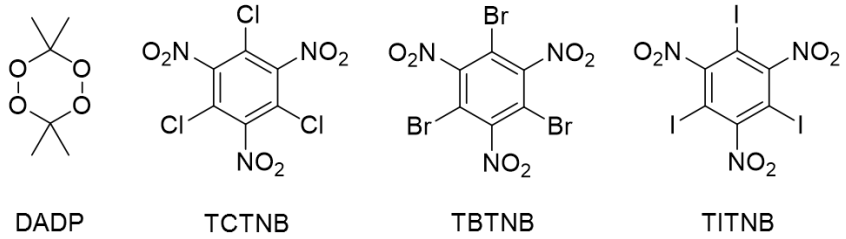

Figure 1.13 Chemical structure of the pure energetic components for the DADP cocrystals.

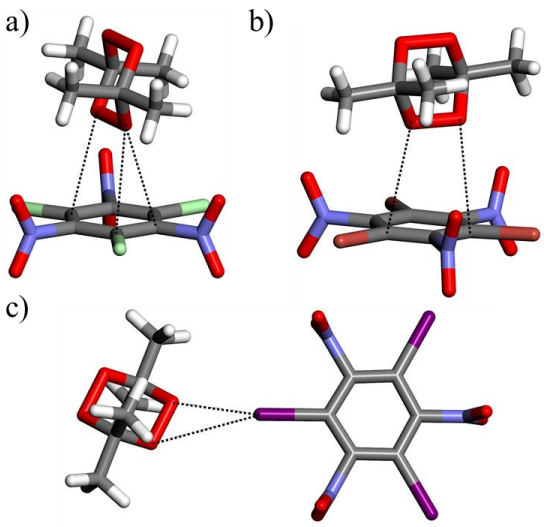

Figure 1.14 Key intermolecular interactions present in the DADP cocrystals: a) peroxy-π interactions of DADP/TCTNB, b) peroxy-π interactions of DADP/TBTNB, and c) iodo-peroxide halogen bonding interactions of DADP/TITNB.

Recently, several non-standard energetic materials have been used to identify novel intermolecular synthons. In 2015, the Shreeve group reported two energetic cocrystals of 1H,4H-3,6-dinitropyrazolo[4,3-c]pyrazole (DNPP) with the non-energetic materials 3-amino-1,2,4-triazole and 4-amino-1,2,4-triazole, that possess performance greater than TNT.[44] The Zhang group synthesized a novel 3-nitro-1,2,4-triazol-5-one (NTO) cocrystal with 5,6,7,8-tetrahydrotetrazolo[1,5-b][1,2,4]-triazine (TZTN) and found that cocrystallization reduced the sensitivity TZTN through the incorporation of the insensitive energetic NTO.[45] The cocrystals of both DNPP and NTO utilized the strong hydrogen bond donors in the azole rings to interact with their respective coformers, see Figure 1.16. A congruent study in our group identified a series of azole energetic-energetic cocrystal with 5,5'-dinitro-2H,2H'-3,3'-bi-1,2,4-triazole (DNBT), see Chapter 2.

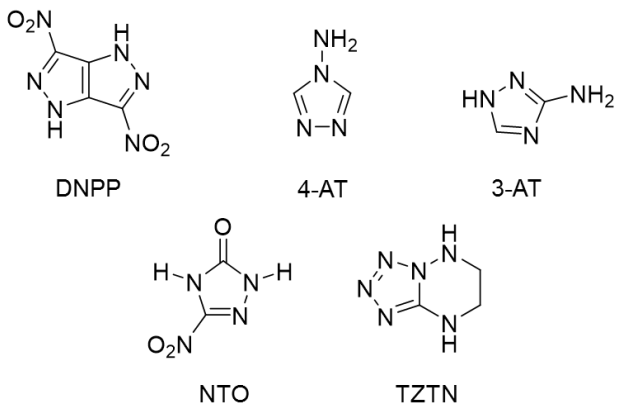

Figure 1.15 Chemical structure of the pure energetic components for the DNPP and NTO cocrystals.

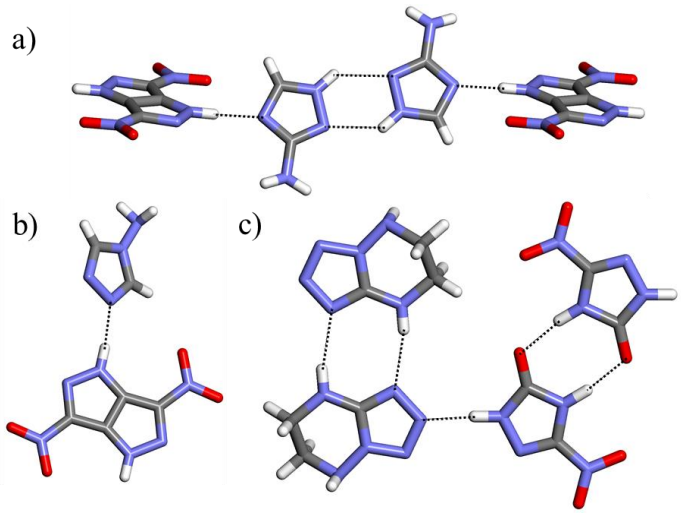

Figure 1.16 Key hydrogen bonding interactions between the amines and heterocyclic rings present in the DNPP and NTO cocrystals: a) DNPP/3-AT, b) DNPP/4-AT, and c) DNPP/4-AT.

In order to develop reliable methods for engineering energetic cocrystals, the important interactions amongst the various families of energetic materials must first be identified. In an effort to elucidate the types of intermolecular interactions that are feasible between various energetic components, the work in this thesis focuses on the multicomponent crystallization of a broad library of energetic materials (nitrobenzenes, azoles, nitroesters, nitramines).

1.6 Outline of the Thesis

1.6.1 Chapter 2: Design and Synthesis of a Series of Nitrogen-Rich Energetic Cocrystals of 5,5'-Dinitro-2H,2H'-3,3'-bi-1,2,4-triazole (DNBT)

A series of three energetic cocrystals containing 5,5'-dinitro-2H,2H'-3,3'-bi-1,2,4-triazole (DNBT) were obtained. These incorporate a class of energetic materials that has seen significant synthetic work, the azole family (tetrazoles, triazole, pyrazole, etc.), and yet have struggled to see broad application. A cocrystal was obtained with the triazole 5-amino-3-nitro-1H-1,2,4-triazole (ANTA) in a stoichiometry of 2:1 (ANTA:DNBT). Two cocrystals were obtained with the pyrazoles 1H,4H-3,6-dinitropyrazolo[4,3-c]pyrazole (DNPP) and 3,4-dinitropyrazole (3,4-DNP) in ratios of 1:1 (DNPP:DNBT) and 2:1 (3,4-DNP:DNBT). All three cocrystals, 2:1 ANTA/DNBT (**1**), 1:1 DNPP/DNBT (**2**), and 2:1 3,4-DNP/DNBT (**3**), have high densities (>1.800 g/cm^3) and high predicted detonation velocities (>8000 m/s). In small-scale impact drop tests cocrystals **1** and **2** were both found to be insensitive, whereas cocrystal **3** possesses sensitivity between that of its two pure components 3,4-DNP and DNBT. The hydrogen bonding motif of the three components with DNBT is preserved among all three cocrystals, and this observation suggests a generally useful motif to be employed in the development of other energetic-energetic cocrystals. These cocrystals represent an area of energetic materials that have yet to be explored for cocrystalline materials.

1.6.2 Chapter 3: Isostructural Cocrystals of 1,3,5-Trinitrobenzene Assembled by Halogen Bonding

Two isostructural energetic cocrystals containing 1,3,5-trinitrobenzene (TNB) were obtained with the energetic materials 1,3,5-triiodo-2,4,6-trinitrobenzene (TITNB) and 1,3,5-tribromo-2,4,6-trinitrobenzene (TBTNB) in ratios of 2:1 TNB/TITNB (**1**) and 2:1 TNB/TBTNB (**2**). These

materials contain the shortest nitro-iodo and second shortest nitro-bromo interactions seen in the Cambridge Structural Database (CSD) for organohalides. Computational studies indicate that the cocrystals are more stable than their respective component crystals by 11.5 kJ/mol for **1** and 8.2 kJ/mol for **2**. While the formation of an isostructural 2:1 cocrystal with 1,3,5-trichloro-2,4,6-trinitrobenzene (TCTNB) was calculated to be favorable by 8.5 kJ/mol, only a physical mixture of the two coformers was obtained experimentally. Both **1** and **2** possess high crystallographic densities (2.203 and 1.980 g/cm^3 respectively) and were found to be insensitive in small-scale impact drop tests, possessing sensitivity between that of TNB and TXTNB (X = I or Br). The halogen content of the two cocrystals suggests application as insensitive biocidal energetics. Halogen bonding, facilitated by the strong polarization induced by aromatic ring nitration, plays a critical role in the formation of these cocrystals and offers one of the most promising routes to the development of new energetic cocrystals.

1.6.3 Chapter 4: Hydrogen Peroxide Solvates of 2,4,6,8,10,12-Hezanitro-2,4,6,8,10,12-Hexaazaisowurtzitane

Two polymorphic hydrogen peroxide (HP) solvates of 2,4,6,8,10,12-hexanitro-2,4,6,8,10,12-hexaazaisowurtzitane (CL-20) were obtained using the hydrated α-CL-20 as a guide. These novel HP solvates have high crystallographic densities (1.96 and 2.03 g/cm^3 respectively), high predicted detonation velocities/pressures (with one solvate possessing greater performance than that of ε-CL-20) and sensitivity similar to that of ε-CL-20. The use of hydrated materials as a guide will be important in the development of other energetic materials with hydrogen peroxide. These solvates represent an area of energetic materials that have yet to be explored.

1.7 References

1. Akhavan, J., *The Chemistry of Explosives*. Second Edition ed.; The Royal Society of Chemistry: Cambridge, UK, 2004; p 1-196.

2. Klapötke, T. M., *Chemistry of High-Energy Materials*. 2 ed.; Walter de Gruyter: Berlin/Boston, 2012.

3. Kamlet, M. J.; Jacobs, S. J., Chemistry of Detonations. I. A Simple Method for Calculating Detonation Properties of C–H–N–O Explosives. *J. Chem. Phys.* **1968,** *48*, 23-35.

4. Meyer, R.; Köhler, J.; Homburg, A., In *Explosives*, Wiley-VCH Verlag GmbH & Co. KGaA2003; pp 307-360.

5. Lothrop, W. C.; Handrick, G. R., The Relationship between Performance and Constitution of Pure Organic Explosive Compounds. *Chem. Rev.* **1949,** *44*, 419-445.

6. Mustafa, A.; Zahran, A. A., Tetryl, Pentyl, Hexyl, and Nonyl. Preparation and Explosive Properties. *J. Chem. Eng. Data* **1963,** *8*, 135-150.

7. Ma, Y.; Zhang, A.; Zhang, C.; Jiang, D.; Zhu, Y.; Zhang, C., Crystal Packing of Low-Sensitivity and High-Energy Explosives. *Cryst. Growth Des.* **2014,** *14*, 4703-4713.

8. Zhang, C.; Wang, X.; Huang, H., π-Stacked Interactions in Explosive Crystals: Buffers against External Mechanical Stimuli. *J. Am. Chem. Soc.* **2008,** *130*, 8359-8365.

9. Ravi, P.; Badgujar, D. M.; Gore, G. M.; Tewari, S. P.; Sikder, A. K., Review on Melt Cast Explosives. *Propell. Explos. Pyrotech.* **2011,** *36*, 393-403.

10. Agrawal, J. P.; Hodgson, R. D., Synthetic Routes to Aromatic C-Nitro Compounds. In *Organic Chemistry of Explosives*, John Wiley & Sons, Ltd2007; pp 125-189.

11. Gao, H.; Shreeve, J. n. M., Azole-Based Energetic Salts. *Chem. Rev.* **2011,** *111*, 7377-7436.

12. Pagoria, P. F.; Lee, G. S.; Mitchell, A. R.; Schmidt, R. D., A review of energetic materials synthesis. *Thermochim. Acta* **2002,** *384*, 187-204.

13. Schmidt, R. D.; Lee, G. S.; Pagoria, P. F.; Mitchell, A. R.; Gilardi, R., Synthesis of 4-amino-3,5-dinitro-1H-pyrazole using vicarious nucleophilic substitution of hydrogen. *J. Heterocycl. Chem.* **2001,** *38*, 1227-1230.

14. *Cheetah 7.0 calculations were preformed utilizing the Sandia JCZS product library revision 32.*

15. Bernstein, J., *Polymorphism in Molecular Crystals*. 1 ed.; Oxford University Press Inc.: New York, 2008.

16. Fleischman, S. G.; Kuduva, S. S.; McMahon, J. A.; Moulton, B.; Bailey Walsh, R. D.; Rodríguez-Hornedo, N.; Zaworotko, M. J., Crystal Engineering of the Composition of Pharmaceutical Phases: Multiple-Component Crystalline Solids Involving Carbamazepine. *Cryst. Growth Des.* **2003,** *3*, 909-919.

17. Porter III, W. W.; Elie, S. C.; Matzger, A. J., Polymorphism in Carbamazepine Cocrystals. *Cryst. Growth Des.* **2008,** *8*, 14-16.

18. Sanphui, P.; Goud, N. R.; Khandavilli, U. B. R.; Nangia, A., Fast Dissolving Curcumin Cocrystals. *Cryst. Growth Des.* **2011,** *11*, 4135-4145.

19. Schultheiss, N.; Newman, A., Pharmaceutical Cocrystals and Their Physicochemical Properties. *Cryst. Growth Des.* **2009,** *9*, 2950-2967.

20. Kapadia, P. P.; Ditzler, L. R.; Baltrusaitis, J.; Swenson, D. C.; Tivanski, A. V.; Pigge, F. C., Semiconducting Organic Assemblies Prepared from Tetraphenylethylene Tetracarboxylic Acid and Bis(pyridine)s via Charge-Assisted Hydrogen Bonding. *J. Am. Chem. Soc.* **2011,** *133*, 8490-8493.

21. Koshima, H.; Miyamoto, H.; Yagi, I.; Uosaki, K., Preparation of Cocrystals of 2-Amino-3-nitropyridine with Benzenesulfonic Acids for Second-Order Nonlinear Optical Materials. *Cryst. Growth Des.* **2004,** *4*, 807-811.

22. Sato, S.; Nikawa, H.; Seki, S.; Wang, L.; Luo, G.; Lu, J.; Haranaka, M.; Tsuchiya, T.; Nagase, S.; Akasaka, T., A Co-Crystal Composed of the Paramagnetic Endohedral Metallofullerene La@C82 and a Nickel Porphyrin with High Electron Mobility. *Angew. Chem. Int. Ed.* **2012,** *51*, 1589-1591.

23. Sokolov, A. N.; Friščić, T.; MacGillivray, L. R., Enforced Face-to-Face Stacking of Organic Semiconductor Building Blocks within Hydrogen-Bonded Molecular Cocrystals. *J. Am. Chem. Soc.* **2006,** *128*, 2806-2807.

24. Sun, A.; Lauher, J. W.; Goroff, N. S., Preparation of Poly(diiododiacetylene), an Ordered Conjugated Polymer of Carbon and Iodine. *Science* **2006,** *312*, 1030-1034.

25. Yan, D.; Delori, A.; Lloyd, G. O.; Friščić, T.; Day, G. M.; Jones, W.; Lu, J.; Wei, M.; Evans, D. G.; Duan, X., A Cocrystal Strategy to Tune the Luminescent Properties of Stilbene-Type Organic Solid-State Materials. *Angew. Chem. Int. Ed.* **2011,** *50*, 12483-12486.

26. Landenberger, K. B.; Matzger, A. J., Cocrystal Engineering of a Prototype Energetic Material: Supramolecular Chemistry of 2,4,6-Trinitrotoluene. *Cryst. Growth Des.* **2010,** *10*, 5341-5347.

27. Landenberger, K. B.; Matzger, A. J., Cocrystals of 1,3,5,7-Tetranitro-1,3,5,7-tetrazacyclooctane (HMX). *Cryst. Growth Des.* **2012,** *12*, 3603-3609.

28. Millar, D. I. A.; Maynard-Casely, H. E.; Allan, D. R.; Cumming, A. S.; Lennie, A. R.; Mackay, A. J.; Oswald, I. D. H.; Tang, C. C.; Pulham, C. R., Crystal engineering of energetic materials: Co-crystals of CL-20. *CrystEngComm* **2012,** *14*, 3742-3749.

29. Steiner, T., The Hydrogen Bond in the Solid State. *Angew. Chem. Int. Ed.* **2002,** *41*, 48-76.

30. Politzer, P.; Murray, J. S.; Clark, T., Halogen bonding and other [sigma]-hole interactions: a perspective. *Phys. Chem. Chem. Phys.* **2013,** *15*, 11178-11189.

31. Cavallo, G.; Metrangolo, P.; Milani, R.; Pilati, T.; Priimagi, A.; Resnati, G.; Terraneo, G., The Halogen Bond. *Chem. Rev.* **2016,** *116*, 2478-2601.

32. Headen, T. F.; Howard, C. A.; Skipper, N. T.; Wilkinson, M. A.; Bowron, D. T.; Soper, A. K., Structure of π−π Interactions in Aromatic Liquids. *J. Am. Chem. Soc.* **2010,** *132*, 5735-5742.

33. Hunter, C. A.; Sanders, J. K. M., The nature of .pi.-.pi. interactions. *J. Am. Chem. Soc.* **1990,** *112*, 5525-5534.

34. Bolton, O.; Matzger, A. J., Improved Stability and Smart-Material Functionality Realized in an Energetic Cocrystal. *Angew. Chem. Int. Ed.* **2011,** *50*, 8960-8963.

35. Wang, Y.; Yang, Z.; Li, H.; Zhou, X.; Zhang, Q.; Wang, J.; Liu, Y., A Novel Cocrystal Explosive of HNIW with Good Comprehensive Properties. *Propell. Explos. Pyrotech.* **2014,** *39*, 590-596.

36. Bolton, O.; Simke, L. R.; Pagoria, P. F.; Matzger, A. J., High Power Explosive with Good Sensitivity: A 2:1 Cocrystal of CL-20:HMX. *Cryst. Growth Des.* **2012,** *12*, 4311-4314.

37. Anderson, S. R.; Dubé, P.; Krawiec, M.; Salan, J. S.; Ende, D. J. a.; Samuels, P., Promising CL-20-Based Energetic Material by Cocrystallization. *Propell. Explos. Pyrotech.* **2016,** *41*, 783-788.

38. Goncharov, T. K.; Aliev, Z. G.; Aldoshin, S. M.; Dashko, D. V.; Vasil´eva, A. A.; Shishov, N. I.; Milekhin, Y. M., Preparation, structure, and main properties of bimolecular crystals CL-20—DNP and CL-20—DNG. *Russ Chem Bull* **2015,** *64*, 366-374.

39. Yang, Z.; Li, H.; Zhou, X.; Zhang, C.; Huang, H.; Li, J.; Nie, F., Characterization and Properties of a Novel Energetic–Energetic Cocrystal Explosive Composed of HNIW and BTF. *Cryst. Growth Des.* **2012,** *12*, 5155-5158.

40. Zhang, H.; Guo, C.; Wang, X.; Xu, J.; He, X.; Liu, Y.; Liu, X.; Huang, H.; Sun, J., Five Energetic Cocrystals of BTF by Intermolecular Hydrogen Bond and π-Stacking Interactions. *Cryst. Growth Des.* **2012,** *13*, 679-687.

41. Yang, Z.; Wang, Y.; Zhou, J.; Li, H.; Huang, H.; Nie, F., Preparation and Performance of a BTF/DNB Cocrystal Explosive. *Propell. Explos. Pyrotech.* **2014,** *39*, 9-13.

42. Landenberger, K. B.; Bolton, O.; Matzger, A. J., Two Isostructural Explosive Cocrystals with Significantly Different Thermodynamic Stabilities. *Angew. Chem. Int. Ed.* **2013,** *52*, 6468-6471.

43. Landenberger, K. B.; Bolton, O.; Matzger, A. J., Energetic-Energetic Cocrystals of Diacetone Diperoxide (DADP): Dramatic and Divergent Sensitivity Modifications via Cocrystallization. *J. Am. Chem. Soc.* **2015,** *137*, 5074-5079.

44. Zhang, J.; Parrish, D. A.; Shreeve, J. n. M., Curious cases of 3,6-dinitropyrazolo[4,3-c]pyrazole-based energetic cocrystals with high nitrogen content: an alternative to salt formation. *Chem. Commun.* **2015,** *51*, 7337-7340.

45. Wu, J.-T.; Zhang, J.-G.; Li, T.; Li, Z.-M.; Zhang, T.-L., A novel cocrystal explosive NTO/TZTN with good comprehensive properties. *RSC Adv.* **2015,** *5*, 28354-28359.

Chapter 2: Design and Synthesis of a Series of Nitrogen-Rich Energetic Cocrystals of 5,5'-Dinitro-2H,2H'-3,3'-bi-1,2,4-triazole (DNBT)

Published: Bennion, J.C.; McBain, A.; Son, S.F.; Matzger, A. J., *Cryst. Growth Des.*, **2015**, *15*, (5), 2545-2549.

2.1 Introduction

Cocrystallization allows for the alteration of the physical properties of materials and has been applied broadly in the fields of pharmaceuticals,[1-4] non-linear optical materials,[5-7] organic semiconductors[8-10] and in recent years to tune the properties of energetic materials (explosives, propellants and pyrotechnics)[11-13]. A cocrystal is typically comprised of two or more neutral molecular components in a defined ratio, whose formation relies upon noncovalent interactions. The physical properties of an energetic material, such as density and melting/decomposition temperature, directly impact the performance criteria including detonation velocity, physical sensitivity and thermal stability. Cocrystallization affords a new material with novel physical properties that are distinct from both the pure components and from a physical mixture of the pure components. Thus cocrystallization is a method to exploit energetics with existing manufacturing infrastructure and produce new properties controlled by arrangement at the molecular level. This approach could also be applied to "failed" previously synthesized molecules that were deemed to be flawed because of undesirable characteristics, but may be acceptable in cocrystal form.

Early work in energetic cocrystals focused on the identification of molecular characteristics that would facilitate the formation of energetic cocrystals of non-energetic cocrystal formers with 2,4,6-trinitrotoluene (TNT),[11] octahydro-1,3,5,7-tetranitro-1,3,5,7-tetrazocine (HMX)[12] and

2,4,6,8,10,12-hexanitro-2,4,6,8,10,12-hexaazaisowurtzitane (CL-20),[13] and then shifted to the formation of energetic cocrystals derived solely from energetic components.[14-20] Many of the traditional hydrogen bonding functional groups (carbonyl, hydroxyl, amines, carboxylic acid, etc.) that are used in the crystal engineering of cocrystalline materials are not present in most energetics; the majority of energetic materials contain various nitro groups including nitroesters, nitramines, and nitroaromatics. The presence of these weak hydrogen bond acceptors and lack of traditional hydrogen bond donors (many energetics only contain aliphatic or aromatic C-H) has led to difficulties in crystal engineering and resulted in the discovery of only a few energetic-energetic cocrystals.[14-21] In order to develop reliable methods for engineering energetic cocrystals, the important interactions amongst the various families of energetic materials must first be identified.

One class of energetic materials that has seen significant synthetic development recently are the azoles (pyrazoles, triazoles, and tetrazoles), which are distinguished from the traditional energetics (nitroesters, nitramines, and etc.) due to the high nitrogen content contained within the aromatic rings. The azoles are of particular interest from a crystal engineering standpoint due to the fact that they possess good hydrogen bond donors (primary and secondary amines). 5,5'-Dinitro-2H,2H'-3,3'-bi-1,2,4-triazole (DNBT) is a high density (1.890 g/cm^3), high nitrogen energetic developed in the 1970s.[22] This high explosive is one of a series of azole explosives that possess high detonation velocities, but have struggled to see broad commercial and military application. DNBT has an impact sensitivity lower than that of HMX, the current state-of-the-art military explosive, making the material suitable for many applications that require insensitive munitions (see below). The principle drawback of DNBT is the high propensity to form a low density hydrate (1.74 g/cm^3)[23], which ultimately reduces the overall power of the material due to

the dependency of detonation velocity on the effective density of energetic in the crystal (higher density leads to higher detonation velocity).[24]

An energetic that is structurally similar to DNBT is 5-amino-3-nitro-1H-1,2,4-triazole (ANTA),[25] another prominent member of the triazole family that was originally developed in an effort to replace the traditional explosives in use (1,3,5-trinitro-1,3,5-triazacyclohexane [RDX], HMX, etc.). ANTA possesses sensitivity on par with 1,3,5-triamino-2,4,6-trinitrobenzene (TATB), the current state of the art insensitive high explosive (IHE) in use in munitions, but with slightly diminished power.[26] Another factor that affects ANTA is the presence of a second solid form which bears a polymorphic relationship.[27] The density of ANTA is significantly lower than that of TATB (1.93 g/cm^3) for both polymorphs: α-(1.82 g/cm^3) and β-ANTA (1.73 g/cm^3), and this explains why ANTA has not seen significant usage as an IHE.

Energetic azoles are not limited to only triazoles, but also include compounds with heterocyclic rings which contain two nitrogen atoms including both pyrazoles and imidazoles; two prominent examples in the pyrazole family are 1H,4H-3,6-dinitropyrazolo[4,3-c]pyrazole (DNPP) and 3,4-dinitropyrazole (3,4-DNP). DNPP was first synthesized by Shevelev and coworkers in 1993,[28] like DNBT and ANTA, it is an insensitive explosive that possesses a high density (1.865 g/cm^3). The energetic 3,4-DNP,[29] on the other hand, has a density (1.791 g/cm^3) lower than the densest forms of the other three azole energetics. Another key drawback of 3,4-DNP is that the material is very sensitive, with sensitivity to impact similar to the epsilon form of CL-20 (see below) which precludes broad deployment in currently used munitions.

2.2 Results and Discussion

Presented here are three novel cocrystals of DNBT with ANTA, DNPP and 3,4-DNP. These cocrystals represent a structure class of energetic materials that have yet to been explored for

cocrystalline materials. The cocrystal of DNBT with ANTA adopts a 2:1 molar ratio (see Figure 2.1a for pure component structures). The cocrystal of DNBT and DNPP occurs with a 1:1 molar ratio, whereas the cocrystal of DNBT and 3,4-DNP forms in a 2:1 molar ratio (see Figure 2.1b and 2.1c). The hydrogen bonding motif of the three components with DNBT is preserved among all three cocrystals, and this observation is significant for the further development of other energetic-energetic cocrystals with similar backbone structure and adds to the library of functional groups that will be instrumental in creating strong intermolecular interactions between two or more energetic compounds for the realization of novel energetic cocrystals.

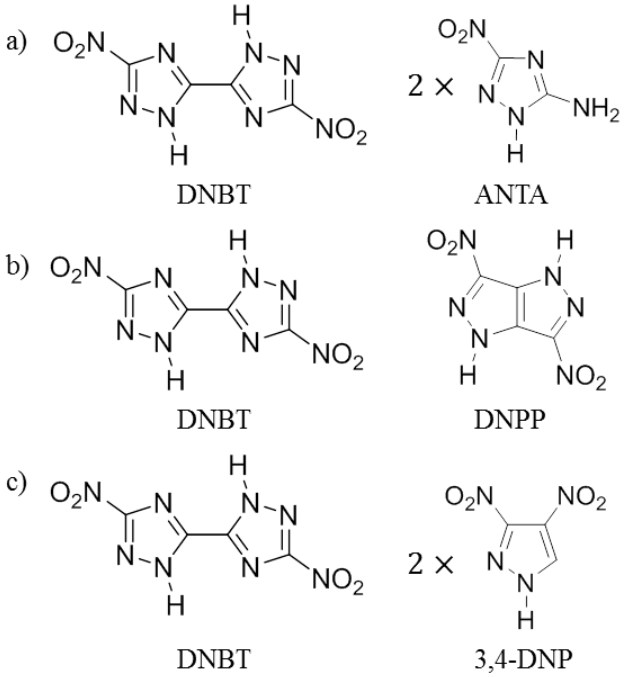

Figure 2.1 Chemical structures of the pure components for each the of three DNBT cocrystals (**1**-**3**): (a) 2:1 ANTA/DNBT cocrystal (**1**), chemical structures of DNBT and ANTA; (b) 1:1 DNPP/DNBT cocrystal (**2**), chemical structures of DNBT and DNPP; (c) 2:1 3,4-DNP/DNBT cocrystal (**3**), chemical structures of DNBT and 3,4-DNP.

Figure 2.2 Typical plate habit morphology of the three DNBT cocrystals (**1-3**): (a) 2:1 ANTA/DNBT cocrystal (**1**); (b) 1:1 DNPP/DNBT cocrystal (**2**); (c) 2:1 3,4-DNP/DNBT cocrystal (**3**).

Cocrystals **1-3** (2:1 ANTA/DNBT, 1:1 DNPP/DNBT and 2:1 3,4-DNP/ DNBT respectively) were all formed initially from acetonitrile solutions and alternatively from isopropanol or acetone; all typically exhibit a plate habit (see Figure 2.2). Raman spectroscopy and powder X-ray diffraction (PXRD) can definitively differentiate cocrystals **1-3** from the pure and hydrated forms of DNBT and the other energetic cocrystal formers (see Appendix A). The crystal structures of the DNBT cocrystals **1-3** were elucidated and the crystallographic data are presented in Table 2.1. All three cocrystals have high crystallographic densities: cocrystal **1** has a density of 1.858 g/cm^3 at 85 K or 1.802 g/cm^3 at room temperature (298 K), cocrystal **2** has a density of 1.889 g/cm^3 at 85 K or 1.833 g/cm^3 at room temperature (298 K), and cocrystal **3** has a density of 1.871 g/cm^3 at 85 K or 1.824 g/cm^3 at room temperature (298 K). Both cocrystals **1** and **2** have densities that are lower than the densities of either of their respective pure components, whereas cocrystal **3** possesses a superior density (1.824 g/cm^3 at 298 K) than that of its pure component 3,4-DNP.

Table 2.1 Crystallographic Data for DNBT Cocrystals (Collected at 85 K)

DNBT Cocrystal	**1**	**2**	**3**
Stoichiometry	2:1	1:1	2:1
Morphology	Plate	Plate	Plate
Space Group	P-1	$P2_1/n$	$P2_1/n$
a (Å)	7.5387(2)	9.6986(2)	9.8182(2)
b (Å)	7.8716(2)	7.22470(10)	6.80370(10)
c (Å)	7.9743(6)	11.4627(8)	14.4194(10)
α (°)	75.469(5)	90	90
β (°)	76.759(5)	111.793(8)	91.927(7)
γ (°)	73.514(5)	90	90
Volume ($Å^3$)	432.842	745.78(6)	962.67(7)
Z	1	2	2
ρ_{calc} (g/cm^3)	1.858	1.889	1.871
Data/Parameter	1556/170	1367/145	1762/181
R_1/wR_2	3.97/11.23	4.34/9.07	2.68/7.05
GOF	1.116	1.198	1.069

The DNBT cocrystals rely on the formation of the same three hydrogen bonding interactions between the hydrogen atoms attached to the heterocyclic rings and the nitrogen atoms within the heterocyclic rings/the nitro groups on the coformers (Figure 2.3). The three cocrystals have an average hydrogen bond length of 2.05, 2.24 and 2.05 Å at 85 K for **1**, **2**, and **3** respectively.[30] In cocrystal **1**, the energetic components form tapes of the repeat unit which propagate throughout the crystal structure. The DNBT sits on an inversion center and acts as a hydrogen donor and acceptor, via a chelating nitrogen-nitro pair, to ANTA molecules (Figure 2.3). The ANTA molecules further dimerize (2.11 Å hydrogen bonding distance) to complete the tape motif through an inversion center. These tapes form into sheets through hydrogen bonding between the aromatic amine of ANTA and the nitro of DNBT (2.35 Å) and these essentially planar sheets are packed through π-stacking interactions between the aromatic rings/nitro groups of the coformers (Figure 2.4a). For cocrystal **2**, the DNPP takes the place of the ANTA dimer in cocrystal **1**, and

both the DNBT and DNPP molecules sit on inversion centers; both components act as a hydrogen donor and acceptor, through chelating nitrogen-nitro pairs from the DNPP instead of the DNBT, as in cocrystal **1** (Figure 2.3). The tapes of cocrystal **2** pack in a herringbone structure dominated by the nitro groups interacting with the π systems (Figure 2.4b). In cocrystal **3,** DNBT interacts with two molecules of 3,4-DNP to form a trimeric unit through hydrogen bonding and acts as a hydrogen donor and acceptor, through chelating nitrogen-nitro pairs from the DNBT, as in cocrystal **1** (Figure 2.3). In contrast to cocrystals **1** and **2** this unit does not extend into tapes, a likely consequence of the additional nitration on the pyrazine ring of 3,4-DNP. The heterotrimer unit interacts with four other heterotrimer units and the closest contacts are through the biaryl linkage (2.81 and 3.01 Å) with the most twisted nitro group on 3,4-DNP (39.84° with respect to the planar 3,4-DNP ring) donating to the π system (Figure 2.4c).

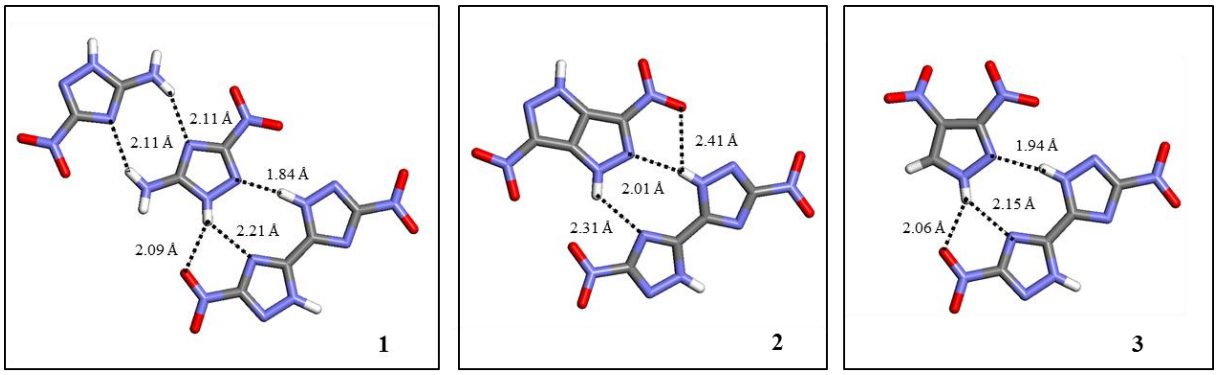

Figure 2.3 Hydrogen bonding motifs utilized in the formation of all three cocrystals **1-3**, all contain three H-bonding interactions between the two respective energetic components in the heterocyclic rings.

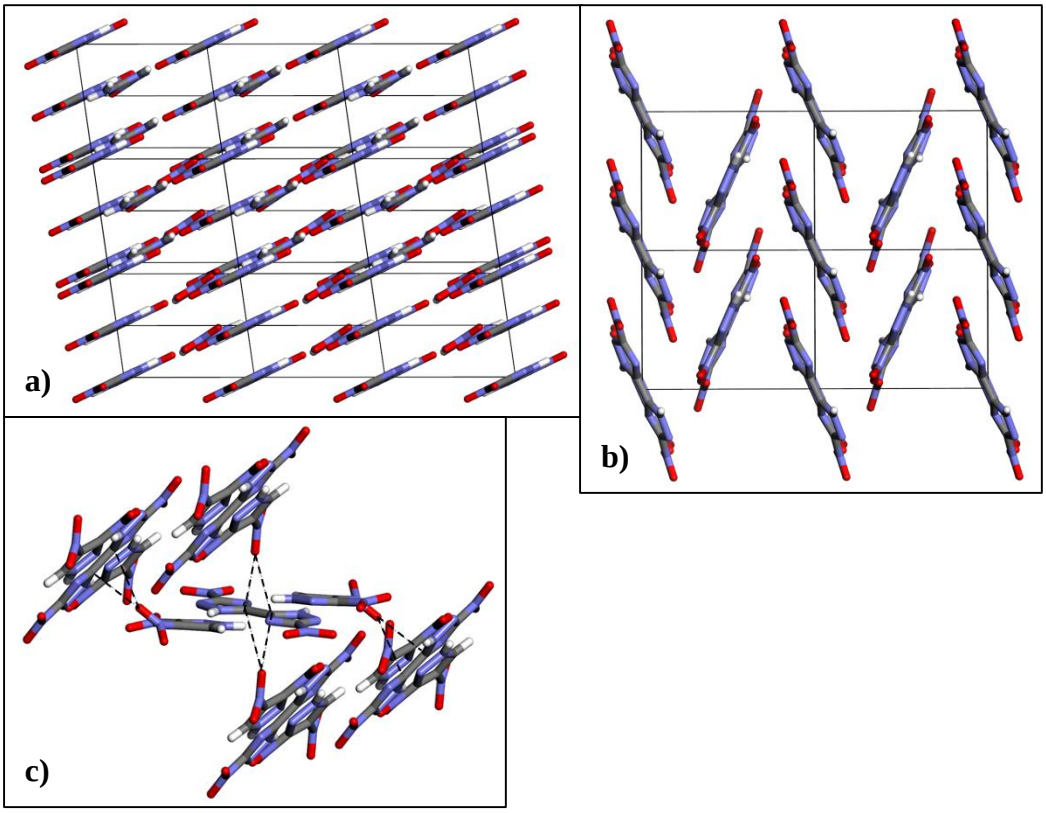

Figure 2.4 Extended packing of each DNBT cocrystals **1-3**: (a) sheet packing of **1**, 2:1 ANTA/DNBT; (b) herringbone packing of **2** (looking down the c-axis), 1:1 DNPP/DNBT; (c) packing interactions between the most twisted nitro groups of 3,4-DNP in the heterotrimer and the biaryl linkage of DNBT in **3**, 2:1 3,4-DNP/DNBT.

The packing coefficient (C_k), which is the measure of the volume occupied by the molecules compared to the volume of the unit cell, was determined for each of the cocrystals and for the pure components (Figure 2.5).[31] For cocrystals **1** (80.6%) and **2** (79.4%) the packing coefficients are lower than those of both of the pure components DNBT (81.5%) and α-ANTA (83.8%) or DNPP (81.1%) respectively. This reduction in the packing efficiency of the cocrystals **1** and **2** compared to their respective pure molecular components can be attributed to the directional hydrogen bonding in the cocrystal tapes adding a defined distance between the two components of the cocrystals that partially compromises close packing. The incorporation of the second molecular unit not only alters the strength of the hydrogen bond seen in the pure components and

thus the hydrogen bond distances, but also causes the packing in the cocrystals to shift to planar packing and herringbone packing for cocrystals **1** and **2** respectively; as a result the molecules no longer occupy space as efficiently. Cocrystal **3** (80.2%) on the other hand achieves a C_k higher than that of the pure component 3,4-DNP (79.8%), which is attributed to the close π interactions between the heterotrimers of the cocrystal compared to sheet packing seen in the pure component.[32, 33] The packing of the heterotrimer and the increase in the packing coefficient for **3** can both be used to explain the higher density found in the cocrystal compared to that of the pure component 3,4-DNP.

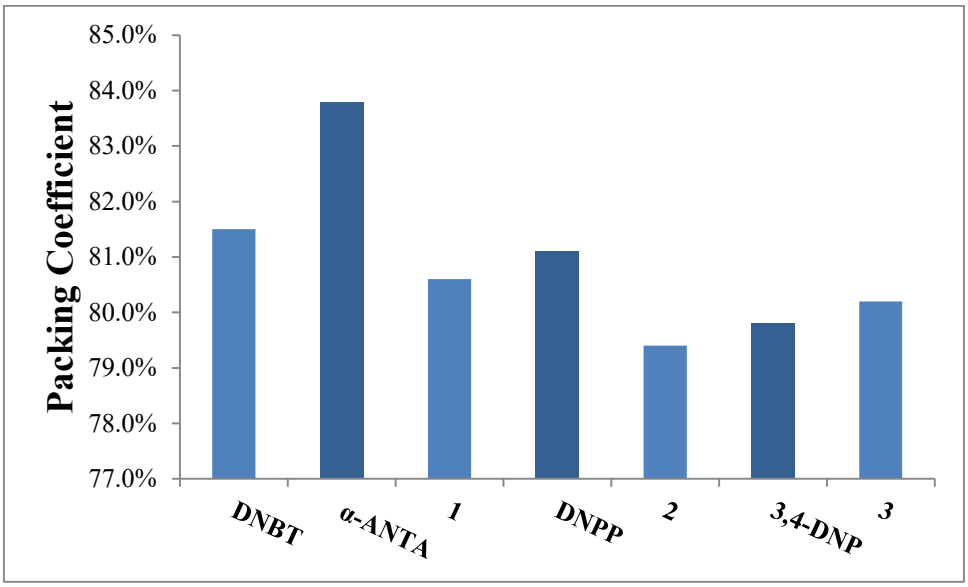

Figure 2.5 Packing coefficients (C_k) of each pure component and DNBT cocrystal **1-3**, are calculated from the room temperature (298 K) crystal lattices of each material.

In order to characterize the novel cocrystalline energetic materials **1-3** for potential use as explosives, the sensitivity was measured by small-scale impact drop testing. Impact drop testing is one of several tests that can be used to determine the sensitivity of a material, but additional tests can be performed to determine the sensitivity to other stimuli such as friction and shock. The apparatus utilized was designed for use with small amounts of material, which are contained within nonhermetic differential scanning calorimetry (DSC) pans. Samples of approximately 2

mg (± 10%) are struck with a freefalling 5 lb drop weight from heights of variable distances until a reproducible Dh_{50} is obtained. For reference, ε-CL-20 and β-HMX exhibit a fifty percent probability of detonation in this apparatus when impacted from heights of 29 and 55 cm, respectively.[14] The sensitivity of all pure components and cocrystals **1**-**3** was determined. Both DNBT and ANTA (Dh_{50} >145 cm) are found to be insensitive in the apparatus, whereas DNPP was seen to react at the maximum of the apparatus at 145 cm. As expected both cocrystal **1** (>145 cm) and **2** (139 cm) can be classified as insensitive explosives, with a slight increase in the sensitivity seen with **2**, potentially attributable to the reduction of hydrogen bonding network in the cocrystal. The insensitivity of the energetic TATB is associated with the crystals vast network of strong inter- and intramolecular hydrogen bonding sheets; the insensitivity of cocrystals **1** and **2** can similarly be associated to the presence of the extended hydrogen bonding tape/sheet networks in the cocrystals.[32, 33] Cocrystal **3** on the other hand has a sensitivity (81 cm) that falls in between that of both pure components: 3,4-DNP (29 cm) and DNBT (>145 cm). Because safety for transportation/handling/storage is a key hurdle that any new energetic material must face before their implementation, the insensitivity of the three novel cocrystals shown here suggest that they may be attractive for use in formulations in future energetic applications where insensitivity is required.

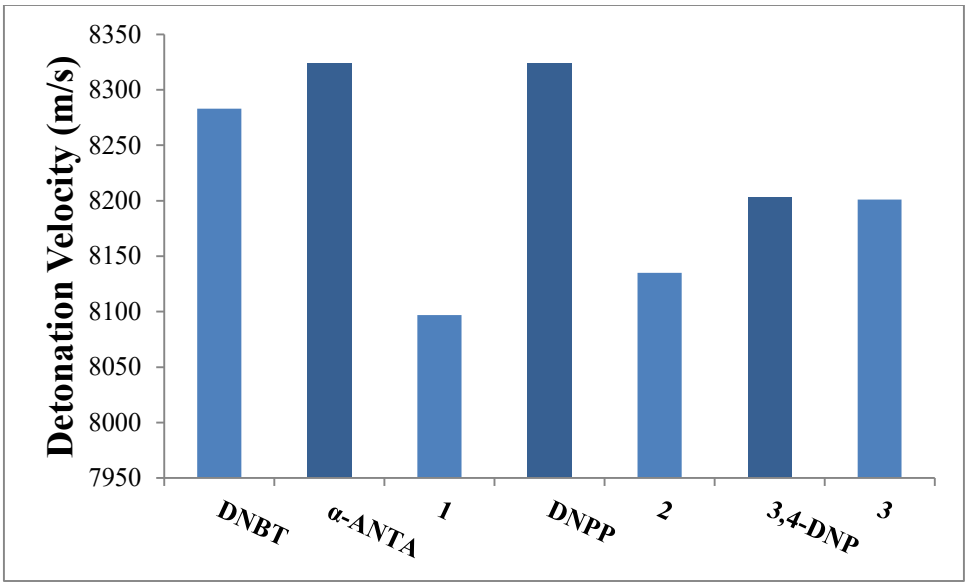

Figure 2.6 Detonation velocities of each pure component and DNBT cocrystal **1-3**, are predicted with Cheetah 6.0 software and use the room temperature (298 K) crystallographic densities of each material.

The sensitivity of an explosive is critical; however, only materials with sufficient explosive power merit further development. The thermochemical code Cheetah 6.0, using the Sandia JCZS product library revision 32, allows for the prediction of the detonation velocities of novel energetic materials or formulations utilizing chemical (formula, density) and thermodynamic (heat of formation) properties of the components. Using the room temperature densities for each material, the detonation velocities were predicted for cocrystals **1-3** and all pure solid components (Figure 2.6) with all three of the cocrystals predicted to have high detonation velocities of >8000 m/s. Cocrystals **1** (8097 m/s) and **2** (8135 m/s) have predicted detonation velocities lower than each of their pure components DNBT (8283 m/s), ANTA (8324 m/s) and DNPP (8324 m/s). This result is expected due to the dependency of the detonation velocity on density and taking into account the finding that both cocrystals **1** and **2** each have densities lower than those of either of their pure components. Conversely, cocrystal **3** possesses a detonation velocity of 8201 m/s that is comparable to its one pure component 3,4-DNP with a detonation

velocity of 8203 m/s. This material not only has a density improved in relation to 3,4-DNP, but **3** is not expected to see loss in power compared to the pure component. This new cocrystal possess the power of the pure component while having a drastically decreased impact sensitivity, which can all be attributed to the greater degree of hydrogen bonding in the cocrystal and the same hydrogen bonding synthon seen among all three of the DNBT cocrystals.

2.3 Conclusion

In summary, three novel energetic cocrystals of DNBT (2:1 cocrystal of ANTA (**1**), a 1:1 cocrystal of DNPP (**2**) and a 2:1 cocrystal of 3,4-DNP (**3**)) have been discovered all exhibiting the same hydrogen bonding motif in their structures. These cocrystals should be attractive ingredients for future explosive formulations. These cocrystals showcase the importance of crystal engineering in energetic cocrystals and the potential for further development of reliable interaction for the formation of energetic cocrystals. The azole family of energetics has shown great promise as energetic cocrystal formers, and the synthon used for the formation of cocrystals **1-3** will be a valuable tool for the design of additional cocrystalline materials of energetics.

2.4 Experimental Procedures

2.4.1 Materials

Acetonitrile (Certified ACS) was obtained from Fisher Scientific and dried over 4 Å molecular sieves. 5,5'-Dinitro-2H,2H'-3,3'-bi-1,2,4-triazole (DNBT), 5-amino-3-nitro-1H-1,2,4-triazole (ANTA), 1H,4H-3,6-dinitropyrazolo[4,3-c]pyrazole (DNPP) and 3,4-dinitropyrazole (3,4-DNP) were received from Lawrence Livermore National Labs. ***Caution!*** *Although no unplanned detonations were encountered during this work, DNBT, α-ANTA, DNPP and 3,4-DNP are all dangerous high explosives. Proper safety practices and equipment was used to prevent an*

explosion due to friction, heat, static shock, or impact. Be aware that the potential for severe injury exists if these materials are handled improperly.

2.4.2 Crystallization

All cocrystals of DNBT (**1**-**3**) were initially obtained from acetonitrile solutions, with the stoichiometric ratio of the pure components (2:1, 1:1 and 2:1 respectively), by slow evaporation and then conditions for their pure growth was determined, see below.

*2:1 ANTA/DNBT (**1**)*

A glass vial was loaded with 7.63 mg of DNBT (0.0338 mmol) and 8.72 mg ANTA (0.0675 mmol), which were subsequently dissolved with 2.3 mL of dry acetonitrile and 0.2 mL of dry acetone. Sonication was used to ensure dissolution, before the solution was filtered through a 0.45 μm PTFE filter into a 4 mL glass vial. The cap on the vial was left loose to allow for slow evaporation of the solvent. After six days at room temperature colorless plates formed on the bottom and side of the vial and were determined to be the 2:1 ANTA:DNBT cocrystal by both Raman spectroscopy and powder X-ray diffraction.

*1:1 DNPP/DNBT (**2**)*

A glass vial was loaded with 7.63 mg of DNBT (0.0338 mmol) and 6.69 mg DNPP (0.0338 mmol), which were subsequently dissolved with 1.4 mL of dry acetonitrile. Sonication was used to ensure dissolution, before the solution was filtered through a 0.45 μm PTFE filter into a 4 mL glass vial. The cap on the vial was left loose to allow for slow evaporation of the solvent. After five days at room temperature colorless plates formed on the bottom of the vial and were determined to be the 1:1 DNPP/DNBT cocrystal by both Raman spectroscopy and powder X-ray diffraction.

*2:1 3,4-DNP/DNBT (**3**)*

A glass vial was loaded with 22.6 mg of DNBT (0.100 mmol) and 31.6 mg 3,4-DNP (0.200 mmol), which were subsequently dissolved with 0.25 mL of dry isopropanol. Sonication was used to ensure dissolution, before the solution was filtered through a 0.45 μm PTFE filter into a 4 mL glass vial. The cap on the vial was left loose to allow for slow evaporation of the solvent. After one day at room temperature colorless plates formed on the bottom of the vial and were determined to be the 2:1 3,4-DNP:DNBT cocrystal by both Raman spectroscopy and powder X-ray diffraction.

The cocrystal synthesis could be scaled up conveniently with the use of solvent mediated transformation in a slurry of the pure components at room temperature. For example, the cocrystal **2** was obtained by loading a glass vial with 11.31 mg of DNBT (0.050 mmol), 9.91 mg DNPP (0.050 mmol) and 0.2 mL of dry isopropanol. The vial was sealed and shaken gently for 2 days, during which time the pure components of DNBT and DNPP had disappeared and a white powder had appeared. This solid was determined to be the 1:1 DNBT:DNPP cocrystal by both Raman spectroscopy and powder X-ray diffraction.

2.4.3 Raman Spectroscopy

Raman spectra were collected using a Renishaw inVia Raman Microscope equipped with a Leica microscope, 633 nm laser, 1800 lines/mm grating, 50 μm slit and a RenCam CCD detector. Spectra were collected in extended scan mode with a range of 100-4000 cm^{-1} and then analyzed using the WiRE 3.4 software package (Renishaw). Calibration was performed using a silicon standard.

2.4.4 Powder X-ray Diffraction (PXRD)

Powder X-ray diffraction patterns were collected on a Bruker D8 Advance diffractometer using Cu-Kα radiation (λ = 1.54187 Å) and operating at 40 kV and 40 mA. Samples were

prepared by finely grinding and packing into the depression of a glass slide. The spectrum was collected by scanning 2θ from 4° to 70° with a step size of 0.02° and a step speed of 0.5 seconds. Powder patterns were processed using Jade 8 XRD Pattern Processing, Identification & Quantification analysis software (Materials Data, Inc.).[34] All powder patterns were compared to their respective simulated powder patterns from the single crystal X-ray diffraction structures and were found to be in substantial agreement with the predicted patterns.

2.4.5 Single Crystal Structure Determination

Single crystal X-ray diffraction data for cocrystals **1-3** were collected using a Rigaku AFC10K Saturn 944+ CCD-based X-ray diffractometer equipped with a low temperature device and Micromax-007HF Cu-target micro-focus rotating anode (λ = 1.54187 Å) operated at 1.2 kW power (40 kV, 30 mA). The X-ray intensities were measured at 85(1) K with the detector placed at a distance 42.00 mm from the crystal. The data was processed with CrystalClear 2.0 (Rigaku)[35] and corrected for absorption. The structures were solved and refined with the Bruker SHELXTL (version 2008/4)[36] software package using direct methods. All non-hydrogen atoms were refined anisotropically with the hydrogen atoms placed in a combination of refined and idealized positions.

2.4.6 Differential Scanning Calorimetry (DSC)

Thermograms of each sample were recorded on a TA Instruments Q20 DSC. All experiments were run in Tzero™ hermetic aluminum DSC pans and studied under a nitrogen purge with a heating rate of 10 °C/min, while covering the temperature range of 35 °C to 350 °C. Calibration of the instrument was performed using an indium standard. Thermograms were analyzed using TA Universal Analysis 2000, V 4.5A.

2.5 References

1. Schultheiss, N.; Newman, A., Pharmaceutical Cocrystals and Their Physicochemical Properties. *Cryst. Growth Des.* **2009,** *9*, 2950-2967.

2. Sanphui, P.; Goud, N. R.; Khandavilli, U. B. R.; Nangia, A., Fast Dissolving Curcumin Cocrystals. *Cryst. Growth Des.* **2011,** *11*, 4135-4145.

3. Porter III, W. W.; Elie, S. C.; Matzger, A. J., Polymorphism in Carbamazepine Cocrystals. *Cryst. Growth Des.* **2008,** *8*, 14-16.

4. Fleischman, S. G.; Kuduva, S. S.; McMahon, J. A.; Moulton, B.; Bailey Walsh, R. D.; Rodríguez-Hornedo, N.; Zaworotko, M. J., Crystal Engineering of the Composition of Pharmaceutical Phases: Multiple-Component Crystalline Solids Involving Carbamazepine. *Cryst. Growth Des.* **2003,** *3*, 909-919.

5. Koshima, H.; Miyamoto, H.; Yagi, I.; Uosaki, K., Preparation of Cocrystals of 2-Amino-3-nitropyridine with Benzenesulfonic Acids for Second-Order Nonlinear Optical Materials. *Cryst. Growth Des.* **2004,** *4*, 807-811.

6. Sun, A.; Lauher, J. W.; Goroff, N. S., Preparation of Poly(diiododiacetylene), an Ordered Conjugated Polymer of Carbon and Iodine. *Science* **2006,** *312*, 1030-1034.

7. Yan, D.; Delori, A.; Lloyd, G. O.; Friščić, T.; Day, G. M.; Jones, W.; Lu, J.; Wei, M.; Evans, D. G.; Duan, X., A Cocrystal Strategy to Tune the Luminescent Properties of Stilbene-Type Organic Solid-State Materials. *Angew. Chem. Int. Ed.* **2011,** *50*, 12483-12486.

8. Sokolov, A. N.; Friščić, T.; MacGillivray, L. R., Enforced Face-to-Face Stacking of Organic Semiconductor Building Blocks within Hydrogen-Bonded Molecular Cocrystals. *J. Am. Chem. Soc.* **2006,** *128*, 2806-2807.

9. Kapadia, P. P.; Ditzler, L. R.; Baltrusaitis, J.; Swenson, D. C.; Tivanski, A. V.; Pigge, F. C., Semiconducting Organic Assemblies Prepared from Tetraphenylethylene Tetracarboxylic Acid and Bis(pyridine)s via Charge-Assisted Hydrogen Bonding. *J. Am. Chem. Soc.* **2011,** *133*, 8490-8493.

10. Sato, S.; Nikawa, H.; Seki, S.; Wang, L.; Luo, G.; Lu, J.; Haranaka, M.; Tsuchiya, T.; Nagase, S.; Akasaka, T., A Co-Crystal Composed of the Paramagnetic Endohedral Metallofullerene La@C82 and a Nickel Porphyrin with High Electron Mobility. *Angew. Chem. Int. Ed.* **2012,** *51*, 1589-1591.

11. Landenberger, K. B.; Matzger, A. J., Cocrystal Engineering of a Prototype Energetic Material: Supramolecular Chemistry of 2,4,6-Trinitrotoluene. *Cryst. Growth Des.* **2010,** *10*, 5341-5347.

12. Landenberger, K. B.; Matzger, A. J., Cocrystals of 1,3,5,7-Tetranitro-1,3,5,7-tetrazacyclooctane (HMX). *Cryst. Growth Des.* **2012,** *12*, 3603-3609.

13. Millar, D. I. A.; Maynard-Casely, H. E.; Allan, D. R.; Cumming, A. S.; Lennie, A. R.; Mackay, A. J.; Oswald, I. D. H.; Tang, C. C.; Pulham, C. R., Crystal engineering of energetic materials: Co-crystals of CL-20. *CrystEngComm* **2012,** *14*, 3742-3749.

14. Bolton, O.; Simke, L. R.; Pagoria, P. F.; Matzger, A. J., High Power Explosive with Good Sensitivity: A 2:1 Cocrystal of CL-20:HMX. *Cryst. Growth Des.* **2012,** *12*, 4311-4314.

15. Bolton, O.; Matzger, A. J., Improved Stability and Smart-Material Functionality Realized in an Energetic Cocrystal. *Angew. Chem. Int. Ed.* **2011,** *50*, 8960-8963.

16. Zhang, H.; Guo, C.; Wang, X.; Xu, J.; He, X.; Liu, Y.; Liu, X.; Huang, H.; Sun, J., Five Energetic Cocrystals of BTF by Intermolecular Hydrogen Bond and π-Stacking Interactions. *Cryst. Growth Des.* **2012,** *13*, 679-687.

17. Yang, Z.; Wang, Y.; Zhou, J.; Li, H.; Huang, H.; Nie, F., Preparation and Performance of a BTF/DNB Cocrystal Explosive. *Propell. Explos. Pyrotech.* **2014,** *39*, 9-13.

18. Yang, Z.; Li, H.; Zhou, X.; Zhang, C.; Huang, H.; Li, J.; Nie, F., Characterization and Properties of a Novel Energetic–Energetic Cocrystal Explosive Composed of HNIW and BTF. *Cryst. Growth Des.* **2012,** *12*, 5155-5158.

19. Wang, Y.; Yang, Z.; Li, H.; Zhou, X.; Zhang, Q.; Wang, J.; Liu, Y., A Novel Cocrystal Explosive of HNIW with Good Comprehensive Properties. *Propell. Explos. Pyrotech.* **2014,** *39*, 590-596.

20. Landenberger, K. B.; Bolton, O.; Matzger, A. J., Two Isostructural Explosive Cocrystals with Significantly Different Thermodynamic Stabilities. *Angew. Chem. Int. Ed.* **2013,** *52*, 6468-6471.

21. Landenberger, K. B.; Bolton, O.; Matzger, A. J., Energetic-Energetic Cocrystals of Diacetone Diperoxide (DADP): Dramatic and Divergent Sensitivity Modifications via Cocrystallization. *J. Am. Chem. Soc.* **2015,** *137*, 5074-5079.

22. Bagal, L. I.; Pevzner, M. S.; Frolov, A. N.; Sheludyakova, N. I., Heterocyclic Nitro Compounds. *J. Org. Chem. USSR (Engl. Transl.)* **1970,** *6*, 259-264.

23. Nikitina, E. V.; Starova, G. L.; Frank-Kamenetskaya, O. V.; Pevzner, M. S., 3,3'-Dinitro-5,5'-bi(1,2,4-triazole) dihydrate CIF. *Kristallografiya(Russ.)(Crystallogr.Rep.)* **1982,** *27*, 485.

24. *Although the crystallographic density may be high for a hydrate the dilution of the energetic by the presence of water reduces the effective density of the energetic component.*

25. Lee, K. Y.; Storm, C. B.; Hiskey, M. A.; Coburn, M. D., An improved synthesis of 5-amino-3-nitro-1H-1,2,4-triazole (ANTA), a useful intermediate for the preparation of insensitive high explosives. *J. Energetic Mater.* **1991,** *9*, 415-428.

26. Pagoria, P. F.; Lee, G. S.; Mitchell, A. R.; Schmidt, R. D., A review of energetic materials synthesis. *Thermochim. Acta* **2002,** *384*, 187-204.

27. Simpson, R. L.; Pagoria, P. F.; Mitchell, A. R.; Coon, C. L., Synthesis, Properties and Performance of the High Explosive ANTA. *Propell. Explos. Pyrotech.* **1994,** *19*, 174-179.

28. Shevelev, S. A.; Dalinger, I. L.; Shkineva, T. K.; Ugrak, B. I.; Gulevskaya, V. I.; Kanishchev, M. I., Nitropyrazoles. *Russ Chem Bull* **1993,** *42*, 1063-1068.

29. Janssen, J. W. A. M.; Koeners, H. J.; Kruse, C. G.; Habrakern, C. L., Pyrazoles. XII. Preparation of 3(5)-nitropyrazoles by thermal rearrangement of N-nitropyrazoles. *J. Org. Chem.* **1973,** *38*, 1777-1782.

30. *Distances are calculated in Mercury 3.3 from the CIFs at 85 K with the N-H hydrogens normalized at 1.015 Å.*

31. *Molecular volumes are calculated in Spartan14 V1.1.2 by determining the equilibrium geometry at the ground state for structures of the pure components with the semi-empirical AM1 method.*

32. Zhang, C.; Wang, X.; Huang, H., π-Stacked Interactions in Explosive Crystals: Buffers against External Mechanical Stimuli. *J. Am. Chem. Soc.* **2008,** *130*, 8359-8365.

33. Ma, Y.; Zhang, A.; Zhang, C.; Jiang, D.; Zhu, Y.; Zhang, C., Crystal Packing of Low-Sensitivity and High-Energy Explosives. *Cryst. Growth Des.* **2014,** *14*, 4703-4713.

34. Jade Plus 8.2 ed.: Materials Data, Inc., 1995-2007.

35. CrystalClear Expert 2.0 r12, Rigaku Americas and Rigaku Corporation (2011): Rigaku Americas, 9009, TX, USA 77381-5209, Rigaku Tokyo, 196-8666, Japan.

36. Sheldrick, G.M. SHELXTL, v. 2008/4; Bruker Analytical X-ray: Madison, WI, 2008.

Chapter 3: Isostructural Cocrystals of 1,3,5-Trinitrobenzene Assembled by Halogen Bonding

Published: Bennion, J.C.; Vogt, L.; Tuckerman, M.E.; Matzger, A. J., *Cryst. Growth Des.*, **2016**, *16*, (8), 4688-4693.

3.1 Introduction

In the fields of pharmaceuticals,[1-4] organic semiconductors,[5-7] non-linear optical materials[8-10] and more recently in energetic materials (propellants, explosives and pyrotechnics),[11-13] the crystal engineering tool of cocrystallization has been applied broadly for the manipulation of a materials physical properties. Energetic cocrystals form through noncovalent interactions between two or more neutral molecular components, which ultimately alter the physical properties of the pure coformers[14-16]; the density and melting/decomposition temperatures differ in the cocrystal, directly impacting performance criteria including impact sensitivity, thermal stability, and detonation velocity. Due to the noncovalent interactions in the cocrystal, the new material is distinct from both pure coformers and from a physical mixture of the two coformers.

Progress in the field of energetic cocrystals has led to several new materials, derived from two energetic components, discovered since 2011 and these materials typically display various hydrogen bonding (HB) motifs between the two coformers.[14-22] The major challenge with utilizing hydrogen bonding for the crystal engineering of energetic cocrystals is that most energetics lack traditional hydrogen bond donors and acceptors (carbonyl, hydroxyl, amine, carboxylic acid, etc.), and thus prediction of the hydrogen bonding interactions between single components is problematic. An alternative to hydrogen bonding interactions that is gaining more traction as a crystal engineering tool for energetic materials is halogen bonding (XB). Halogen

bonding occurs between a nucleophile and the σ-hole of a highly polarized halogen atom; the σ-hole is a region of positive electrostatic potential, whose size and strength increases upon descending the periodic table (Cl < Br < I).[23] Figure 3.1 shows that the σ-hole in the 1,3,5-trihalo-2,4,6-trinitrobenzene series (TXTNB, where X = I, Br, or Cl) varies with the halogen substituent, suggesting that this series of compounds is useful to explore halogen bonding in energetic cocrystals. The first example of halogen bonding in energetic cocrystals was 1:1 DADP/TITNB (diacetone diperoxide and 1,3,5-triiodo-2,4,6-trinitrobenzene),[21] in which the iodo-peroxide interaction, the first of its kind, is thought to be a crucial force in the stabilization of the cocrystal.

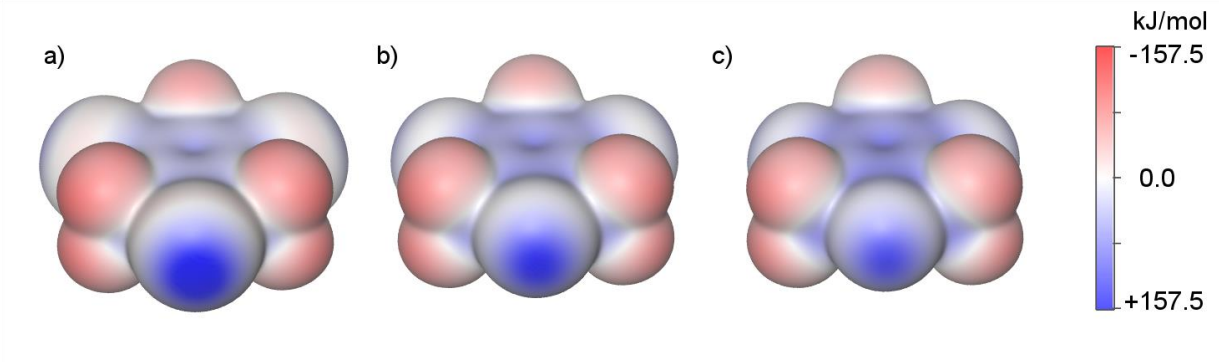

Figure 3.1 Electrostatic potential at the molecular surface (ρ=0.002 a.u.) for a) TITNB, b) TBTNB, and c) TCTNB calculated using Density Functional Theory (see Methods for details). The oxygens of the nitro group are shown in red and the halogen atoms (I, Br, and Cl) are shown in blue.

Several halogen-containing energetics are already known in the field, such as 3,3,7,7-tetrakis(difluoramino)octahydo-1,5-dinitro-1,5-diazocine (HNFX), octafluoropentaerythrityltetramine (octafluoro-PETA)[24] and 1,3,5-trichloro-2,4,6-trinitrobenzene (TCTNB) and these compounds are of immense interest due to the known biocidal activity of halogenated energetics and their potential use as countermeasures for biowarfare agents. Iodine is generally regarded as the most potent biocide and with this in mind the energetic TITNB was first synthesized in 2015; since its discovery it has been shown to possess the largest σ-hole of

halogenated aromatic compounds[25] and therefore is of interest as a supramolecular building block. TITNB is a very impact sensitive energetic [Dh_{50} of 29 cm compared to 55 cm for HMX (octahydro-1,3,5,7-tetranitro-1,3,5,7-tetrazocine) and 29 cm for CL-20 (2,4,6,8,10,12-hexanitro-2,4,6,8,10,12-hexaazaisowurtzitane)][15] and could see improvements in its physical properties through cocrystallization. The cocrystal of DADP/TITNB showed, for the first time, two primary energetics (extremely sensitive to external stimuli and needs only a small amount of energy input to cause detonation) cocrystallizing to make a secondary energetic (relatively insensitive to external stimuli and typically needs a primary energetic to cause detonation).[21] Both TCTNB and 1,3,5-tribromo-2,4,6-trinitrobenzene (TBTNB) are less sensitive to impact (Dh_{50} of 94 cm for both)[21] than TITNB, and like TITNB form 1:1 cocrystals with DADP.[17] The DADP cocrystals are, however, of relatively low performance and too sensitive for what is currently needed in insensitive munitions. Therefore the TXTNB series was chosen for cocrystallization with a traditional energetic material to test the reliability and robustness of halogen bonding for energetic cocrystal formation and to expand the utility of these biocidal energetics. For this study of halogen bonding in energetic materials, 1,3,5-trinitrobenzene (TNB) was selected as the traditional energetic coformer. TNB is an energetic that possesses superior power to 2,4,6-trinitrotoluene (TNT) and similarly is an insensitive explosive (*vide infra*).[26]

3.2 Results and Discussion

Two novel cocrystals of TNB with TITNB and TBTNB are described here. The materials form in a 2:1 molar ratio of TNB with each TXTNB (see Figure 3.2a and 3.2b for pure component structures where X = I or Br respectively) and are isostructural. The formation of these cocrystals is aided by halogen bonding between the TNB and the respective TXTNB (X = I or Br). This is the first example of halogen bonding with traditional energetic materials and the $NO_2\cdots X$

interaction this approach utilizes is ripe for application to the further development of novel energetic-energetic cocrystals.

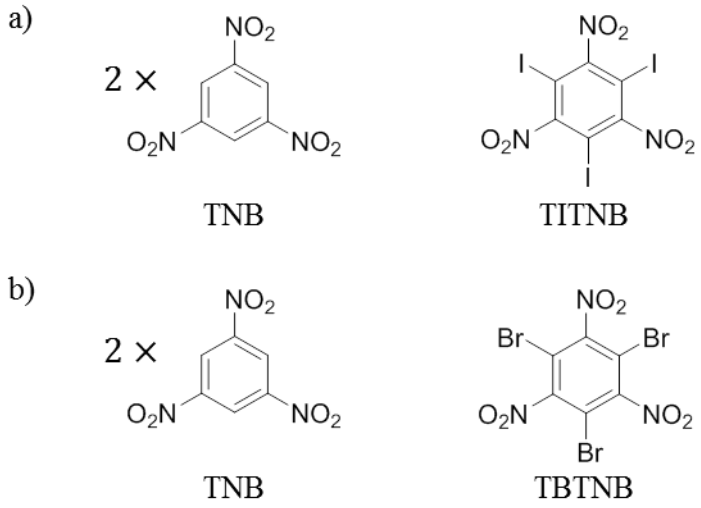

Figure 3.2 Chemical structures of the pure components for both TNB cocrystals **1** and **2**: (a) 2:1 TNB/TITNB cocrystal (**1**), chemical structures of TNB and TITNB; (b) 2:1 TNB/TBTNB cocrystal (**2**), chemical structures of TNB and TBTNB.

Cocrystals **1** and **2** (2:1 TNB/TITNB and 2:1 TNB/TBTNB, respectively) were both formed initially from acetonitrile solutions and alternatively from isopropanol or ethanol. Based on computational results (see below), several attempts were made at the formation of a third cocrystal between TNB and TCTNB under both thermodynamic and kinetic conditions, but no cocrystallization was observed between those components in this study. Cocrystal **1** exhibits a prismatic habit, whereas **2** typically exhibits a plate habit. Raman spectroscopy and powder X-ray diffraction (PXRD) can definitively differentiate cocrystals **1** and **2** from the pure forms of TNB and the cocrystal formers TITNB and TBTNB (see Appendix B). The crystal structures of **1** and **2** were elucidated and the crystallographic data are presented in Table 3.1. Both cocrystals have high crystallographic densities: cocrystal **1** has a density of 2.263 g/cm^3 at 85 K (2.203 g/cm^3 at 298 K), and cocrystal **2** has a density of 2.041 g/cm^3 at 85 K (1.980 g/cm^3 at 298 K). Therefore, cocrystals **1** and **2** have densities that are between those of their respective coformers,

with both having superior densities to that of their shared pure component TNB (1.676 g/cm^3). It should be noted that while both of these materials have high crystallographic densities, this is partially due in part to the presence of the heavy halogen atoms. DSC analysis on TNB cocrystals and their respective coformers show thermal sensitivity similar to that of other secondary energetics, decomposition occurs at 320 °C for **1** and 340 °C for **2** (see the DSC analysis in the Appendix B).

Table 3.1 Crystallographic Data for TNB Cocrystals (Collected at 85 K)

TNB Cocrystal	**1**	**2**
Stoichiometry	2:1	2:1
Morphology	Prism	Plate
Space Group	Pbcn	Pbcn
a (Å)	32.174(2)	30.451(2)
b (Å)	9.8384(2)	9.6013(2)
c (Å)	9.4308(2)	9.7519(2)
Volume (Å^3)	2985.2(2)	2851.1(2)
Z	4	4
ρ_{calc} (g/cm^3)	2.263	2.041
Data/Parameter	2739/219	2613/219
R_1/wR_2	2.57/5.93	7.94/20.69
GOF	1.124	1.181

The TNB cocrystals rely on the formation of similar halogen bonding interactions between the halogen atoms, I or Br, attached to the aromatic rings on the TXTNB coformer and the nitro groups of both components (Figure 3.3 and 3.4 for cocrystals **1** and **2**, respectively).[27] The shortest halogen bond interactions in each of the two TNB cocrystals is seen between the NO_2 of the TNB and X of the TXTNB and is measured to be 2.93 and 2.90 Å for **1** and **2,** respectively; these represent the shortest nitro-iodo (n = 111) and second shortest nitro-bromo (n = 265) interactions seen in the Cambridge Structural Database (CSD) for organohalides.[28] In both cocrystals, the TXTNB component forms linear tapes by chelation from the nitro group to the

halogen, which propagates throughout the crystal structure, and these tapes are flanked by TNB molecules which interact with the open halogen atoms forming into a larger tape (Figure 3.3a-b and 3.4a-b). Due to the larger size of the σ-hole on the iodine atom (Figure 3.1a), one TITNB (Figure 3.3a) molecule interacts with four TNB molecules (2.93 and 3.50 Å), while the smaller σ-hole on the bromine atom (Figure 3.1b) of TBTNB (Figure 3.4a) allows only two close halogen bonding interactions with TNB (2.90 Å). This is a direct result of the differences in the size of the van der Waals radii of iodine and bromine, where the adjacent interaction at 3.50 Å in **1** is within the sum of the respective van der Waals radii. These larger tapes form infinite stacks through π-stacking interactions between the aromatic rings/nitro groups of the coformers, and ultimately form a herringbone-like structure through interactions between the stacking groups (Figure 3.3c and 3.4c). The observed differences in the halogen bonding interactions of **1** and **2**, I and Br, could explain why no cocrystal with TCTNB has been discovered since the σ-hole is increasingly smaller with the smaller and less polarizable Cl atoms (Figure 3.1c).

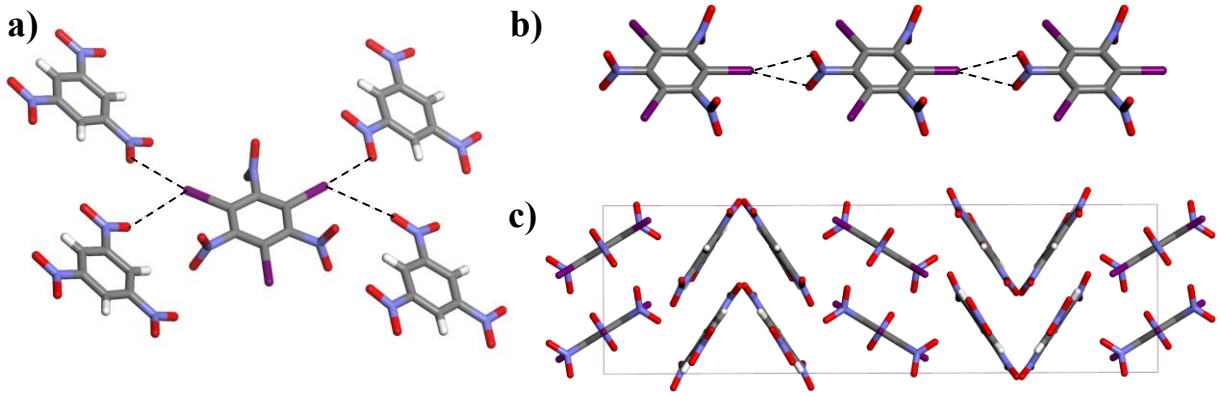

Figure 3.3 The TNB/TITNB cocrystal. a) Halogen bonding interaction between the nitro and iodine of the coformers. b) Infinite tape of TITNB iodine-nitro interactions in TNB/TITNB. c) Unit cell viewing down the b-axis.

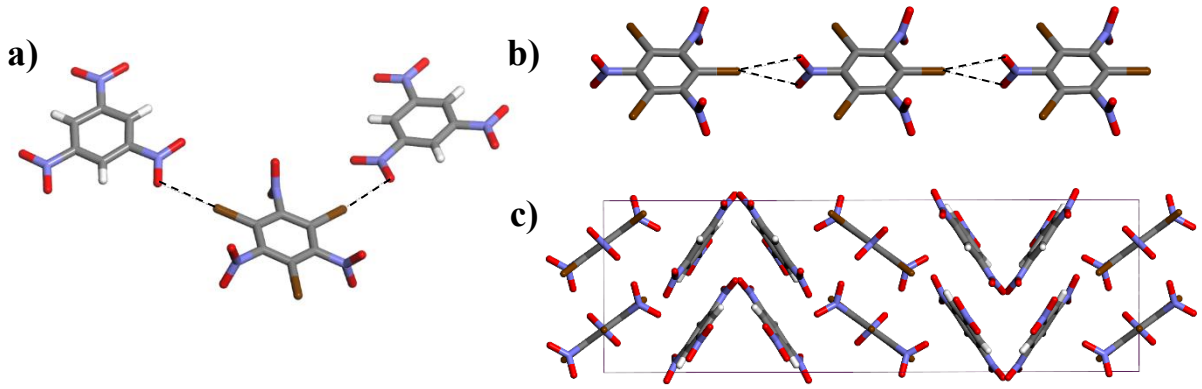

Figure 3.4 The TNB/TBTNB cocrystals. a) Halogen bonding interaction between the nitro and bromine of the coformers. b) Infinite tape of TBTNB bromine-nitro interactions in TNB/TBTNB. c) Unit cell viewing down the b-axis.

To investigate the halogen-nitro bonding capability of the reported coformers, the electrostatic potentials at the molecular surfaces of TITNB, TBTNB, and TCTNB were calculated using density functional theory (DFT). Each molecule was optimized in a 20 $Å^3$ bounding box using the Gaussian and plane wave (GPW) scheme[29] of the QUICKSTEP package[30] in CP2K v. 2.6.2.[31] The PBE exchange-correlation functional[32] with the D3(BJ) dispersion correction[33, 34] was used with a cutoff of 18 Å. Calculations employed the DZVP-MOLOPT-GTH (m-DZVP) basis set for H, C, N, O, and Cl and the DZVP-MOLOPT-SR-GTH basis set for Br and I,[35] paired with appropriate dual-space GTH pseudopotentials[36] optimized for the PBE functional.[37] To further explore why no cocrystal of TNB/TCTNB was observed, the relative lattice energy for each 2:1 TNB/TXTNB (X = I, Br, or Cl) cocrystal was calculated using the same method to optimize the periodic crystal structures of the coformers and cocrystals. Further computational details and the optimized cell parameters can be found in the Appendix B.

For each of the 2:1 TNB/TXTNB cocrystals, the lattice energy of the cocrystal was calculated to be more stable than the net lattice energy of the pure component crystals. The relative lattice energies for the cocrystals are -11.5, -8.2, and -8.5 kJ/mol for X = I, Br, and Cl, respectively. As seen in Figure 3.5, optimized lattice parameters for all isostructural cocrystals are similar. The

greater favorability of the TITNB cocrystal is also supported by the experimental observation that it forms much more readily in slurries than the TBTNB cocrystal. The favorable relative lattice energy for all three systems suggests that an isostructural 2:1 TNB/TCTNB cocrystal could form experimentally, and therefore the cocrystallization methods were expanded to include crystallization via slow evaporation, pseudoseeding of a supersaturated solution, and slurry in various solvents (acetonitrile, ethanol, isopropanol, etc.) at various temperatures (4, 22 and 50 °C). No cocrystal of TNB/TCTNB in any ratio was obtained under these conditions, but a physical mixture of TCTNB and TNB form 3 was observed by Raman spectroscopy and PXRD when seeding a supersaturated coformer solution with either **1** or **2**. In almost all crystallizations involving TNB, a pure phase is dominated by TNB form 1 and as such the presence of TNB form 3 in the crystallization with TCTNB is atypical. This result suggests that heteroseeding with either **1** or **2** may facilitate growth of coformer domains rather than a cocrystal due to similar lattice parameters for the rarely observed TNB form 3[38] and TCTNB with the TNB/TXTNB cocrystals.

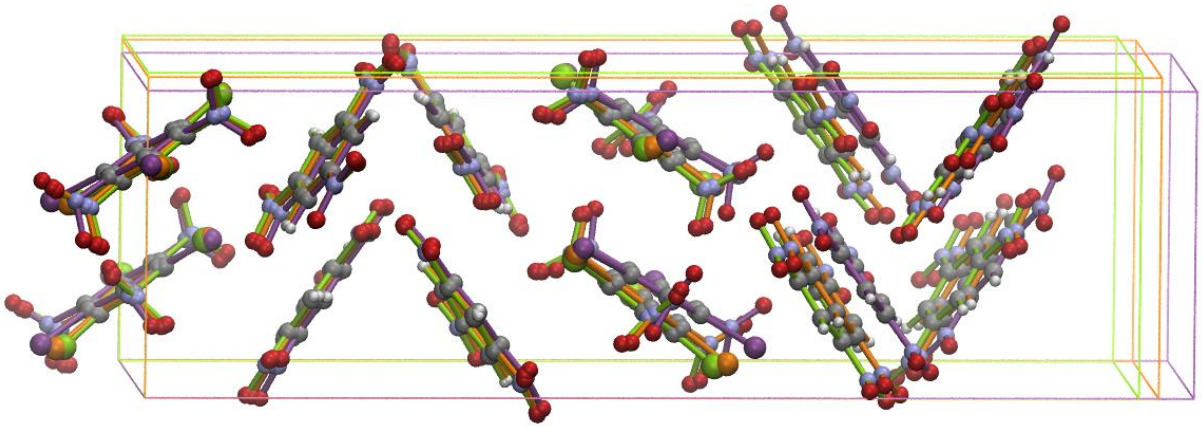

Figure 3.5 DFT-optimized unit cells of 2:1 TNB/TXTNB cocrystals, where X = I (purple), Br (orange), or Cl (green).

To determine how efficiently each material occupies the volume of the unit cell, the packing coefficient (C_k), the total molecular volume in a unit cell divided by the unit cell volume, was determined for each of the cocrystals and for the pure components (Figure 3.6).[39] For cocrystals **1** (74.0%) and **2** (74.6%) the packing coefficients are lower than that of the pure component TNB (77.9%), but both achieve a C_k higher than that of their pure TXTNB components: TITNB (68.4%) and TBTNB (69.9%). The similarity in the packing coefficients of the cocrystals is in line with expectations given the fact that these materials are isostructural, and this has been seen before for the isostructural 1:1 DADP/TCTNB and 1:1 DADP/TBTNB cocrystals.[21] This increase in the C_k of the cocrystals compared to the respective TXTNB coformer is attributed to the close halogen bond interactions between the TNB and TXTNB coformers, compared to the pure TXTNB coformers. Additionally the herringbone-like packing of the cocrystals is thought to contribute to the significant increase in the packing coefficients when compared to sheet packing seen in the pure components TITNB and TBTNB.

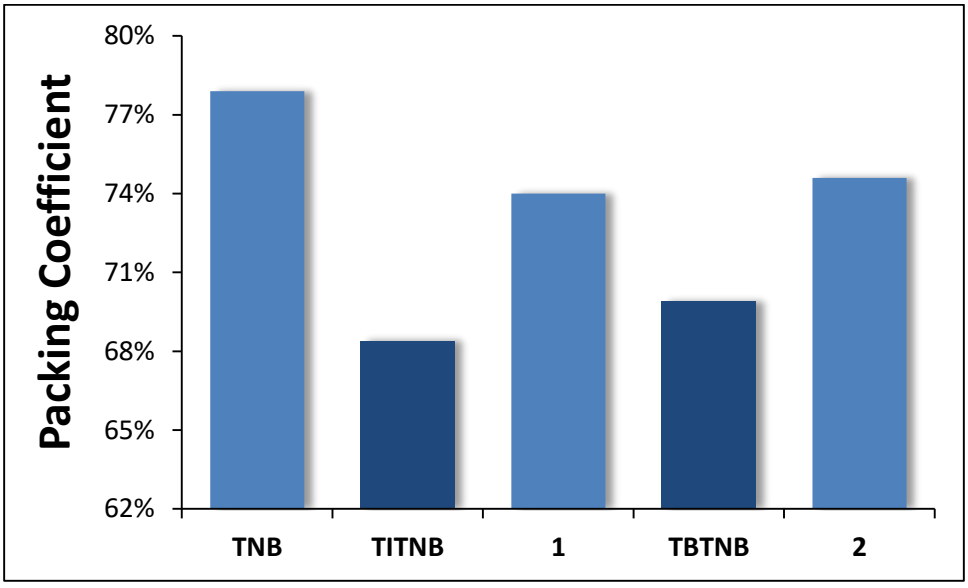

Figure 3.6 Packing coefficients (C_k) of each pure component and TNB cocrystals **1** and **2**, are calculated from the room temperature (298 K) crystal lattices of each material.

The sensitivity of the isostructural energetic materials **1** and **2** was determined by small-scale impact drop testing, in which only a small amount of material, approximately 2 mg (± 10%), is required for each measurement.[15, 21, 22] A reproducible Dh_{50} is obtained by striking the energetic samples, contained within nonhermetic differential scanning calorimetry (DSC) pans, with a freefalling 5 lb drop weight from heights of variable distance on approximately 20 trials per material. Two well-known materials, ε-CL-20 and β-HMX, have been tested on this apparatus and for reference exhibit a 50% probability of detonation in this apparatus when impacted from heights of 29 and 55 cm, respectively. The sensitivity to impact of all pure components and cocrystals **1** and **2** was determined. For the common component of both cocrystals, TNB, the Dh_{50} was determined to be >145 cm, the max height of the apparatus, and as such is classified as insensitive. The TXTNBs on the other hand were found to be much more sensitive compared to TNB: TITNB (29 cm) and TBTNB (94 cm). Cocrystallization of these components resulted in both **1** (77 cm) and **2** (103 cm) possessing sensitivity between that of their respective pure coformers. Both materials can be preliminarily classified as secondary explosives and the decrease in the impact sensitivity can be potentially attributed to the increase in the strength of halogen bonding interactions, as well as the π-stacking interactions in the cocrystals. The sensitivity of an energetic material is generally associated with both the inter-/intra- molecular interactions and the packing of the molecules in the crystal.[40] Cocrystal **1** is an important example of cocrystallization being able to take a very sensitive material like TITNB and drastically reducing its sensitivity to impact.

One place where these novel cocrystalline energetic materials could see an application is as biocidal energetics. Some of the most dangerous weapons that can be deployed on the front lines or on the home front are bioweapons, such as anthrax (*bacillus anthracis*), and as a result

considerable research has gone into finding a way to neutralize these materials in fortified stockpiles rather than simply dispersing them with conventional weapons. Two of the ways that have been developed to neutralize such bioweapons include utilizing materials that generate high temperatures (i.e. thermites) and/or halogen containing materials/energetics that will generate X_2/HX upon decomposition, both of which will destroy the bioweapons.[41-44] For organic materials, the generation of X_2/HX is typically accomplished through formulations that will generate HCl/Cl_2 or HF from an energetic such as HNFX.[45] Perchlorates are typically used for the generation of chlorine and have albeit with the drawbacks of chlorine being a poor biocidal agent and the toxicity of the perchlorates. Fluorine on the other hand is a very good biocide, but is more likely to form the C-F bond than the H-F bond. Additionally, the sources of fluorine, HNFX or octafluoro-PETA, have several key drawbacks (HNFX has high sensitivity/low density and octafluoro-PETA is highly volatile) that have kept these materials from making a broader impact.[46] Both bromine (HBr/Br_2) and iodine (HI/I_2) have been shown to have great biocidal activity[47-50], and both cocrystals **1** and **2** contain high weight percents (37.4 and 27.4) of the respective halogens. Given the abundance of halogen atoms in the cocrystals and the relative insensitivity compared to HNFX, both **1** and **2** could see application as an insensitive biocidal energetics.

3.3 Conclusion

In summary, two isostructural energetic cocrystals of TNB (2:1 cocrystal with TITNB (**1**) and 2:1 cocrystal with TBTNB (**2**)) have been discovered whose formation relies on the same halogen bonding motif between the respective components. These halogen-containing cocrystals should be attractive ingredients for future munition formulations and have potential as insensitive biocidal materials. Computational evaluation of relative lattice energies played a vital role in

guiding the experimental search for isostructural cocrystalline materials and predicts that a 2:1 cocrystal with TNB and TCTNB should exist if suitable synthesis conditions are discovered. Halogen bonding has been shown to be a useful and reliable crystal engineering tool with the formation of energetic cocrystals; a variety of halogen-containing energetics are already known and should offer additional scaffolds for the formation of cocrystalline materials.

3.4 Experimental Procedures

3.4.1 Materials

Acetonitrile (Certified ACS) was obtained from Fisher Scientific and dried over 4 Å molecular sieves. 1,3,5-Trinitrobenzene (TNB) was received from Pfaltz & Bauer (wetted with ~40% water) and allowed to dry before use. 1,3,5-Triiodo-2,4,6-trinitrobenzene (TITNB), 1,3,5-tribromo-2,4,6-trinitrobenzene (TBTNB) and 1,3,5-tricloro-2,4,6-trinitrobenzene (TCTNB) were synthesized as described in the literature.[21] ***Caution!*** *Although no unplanned detonations were encountered during this work, TNB, TITNB, TBTNB, and TCTNB are all dangerous high explosives. Proper safety practices and equipment were used to prevent an explosion due to friction, heat, static shock, or impact. Be aware that the potential for severe injury exists if these materials are handled improperly.*

3.4.2 Crystallization

Both cocrystals of TNB (**1** and **2**) were initially obtained from acetonitrile solutions, with the stoichiometric ratio of the pure components 2:1, by slow evaporation and then conditions for growth in pure form was determined. The cocrystal synthesis could be scaled up conveniently with the use of solvent mediated transformation in a slurry of the pure components at room temperature, see below.

*2:1 TNB/TITNB (**1**)*

A 4 mL glass vial was loaded with 21.31 mg of TNB (0.1000 mmol), 29.54 mg TITNB (0.05000 mmol) and 200 µL of dry isopropanol. The vial was sealed and shaken gently for 6 days, during which time the pure components of TNB and TITNB had disappeared and small clear prisms had appeared. This solid was determined to be the 2:1 TNB/TITNB cocrystal by both Raman spectroscopy and powder X-ray diffraction.

*2:1 TNB/TBTNB (**2**)*

A 4 mL glass vial was loaded with 21.31 mg of TNB (0.1000 mmol), 22.48 mg TBTNB (0.05000 mmol), 150.0 µL of dry isopropanol and a small magnetic stir bar. The vial was sealed and stirred gently for 4 days, during which time the pure components of TNB and TBTNB had disappeared and a white powder had appeared. This solid was determined to be the 2:1 TNB/TBTNB cocrystal by both Raman spectroscopy and powder X-ray diffraction.

3.4.3 Raman Spectroscopy

Raman spectra were collected using a Renishaw inVia Raman Microscope equipped with a Leica microscope, 633 nm laser, 1800 lines/mm grating, 50 µm slit and a RenCam CCD detector. Spectra were collected in extended scan mode with a range of 100-4000 cm^{-1} and then analyzed using the WiRE 3.4 software package (Renishaw). Calibration was performed using a silicon standard in static mode.

3.4.4 Powder X-ray Diffraction (PXRD)

Powder X-ray diffraction patterns were collected on a Bruker D8 Advance diffractometer using Cu-Kα radiation (λ = 1.54187 Å) and operating at 40 kV and 40 mA. Samples were prepared by finely grinding and packing into the depression of a glass slide. The powder patterns were collected by scanning 2θ from 4° to 70° with a step size of 0.02° and a step speed of 0.5

seconds. To minimize preferred orientation effects, the PXRD patterns of the cocrystals were also obtained on a Rigaku R-Axis Spider diffractometer using Cu-Kα radiation (λ = 1.54187 Å) and operating at 40 kV and 44 mA. Samples were ground and mounted on a CryoLoop™. Images were collected for 10 minutes with rotating the sample about φ-axis at 10°/sec, oscillating ω between 80° and 140° at 1°/sec with χ fixed at 45°. The images were integrated from 4 to 50° with a 0.02° step size using AreaMax 2.0 software (Rigaku). The data were processed using Jade 8 XRD Pattern Processing, Identification & Quantification analysis software (Materials Data, Inc.).[51] The powder patterns were all compared to their respective simulated powder patterns from the single crystal X-ray diffraction structures and were found to be in good agreement with the predicted patterns.

3.4.5 Single Crystal Structure Determination

Single crystal X-ray diffraction data for cocrystals **1** and **2** were collected using a Rigaku AFC10K Saturn 944+ CCD-based X-ray diffractometer equipped with a low temperature device and Micromax-007HF Cu-target micro-focus rotating anode (λ = 1.54187 Å) operated at 1.2 kW power (40 kV, 30 mA). The X-ray intensities were measured at 85(1) K with the detector placed at a distance 42.00 mm from the crystal. The data were processed with CrystalClear 2.0 (Rigaku)[52] and corrected for absorption. The structures were solved and refined with the Bruker SHELXTL (version 2008/4)[53] software package using direct methods. All non-hydrogen atoms were refined anisotropically with the hydrogen atoms placed in a combination of refined and idealized positions.

3.4.6 Differential Scanning Calorimetry (DSC)

Thermograms for each sample were recorded on a TA Instruments Q20 DSC equipped with a RCS90 chiller. All experiments were conducted in Tzero™ hermetic aluminum DSC pans under

a nitrogen purge with a heating rate of 10 °C/min, while covering the temperature range of 35 °C to 400 °C. The instrument was calibrated using an indium standard. Thermograms were analyzed using TA Universal Analysis 2000, V 4.5A.

3.4.7 Computational Optimization of Molecules and Unit Cells

The atomic positions and unit cells of each crystal were optimized starting from either the experimental structure or an isostructural analogue using CP2K v. 2.6.2.[31] The QUICKSTEP package[30] was used with the Gaussian and plane wave (GPW) scheme[29] to run *ab initio* Density Functional Theory (DFT) calculations. The PBE exchange-correlation functional[32] was used with the D3(BJ) dispersion correction,[33, 34] including the C9 term and a cutoff of 18 Å. The DZVP-MOLOPT-GTH (m-DZVP) or DZVP-MOLOPT-SR-GTH basis sets[35] were used for {H, C, N, O, Cl} and {Br, I}, respectively, paired with appropriate dual-space GTH pseudopotentials[36] optimized for the PBE functional.[37] The calculations made use of the orbital transformation method[54] for wave function optimization and the BFGS algorithm for geometry optimization.

Explicit supercells were constructed for each system such that each cell vector spans at least two independent molecules, but crystallographic symmetry was not imposed during the optimizations. For all systems, SCF convergence was set to 1E-7 Hartree using the fine integration grid and the following QUICKSTEP variables: 5 grids with a cutoff of 900 Ry and a relative cutoff of 70 Ry, EPS_RHO = 1E-12, EPS_PGF_ORB = 1E-7. The optimization parameters were selected based on convergence of the energy per unit cell to < 1E-5 Hartree, although due to computational cost of the large supercells, the dispersion cutoff of 18 Å is converged only to 1E-4 Hartree. The dispersion cutoff was smaller than the length of any supercell vector.

Optimizations of single molecules of TITNB, TBTNB, and TCTNB were performed by placing each molecule in a 20 $Å^3$ cell. The electrostatic potential was calculated on a grid using CP2K and visualized at the $\rho = 0.002$ a.u. isosurface using VMD v. 1.9.1. The optimized cell parameters for the TNB, TXTNB, and cocrystal systems are reported in Tables S1 – S3. After optimizations, deviations from experimental cell vectors and unit cell volumes are ≤ 4.4% and ≤ 4.7%, respectively. The total system energy for each crystal is reported in Table S4. The relative lattice energies of -11.5, -8.2, and -8.5 kJ/mol for 2:1 TNB/TITNB, TNB/TBTNB and TNB/TCTNB, respectively, are determined by subtracting the cocrystal system energy per asymmetric unit from the total lattice energy of the coformers in an equivalent ratio. Conformational changes from the gas phase single molecule geometries are minimal and all coformers are in the same solvent environment; therefore, the thermodynamic cycle reduces to the difference between the cocrystal lattice energy and the lattice energies of (2*TNB Form I + TXTNB).

3.5 References

1. Fleischman, S. G.; Kuduva, S. S.; McMahon, J. A.; Moulton, B.; Bailey Walsh, R. D.; Rodríguez-Hornedo, N.; Zaworotko, M. J., Crystal Engineering of the Composition of Pharmaceutical Phases: Multiple-Component Crystalline Solids Involving Carbamazepine. *Cryst. Growth Des.* **2003,** *3*, 909-919.

2. Porter III, W. W.; Elie, S. C.; Matzger, A. J., Polymorphism in Carbamazepine Cocrystals. *Cryst. Growth Des.* **2008,** *8*, 14-16.

3. Sanphui, P.; Goud, N. R.; Khandavilli, U. B. R.; Nangia, A., Fast Dissolving Curcumin Cocrystals. *Cryst. Growth Des.* **2011,** *11*, 4135-4145.

4. Schultheiss, N.; Newman, A., Pharmaceutical Cocrystals and Their Physicochemical Properties. *Cryst. Growth Des.* **2009,** *9*, 2950-2967.

5. Kapadia, P. P.; Ditzler, L. R.; Baltrusaitis, J.; Swenson, D. C.; Tivanski, A. V.; Pigge, F. C., Semiconducting Organic Assemblies Prepared from Tetraphenylethylene Tetracarboxylic Acid and Bis(pyridine)s via Charge-Assisted Hydrogen Bonding. *J. Am. Chem. Soc.* **2011,** *133*, 8490-8493.

6. Sato, S.; Nikawa, H.; Seki, S.; Wang, L.; Luo, G.; Lu, J.; Haranaka, M.; Tsuchiya, T.; Nagase, S.; Akasaka, T., A Co-Crystal Composed of the Paramagnetic Endohedral Metallofullerene La@C82 and a Nickel Porphyrin with High Electron Mobility. *Angew. Chem. Int. Ed.* **2012,** *51*, 1589-1591.

7. Sokolov, A. N.; Friščić, T.; MacGillivray, L. R., Enforced Face-to-Face Stacking of Organic Semiconductor Building Blocks within Hydrogen-Bonded Molecular Cocrystals. *J. Am. Chem. Soc.* **2006,** *128*, 2806-2807.

8. Koshima, H.; Miyamoto, H.; Yagi, I.; Uosaki, K., Preparation of Cocrystals of 2-Amino-3-nitropyridine with Benzenesulfonic Acids for Second-Order Nonlinear Optical Materials. *Cryst. Growth Des.* **2004,** *4*, 807-811.

9. Sun, A.; Lauher, J. W.; Goroff, N. S., Preparation of Poly(diiododiacetylene), an Ordered Conjugated Polymer of Carbon and Iodine. *Science* **2006,** *312*, 1030-1034.

10. Yan, D.; Delori, A.; Lloyd, G. O.; Friščić, T.; Day, G. M.; Jones, W.; Lu, J.; Wei, M.; Evans, D. G.; Duan, X., A Cocrystal Strategy to Tune the Luminescent Properties of Stilbene-Type Organic Solid-State Materials. *Angew. Chem. Int. Ed.* **2011,** *50*, 12483-12486.

11. Landenberger, K. B.; Matzger, A. J., Cocrystal Engineering of a Prototype Energetic Material: Supramolecular Chemistry of 2,4,6-Trinitrotoluene. *Cryst. Growth Des.* **2010,** *10*, 5341-5347.

12. Landenberger, K. B.; Matzger, A. J., Cocrystals of 1,3,5,7-Tetranitro-1,3,5,7-tetrazacyclooctane (HMX). *Cryst. Growth Des.* **2012,** *12*, 3603-3609.

13. Millar, D. I. A.; Maynard-Casely, H. E.; Allan, D. R.; Cumming, A. S.; Lennie, A. R.; Mackay, A. J.; Oswald, I. D. H.; Tang, C. C.; Pulham, C. R., Crystal engineering of energetic materials: Co-crystals of CL-20. *CrystEngComm* **2012,** *14*, 3742-3749.

14. Bolton, O.; Matzger, A. J., Improved Stability and Smart-Material Functionality Realized in an Energetic Cocrystal. *Angew. Chem. Int. Ed.* **2011,** *50*, 8960-8963.

15. Bolton, O.; Simke, L. R.; Pagoria, P. F.; Matzger, A. J., High Power Explosive with Good Sensitivity: A 2:1 Cocrystal of CL-20:HMX. *Cryst. Growth Des.* **2012,** *12*, 4311-4314.

16. Zhang, H.; Guo, C.; Wang, X.; Xu, J.; He, X.; Liu, Y.; Liu, X.; Huang, H.; Sun, J., Five Energetic Cocrystals of BTF by Intermolecular Hydrogen Bond and π-Stacking Interactions. *Cryst. Growth Des.* **2012,** *13*, 679-687.

17. Landenberger, K. B.; Bolton, O.; Matzger, A. J., Two Isostructural Explosive Cocrystals with Significantly Different Thermodynamic Stabilities. *Angew. Chem. Int. Ed.* **2013,** *52*, 6468-6471.

18. Wang, Y.; Yang, Z.; Li, H.; Zhou, X.; Zhang, Q.; Wang, J.; Liu, Y., A Novel Cocrystal Explosive of HNIW with Good Comprehensive Properties. *Propell. Explos. Pyrotech.* **2014,** *39*, 590-596.

19. Yang, Z.; Li, H.; Zhou, X.; Zhang, C.; Huang, H.; Li, J.; Nie, F., Characterization and Properties of a Novel Energetic–Energetic Cocrystal Explosive Composed of HNIW and BTF. *Cryst. Growth Des.* **2012,** *12*, 5155-5158.

20. Yang, Z.; Wang, Y.; Zhou, J.; Li, H.; Huang, H.; Nie, F., Preparation and Performance of a BTF/DNB Cocrystal Explosive. *Propell. Explos. Pyrotech.* **2014,** *39*, 9-13.

21. Landenberger, K. B.; Bolton, O.; Matzger, A. J., Energetic-Energetic Cocrystals of Diacetone Diperoxide (DADP): Dramatic and Divergent Sensitivity Modifications via Cocrystallization. *J. Am. Chem. Soc.* **2015,** *137*, 5074-5079.

22. Bennion, J. C.; McBain, A.; Son, S. F.; Matzger, A. J., Design and Synthesis of a Series of Nitrogen-Rich Energetic Cocrystals of 5,5′-Dinitro-2H,2H′-3,3′-bi-1,2,4-triazole (DNBT). *Cryst. Growth Des.* **2015,** *15*, 2545-2549.

23. Politzer, P.; Murray, J. S.; Clark, T., Halogen bonding and other [sigma]-hole interactions: a perspective. *Phys. Chem. Chem. Phys.* **2013,** *15*, 11178-11189.

24. Chapman, R. D.; Hollins, R. A., Octafluoropentaerythrityltetramine (Octafluoro-PETA) and Process For Its Preparation. *U.S. 8,008,527B1* **2011**.

25. Goud, N. R.; Bolton, O.; Burgess, E. C.; Matzger, A. J., Unprecedented Size of the σ-Holes on 1,3,5-Triiodo-2,4,6-trinitrobenzene Begets Unprecedented Intermolecular Interactions. *Cryst. Growth Des.* **2016,** *16*, 1765-1771.

26. Meyer, R.; Köhler, J.; Homburg, A., In *Explosives*, Wiley-VCH Verlag GmbH & Co. KGaA2003; pp 307-360.

27. *Distances are calculated in Mercury 3.7 from the CIFs at 85 K with the C-H hydrogens normalized at 1.089 Å.*

28. *Intermolecular contacts between C-X (X = Br or I) and C-NO_2 (N-O bond order set to any) were determined via a search of the CSD in ConQuest V 1.18, with Nov. 2015 updates and the following filters applied: not disordered, no ions and R factor ≤ 10%. The results in ConQuest resulted in the n value and the distances were analyzed in Mercury 3.7.*

29. Lippert, G.; Hutter, J.; Parrinello, M., A hybrid Gaussian and plane wave density functional scheme. *Mol. Phys.* **1997,** *92*, 477-488.

30. VandeVondele, J.; Krack, M.; Mohamed, F.; Parrinello, M.; Chassaing, T.; Hutter, J., QUICKSTEP: Fast and accurate density functional calculations using a mixed Gaussian and plane waves approach. *Comput. Phys. Commun.* **2005,** *167*, 103-128.

31. Hutter, J.; Iannuzzi, M.; Schiffmann, F.; VandeVondele, J., CP2K: Atomistic simulations of condensed matter systems. *WIREs Comput. Mol. Sci.* **2014,** *4*, 15-25.

32. Perdew, J. P.; Burke, K.; Ernzerhof, M., Generalized gradient approximation made simple. *Phys. Rev. Lett.* **1996,** *77*, 3865-3868.

33. Grimme, S.; Antony, J.; Ehrlich, S.; Krieg, H., A consistent and accurate *ab initio* parametrization of density functional dispersion correction (DFT-D) for the 94 elements H-Pu. *J. Chem. Phys.* **2010,** *132*, 154104.

34. Grimme, S.; Ehrlich, S.; Goerigk, L., Effect of the damping function in dispersion corrected density functional theory. *J. Comput. Chem.* **2011,** *32*, 1456-65.

35. VandeVondele, J.; Hutter, J., Gaussian basis sets for accurate calculations on molecular systems in gas and condensed phases. *J. Chem. Phys.* **2007,** *127*, 114105.

36. Goedecker, S.; Teter, M.; Hutter, J., Separable dual-space Gaussian pseudopotentials. *Phys. Rev. B: Condens. Matter* **1996,** *54*, 1703-1710.

37. Krack, M., Pseudopotentials for H to Kr optimized for gradient-corrected exchange-correlation functionals. *Theor. Chem. Acc.* **2005,** *114*, 145-152.

38. Thallapally, P. K.; Jetti, R. K. R.; Katz, A. K.; Carrell, H. L.; Singh, K.; Lahiri, K.; Kotha, S.; Boese, R.; Desiraju, G. R., Polymorphism of 1,3,5-Trinitrobenzene Induced by a Trisindane Additive. *Angew. Chem. Int. Ed.* **2004,** *43*, 1149-1155.

39. *Molecular volumes are calculated in Spartan14 V1.1.2 by determining the equilibrium geometry at the ground state for structures of the pure components with the semi-empirical AM1 method.*

40. Deschamps, J. R.; Parrish, D. A., Stabilization of Nitro-Aromatics. *Propell. Explos. Pyrotech.* **2015,** *40*, 506-513.

41. He, C.; Parrish, D. A.; Shreeve, J. n. M., Alkyl Ammonium Cation Stabilized Biocidal Polyiodides with Adaptable High Density and Low Pressure. *Chem. Eur. J.* **2014,** *20*, 6699-6706.

42. He, C.; Zhang, J.; Shreeve, J. n. M., Dense Iodine-Rich Compounds with Low Detonation Pressures as Biocidal Agents. *Chem. Eur. J.* **2013,** *19*, 7503-7509.

43. Sullivan, K. T.; Piekiel, N. W.; Chowdhury, S.; Wu, C.; Zachariah, M. R.; Johnson, C. E., Ignition and Combustion Characteristics of Nanoscale Al/AgIO3: A Potential Energetic Biocidal System. *Combust. Sci. Technol.* **2010,** *183*, 285-302.

44. Wang, H.; Jian, G.; Zhou, W.; DeLisio, J. B.; Lee, V. T.; Zachariah, M. R., Metal Iodate-Based Energetic Composites and Their Combustion and Biocidal Performance. *ACS Appl. Mat. Interfaces* **2015,** *7*, 17363-17370.

45. Chapman, R. D., Process for employing HNFX as a biocidal explosive. *U.S. 8,221,566B1* **2012**.

46. Klapötke, T. M., *Chemistry of High-Energy Materials*. 2 ed.; Walter de Gruyter: Berlin/Boston, 2012.

47. Fischer, D.; Klapötke, Thomas M.; Stierstorfer, J., Synthesis and Characterization of Guanidinium Difluoroiodate, [C(NH2)3]+[IF2O2]– and its Evaluation as an Ingredient in Agent Defeat Weapons‡. *Z. Anorg. Allg. Chem.* **2011,** *637*, 660-665.

48. Haggstrom, J. A.; Klabunde, K. J.; Marchin, G. L., Biocidal properties of metal oxidenanoparticles and their halogenadducts. *Nanoscale* **2010,** *2*, 399-405.

49. Koper, B. O.; Klabunde, S. J.; Marchin, L. G.; Klabunde, J. K.; Stoimenov, P.; Bohra, L., Nanoscale Powders and Formulations with Biocidal Activity Toward Spores and Vegetative Cells of Bacillus Species, Viruses, and Toxins. *Curr. Microbiol. 44*, 49-55.

50. Stoimenov, P. K.; Klinger, R. L.; Marchin, G. L.; Klabunde, K. J., Metal Oxide Nanoparticles as Bactericidal Agents. *Langmuir* **2002,** *18*, 6679-6686.

51. Jade Plus 8.2 ed.: Materials Data, Inc., 1995-2007.

52. CrystalClear Expert 2.0 r12, Rigaku Americas and Rigaku Corporation (2011): Rigaku Americas, 9009, TX, USA 77381-5209, Rigaku Tokyo, 196-8666, Japan.

53. Sheldrick, G.M. SHELXTL, v. 2008/4; Bruker Analytical X-ray: Madison, WI, 2008.

54. VandeVondele, J.; Hutter, J. r., An efficient orbital transformation method for electronic structure calculations. *J. Chem. Phys.* **2003,** *118*, 4365.

Chapter 4: Hydrogen Peroxide Solvates of 2,4,6,8,10,12-Hexanitro-2,4,6,8,10,12-Hexaazaisowurtzitane

Published: Bennion, J.C.; Chowdhury, N.; Kampf,J.W.; Matzger, A. J., *Angew. Chem. Int. Ed.*, **2016**, *55*, 13118-13121.

4.1 Introduction

The formation of hydrated materials is a common phenomenon throughout crystal engineering; in the field of pharmaceuticals it is estimated that at least a third of all pharmaceuticals are capable of forming hydrates.[1] In energetic materials the formation of various (hemi-, mono-, di-, etc.) hydrated materials is a problem that is also often encountered.[2-7] For example, the widely used energetics octahydro-1,3,5,7-tetranitro-1,3,5,7-tetrazocine (HMX) and 2,4,6,8,10,12-hexanitro-2,4,6,8,10,12-hexaazaisowurtzitane (CL-20) both form ¼ hydrates, γ-HMX and α-CL-20, which have inferior detonation properties compared to the respective high density forms, β-HMX and ε-CL-20. The detonation properties (velocity and pressure) are dependent on the density of a material (higher density translates to higher detonation velocity/pressure). While a hydrate may have a high density, hydration ultimately reduces the effective density of the energetic component(s) and as a result diminishes the performance of the material. Such an erosion of properties is similar to the case of cocrystals of energetic materials with non-energetic coformers.[8-10] This has been overcome through the use of other energetic molecules as coformers. Here we adapt this concept by using hydrogen peroxide as an energetic replacement for water of hydration in CL-20 thus improving the oxygen balance of the material.

Oxygen balance (OB) is the weight percent of oxygen released as a result of the complete conversion to neutral molecular components (CO_2, H_2O, N_2, etc.) upon detonation.[11] A positive

OB denotes that there is excess oxygen in the system after full conversion, whereas a negative OB refers to an insufficient amount of oxygen and typically results in the generation of carbon soot and lower oxidized, toxic gases (CO, NO). The more negative the OB, the less gas that is generated from the detonation and as a result, the brisance or shattering effect of the material is diminished.[12, 13] The vast majority of traditional energetic materials possess a negative OB with respect to CO_2: CL-20 (-11%), HMX (-22%) and 2,4,6-trinitrotoluene [TNT] (-74%). The inclusion of water molecules into the lattice of an energetic does not lead to increased OB because the oxygen atoms are already bonded to two hydrogens. However, the ability to incorporate water into the lattice suggested to us that a chemically similar, but more oxidizing solvent could improve rather than degrade performance. Hydrogen peroxide (HP) has seen extensive use as a propellant in both mono- and bi-propellant rockets.[14-16] HP has very low toxicity, minimal environmental impact compared to traditional perchlorate oxidizers and is also impact/shock insensitive in concentrated form.

In addition to the use of HP in rocket fuels, the peroxy group has seen some application into various energetic materials, such as triacetone triperoxide (TATP), diacetone diperoxide (DADP), hexamethylene triperoxide diamine (HMTD) and more recently into energetic materials containing peroxy acid and hydroperoxy groups.[17-20] The problem often encountered with these materials is that many are very sensitive to both thermal and impact initiation, while also possessing very poor OB due to the large amount of carbon contained within the backbones. Recently, DADP was shown to form a series of 1:1 cocrystals with 1,3,5-trichloro-2,4,6-trinitrobenzene (TCTNB), 1,3,5-tribromo-2,4,6-trinitrobenzene (TBTNB) and 1,3,5-triiodo-2,4,6-trinitrobenzene (TITNB) through interaction between the TXTNB (X = Cl, Br or I) coformer and the peroxy moiety.[21, 22] These materials show feasibility for the formation of non-

covalent interactions with the peroxy moiety. The substitution of HP for water of hydration might be predicted to form not only non-covalent interactions between the peroxy moieties, but also allow maintenance of the hydrogen bonding pattern.

The hydrated form of CL-20, α-CL-20, is generally regarded as a ¼ hydrate, but can also exist as a ½ hydrate.[5] The unit cell of the ¼ hydrate contains a total of eight CL-20 molecules with sufficient void space to encompass two solvent molecules. The packing coefficient (C_k), a measure of the efficiency that molecules occupy the unit cell volume, can be determined by dividing the total molecular volume in a unit cell by the unit cell volume. By comparing the C_k of the high density ε-CL-20 (80.6%) to the lower density α-CL-20 (77.9%), it is evident that α-CL-20 possess void space that might be used to contain additional solvent molecules. Recently, it has been shown that water can be removed under heating/vacuum from α-CL-20 with little deformation of the lattice parameters.[23] This suggests the ability to utilize the void space for the formation of CL-20 solvates that will remain isostructural to the hydrated α-CL-20.

4.2 Results and Discussion

Disclosed here are two novel polymorphic solvates of CL-20 with HP, orthorhombic (**1**) and monoclinic (**2**); both materials form in a 2:1 molar ratio of CL-20 and HP (see Figure 4.1 for pure component structures). These represent the first examples of solvates with HP for any energetic material and may be influential for the further development of novel energetics.

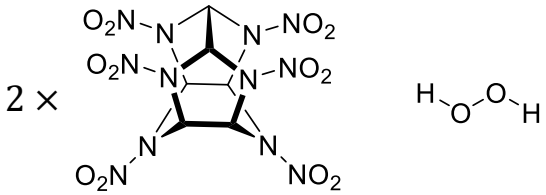

Figure 4.1 Chemical structures of the pure components for the CL-20 polymorphic solvates (**1** and **2**): CL-20 and HP.

The concomitant formation of **1** and **2** was initially observed from a 1:1 acetonitrile/HP (>90% H_2O_2) solution. Solvate **1** exhibits a rhombic habit, whereas **2** typically exhibits a polyhedron habit (Figure 4.3c and 4.4c respectively), and these crystals were separated and analyzed by powder X-ray diffraction. The powder pattern of **1** was indistinguishable from α-CL-20 (Appendix C **C1.1** and **C1.2**), which suggests that the material is either simply α-CL-20 or an isostructural material with HP replacing the water molecules as hypothesized. Solvate **2**, on the other hand, is readily distinguishable from any of the other forms of CL-20 (Appendix C **C1.3**).

The crystal structures of **1** and **2** were elucidated and determined to be 2:1 CL-20/HP solvates; crystallographic data are presented below in Table 4.1 for α-CL-20, **1** and **2**. Both materials have high crystallographic densities: **1** has a density of 2.033 g/cm^3 at 295 K and **2** has a density of 1.966 g/cm^3 at 295 K. When compared to α-CL-20 (1.970 g/cm^3 at 295 K), the isostructural material **1** possesses a superior density and **2** possesses a density similar to that of the hydrated material. The OB for both **1** and **2** was determined to be -8.79%, an improvement with respect to both α-CL-20 (-10.84%) and pure CL-20 (-10.95%).

One way of identifying the solvent content in a crystal structure is through the use of a PLATON/SQUEEZE calculation, which assesses the electron density contribution in the unit cell from the solvent.[24] Both the HP solvent present in the crystal structure of **1** and the H_2O in α-CL-20 (for these calculations the crystal structure of α-CL-20 was redetermined) sit on the same inversion center, leading to uncertainty into the existence of the HP in the material. The electron density was estimated to be 24 and 44 e^-/unit cell for α-CL-20 and **1**, respectively. The electron density for α-CL-20 corresponds roughly to the two water molecules present in the unit cell (10 e^-/molecule), whereas the higher electron density of 44 electrons for **1** corresponds to the presence of HP (18 e^-/molecule) in the isostructural material. The same routine was applied to **2**

and the electron density was determined to be 79 e^-/unit cell, which corresponds closely to the four HP molecules in the 2:1 CL-20 solvate. The higher electron density suggests the presence of a novel material compared to α-CL-20, but given the tendency of SQUEEZE to overcount electron density, additional investigation via Raman spectroscopy and chemical analysis was carried out to further support these results.

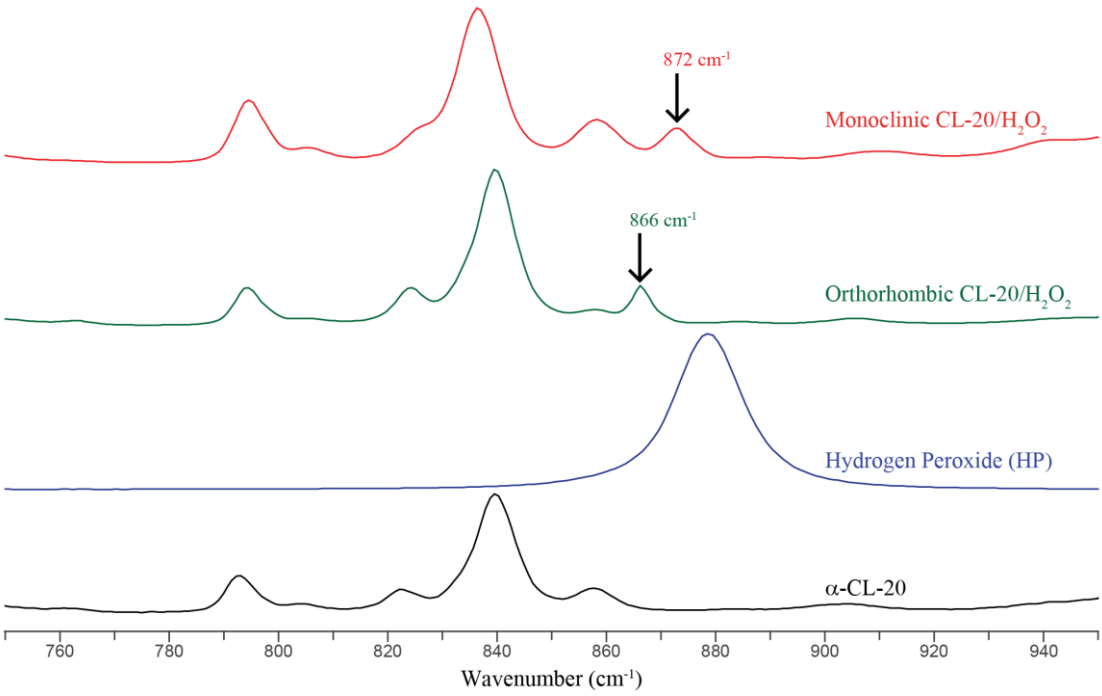

Figure 4.2 Raman spectra (700-1000 cm^{-1}) of α-CL-20, concentrated HP, **1** and **2**. Pure HP O-O peak is at 879 cm^{-1}.

The Raman spectra of both **1** and **2** were compared to all known forms of CL-20 and in particular to α-CL-20 (Figure 4.2 and Appendix C **C1.4**). Both **1** and **2** resemble α-CL-20, with the exception of the addition/shifting of the O-O stretch present in the two new solvates. Pure HP has an O-O stretch at around 879 cm^{-1}, while the solvates have an O-O peak shifted to 866 and 872 cm^{-1} respectively for **1** and **2** (Figure 4.2). Additionally, shifting is present in the H-O stretch region for all three materials: α-CL-20 (3610 cm^{-1}), **1** (3557 cm^{-1}) and **2** (3517 cm^{-1}). The addition of the O-O peak and the shifting of the H-O peak in both **1** and **2** is indicative of an

interaction between the CL-20 and HP. For both of the solvates, the higher population of electron density, along with the new and shifted peaks in the Raman spectra, confirms the existence of HP in these novel materials. The presence of the HP in the solvates was also quantified by a chemical test wherein the oxidation of triphenylphosphine with HP to triphenylphosphine oxide was measured by ^{31}P NMR and the proposed stoichiometry of 2 CL-20 to 1 HP was confirmed.

The formation of both CL-20 solvates rely on hydrogen bonding between the HP and the nitro groups of CL-20 as well as C-H hydrogen bonds between adjacent CL-20 molecules. The shortest interactions between the HP and CL-20 are highlighted (see Figures 4.3 and 4.4 respectively for solvates **1** and **2**). The HP in **1** hydrogen bonds with two CL-20 molecules and interacts with two nitro groups on each molecule in a bifurcated fashion, with intermolecular distances of 2.17/2.22 Å and 2.19/2.24 Å for each CL-20 molecule (Figure 4.3a). In contrast, the HP in solvate **2** hydrogen bonds with two CL-20 molecules, with an equivalent intermolecular distance of 2.25 Å. In both structures, the CL-20 molecules form linear chains through C-H and nitro hydrogen bonding with adjacent CL-20 molecules; these interactions are reminiscent to those seen in both 1:1 CL-20/TNT and 2:1 CL-20/HMX.[25, 26] The shortest CL-20 C-H$\cdots$$NO_2$ interactions for **1** and **2** are 2.20 Å and 2.23/2.31 Å respectively. The same linear chain of CL-20 molecules in **1** is also seen in α-CL-20 (2.28 Å). Additionally in the structure of **2**, the repeat unit of two CL-20s with one HP (Figure 4.4a) forms a tape that extends through C-H hydrogen bonding between adjacent CL-20 molecules at 2.23 Å.

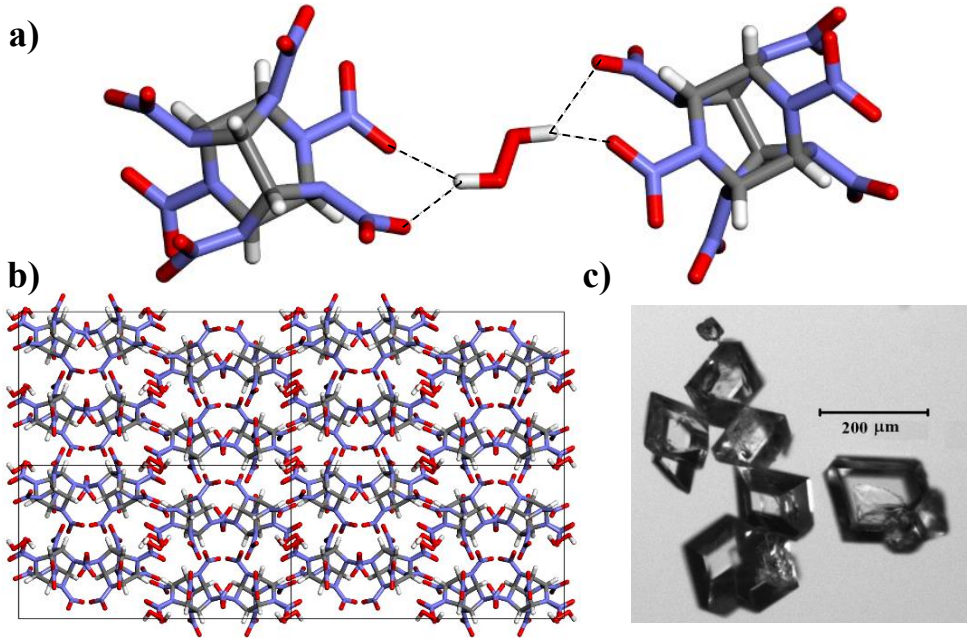

Figure 4.3 The 2:1 CL-20/HP orthorhombic solvate (**1**). a) Hydrogen bonding interaction between CL-20 and HP. b) Unit cell viewing down the *a*-axis. c) Typical rhombic habit morphology of the orthorhombic polymorph.

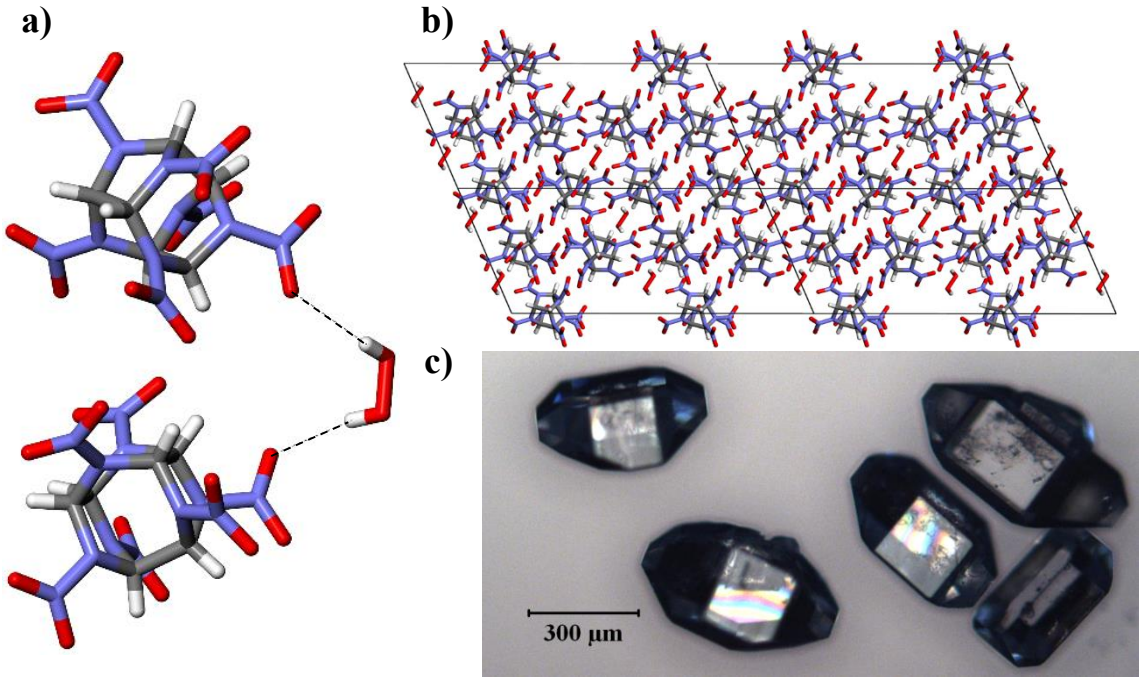

Figure 4.4 The 2:1 CL-20/HP monoclinic solvate (**2**). a) Hydrogen bonding interaction between CL-20 and HP. b) Unit cell viewing down the *a*-axis. c) Typical polyhedron habit morphology of the monoclinic polymorph.

With the structural parameters obtained, the C_k values for these systems were determined for **1**, **2**, and the pure components ε-CL-20 and α-CL-20.[27] Both solvates **1** (80.6%) and **2** (78.1%) possess C_k's higher than that of the α-CL-20 (77.9%), whereas **1** equals the C_k of ε-CL-20 (80.6%). The difference of the C_k between **1** and α-CL-20 is expected for two reasons: the increased ratio of CL-20/HP (2:1) compared to the CL-20/H_2O (4:1) and the increased size/volume of the HP compared to the H_2O molecules. The C_k of solvate **1** equals that of ε-CL-20 through the incorporation of additional oxidizer, while also possessing a density on par to that of ε-CL-20 (2.04 g/cm^3).

The thermal properties of both **1** and **2** were determined via differential scanning calorimetry (DSC) and thermogravimetric analysis (TGA). The DSC traces show endothermic peaks at 165, 190 and 158 °C for **1**, **2** and α-CL-20 respectively, and decomposition around 250 °C for all three materials (Appendix C **C1.9**). Raman spectroscopy and PXRD were performed after holding the temperature just past the respective endothermic peaks of **1** and **2**, and this thermal event was determined to correspond to the release of HP and subsequent conversion to γ-CL-20. The difference in the desolvation temperature of the two materials arises from the difference in both the hydrogen bonding between the two components and the packing arrangements of the CL-20 molecules in the unit cell; **1** possesses a channel for the HP to escape from, while the HP in **2** is contained in a cage of CL-20 molecules. The conversion of the solvates to γ-CL-20 explains why all three materials decompose at the same temperature. Furthermore, the TGA thermograms show the loss of HP at the corresponding endothermic peak temperatures (Appendix C **C1.10** and **C1.11**). The thermal stability of these materials is an important performance criterion to consider in their future application as energetics.

The sensitivity of an energetic material to various external stimuli (impact, friction, electrostatic shock, etc.) must be determined before utility of a material can be fully realized. The sensitivity of **1** and **2** was determined via small-scale impact drop testing; for reference the Dh50 of ε-CL-20 and β-HMX are 29 and 55 cm, respectively.[26, 28] Solvate formation of CL-20 with HP results in material **1** possessing sensitivity (24 cm) just below that of ε-CL-20 (29 cm). Solvate **2** possesses sensitivity (28 cm) similar to that of ε-CL-20, yet with an increase to the overall OB of the system. These materials can be classified as sensitive secondary explosives. Currently CL-20 has seen some application in propellants, but with the need of oxidizers in the final formulation. Both **1** and **2** represent materials that, through solvate formation, are able to reduce/eliminate the need for the use of toxic oxidizers like perchlorates in the formulation of CL-20 propellants and should increase its potential utility.

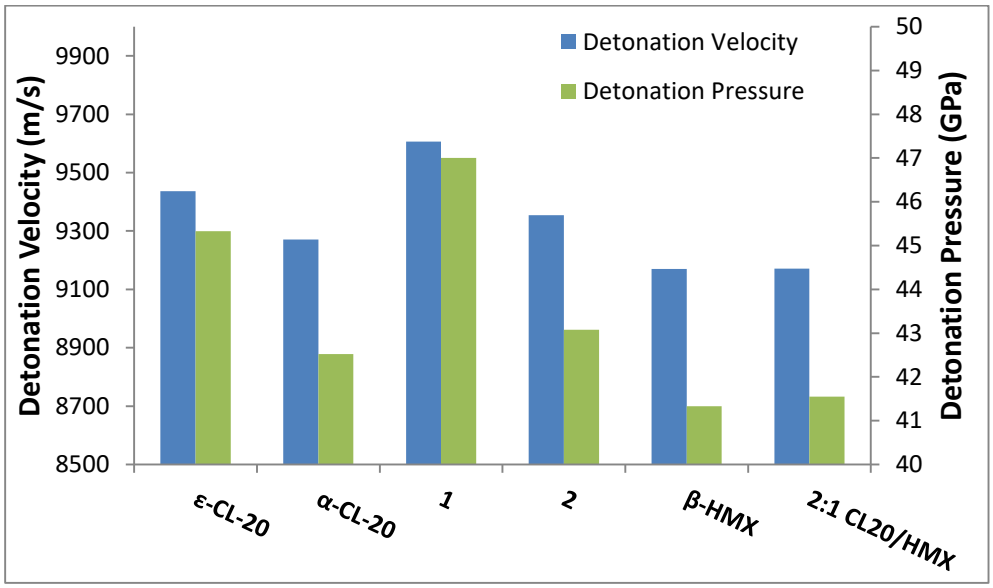

Figure 4.5 Detonation parameters (velocity and pressure) of ε-CL-20, α-CL-20, **1**, **2**, β-HMX and 2:1 CL-20/HMX are predicted with Cheetah 7.0 using the room-temperature (295 K) crystallographic densities of each material; detonation parameters for **1** at 2.033 g/cm^3 were calculated by extrapolating the detonation velocity vs. density and detonation pressure vs. density squared from the values determined at 99-90% of the crystallographic density given that the theoretical max density (%TMD) maxed out at only 2.013 g/cm^3.

The detonation properties (velocity, pressure, etc.) were calculated using the thermochemical code Cheetah 7.0.[29] Cheetah calculations require both the chemical (molecular formula/density) and the thermodynamic (heat of formation) properties of a novel energetic material or formulation to predict the detonation velocity/pressure. The cocrystal/solvate performance properties are predicted by treating the materials as a formulation of the two components in their respective molar ratio. For the CL-20 solvates, the room temperature (295 K) densities for each material were used to predict both the detonation velocities and pressures as well as those properties for ε-CL-20, α-CL-20, β-HMX and the 2:1 CL-20/HMX cocrystal (Figure 4.5). Both **1** (9606 m/s and 47.005 GPa) and **2** (9354 m/s and 43.078 GPa) have predicted detonation velocities and pressures that outperform α-CL-20, β-HMX and the 2:1 CL-20/HMX cocrystal. The orthorhombic solvate **1** is also projected to surpass the properties of ε-CL-20 (9436 m/s and 45.327 GPa), the gold standard for high performance energetic materials; this feat is accomplished through the incorporation of HP to increase the overall OB, with little degradation to the sensitivity of the materials.

4.3 Conclusion

In conclusion, we have discovered and characterized two polymorphic energetic solvates comprised of 2:1 molar ratios of the high explosive CL-20 and the oxidizer HP. The hydrated form of CL-20, α-CL-20, was used as a guide for the synthesis of the two HP solvates, and indeed one solvate remains isostructural to α-CL-20. These solvates represent the first example of hydrogen bonding interactions between HP and the nitro moiety, and the approach will be useful for the formation of additional HP solvated materials. Calculated detonation parameters (velocity and pressure) of the two solvates are predicted to surpass the performance of all known forms of HMX and all low density forms of CL-20, with the orthorhombic solvate **1** expected to

exceed the properties of even ε-CL-20. The incorporation of HP into the crystal system allows for an easy and effective method for the improvement of the detonation properties, without the need for the development of new molecules. By utilizing existing hydrated energetic materials as a guide, the formation of additional isostructural HP solvates may be realized, which should possess superior performance to their pure energetic polymorphs.

4.4 Experimental Procedures

4.4.1 Materials

Acetonitrile (Certified ACS) was obtained from Fisher Scientific and dried over 4 Å molecular sieves. 2,4,6,8,10,12-Hexanitro-2,4,6,8,10,12-hexaazaisowurtzitane (CL-20) was used as received from Picantinny Arsenal. The concentrated 98% hydrogen peroxide (HP) was used as received from PeroxyChem LLC. ***Caution!*** *Although no unplanned detonations were encountered during this work, CL-20 is a dangerous high explosives and hydrogen peroxide is a strong oxidizing agent. Proper safety practices and equipment was used to prevent an explosion due to friction, heat, static shock, or impact. Be aware that the potential for severe injury exists if these materials are handled improperly.*

4.4.2 Crystallization

Both polymorphic solvates of CL-20 (**1** and **2**) were initially obtained from 1:1 acetonitrile/HP solutions, with a small amount (~5 mg) of CL-20 dissolved, by slow evaporation and then conditions for their pure growth was determined. Similarly, the hydrated form of α-CL-20 was obtained by slow evaporation by dissolving a small amount (~5 mg) of CL-20 in a 1:1 acetonitrile/DI H_2O solution. The orthorhombic solvate could be scaled up easily through the slow addition of HP to the solution of CL-20. The monoclinic solvate could be scaled up

conveniently with the use of solvent mediated transformation in a slurry of the pure components at room temperature, see below.

*2:1 CL-20/HP (**1**) monoclinic*

A 4 mL glass vial was loaded with 30 mg of ε-CL-20 (0.0685 mmol) which was dissolved in 300 µL of dry acetonitrile. To this was added 300 µL of concentrated H_2O_2 at which point the formation of thin plates of **1** was observed by optical microscopy. The vial was sealed/stirred gently for 15 minutes, before the crystal were collected. This solid was determined to be the 2:1 CL-20/HP orthorhombic solvate by both Raman spectroscopy and powder X-ray diffraction.

*2:1 CL-20/HP (**2**) monoclinic*

A 4 mL glass vial was loaded with 30 mg of ε-CL-20 (0.0685 mmol) which was dissolved in 200 µL of dry acetonitrile. To this was added 500 µL of concentrated H_2O_2 at which point a mixture of orthorhombic and monoclinic solvates was obtained. The vial was sealed/stirred gently for 4 days, during which time the orthorhombic CL-20/HP crystals had disappeared and only the monoclinic CL-20/HP remained by optical microscopy. This solid was determined to be the 2:1 CL-20/HP monoclinic solvate by both Raman spectroscopy and powder X-ray diffraction.

4.4.3 Raman Spectroscopy

Raman spectra were collected using a Renishaw inVia Raman Microscope equipped with a Leica microscope, 633 nm laser, 1800 lines/mm grating, 50 µm slit and a RenCam CCD detector. Spectra were collected in extended scan mode with a range of 100-4000 cm^{-1} and then analyzed using the WiRE 3.4 software package (Renishaw). Calibration was performed using a silicon standard.

4.4.4 Powder X-ray Diffraction (PXRD)

Powder X-ray diffraction patterns were collected on a Bruker D8 Advance diffractometer using Cu-Kα radiation (λ = 1.54187 Å) and operating at 40 kV and 40 mA. Samples were prepared by finely grinding and packing into the depression of a glass slide. The powder patterns were collected by scanning 2θ from 5° to 50° with a step size of 0.02° and a step speed of 0.5 seconds. The data was processed using Jade 8 XRD Pattern Processing, Identification & Quantification analysis software (Materials Data, Inc.).[30] The powder patterns were all compared to their respective simulated powder patterns from the single crystal X-ray diffraction structures and were found to be in significant agreement with the predicted patterns.

4.4.5 Single Crystal Structure Determination

Single crystal X-ray diffraction data for **1**, **2** and α-CL-20 were collected using a Rigaku AFC10K Saturn 944+ CCD-based X-ray diffractometer equipped with a low temperature device and Micromax-007HF Cu-target micro-focus rotating anode (λ = 1.54187 Å) operated at 1.2 kW power (40 kV, 30 mA). The X-ray intensities were measured at 85(1) K with the detector placed at a distance 42.00 mm from the crystal. The data was processed with CrystalClear 2.0 (Rigaku)[31] and corrected for absorption. The structures were solved and refined with the Bruker SHELXTL (version 2008/4)[32] software package using direct methods. All non-hydrogen atoms were refined anisotropically with the hydrogen atoms placed in a combination of refined and idealized positions. Funding for single crystal X-ray analysis was from NSF Grant CHE-0840456 for the Rigaku AFC10K Saturn 944+ CCD-based X-ray diffractometer.

CCDC 1495519, 1495520 and 1495521 contain the supplementary crystallographic data for this paper. These data are provided free of charge by The Cambridge Crystallographic Data Centre.

Table 4.1 Crystallographic Data for α-CL20 and CL-20 Solvates (Collected at 85 K)

Material	**α-CL-20**	**1**	**2**
Stoichiometry	4:1	2:1	2:1
Morphology	Plate	Rhombic	Polyhedron
Space Group	Pbca	Pbca	C2/c
a (Å)	9.4765(2)	9.4751(2)	28.4497(7)
b (Å)	13.1394(2)	13.1540(10)	8.9596(2)
c (Å)	23.3795(16)	23.4266(4)	12.7807(9)
α (°)	90	90	90
β (°)	90	90	113.397(8)
γ (°)	90	90	90
V0olume (Å^3)	2911.11	2919.79	2989.9
Z	8	8	8
ρ_{calc} (g/cm^3)	2.020	2.071	2.041
Data/Parameter	2669/287	2648/324	2696/312
R_1/wR_2	3.46/9.38	3.28/8.82	4.10/9.49
GOF	1.008	1.058	1.134

4.4.6 Differential Scanning Calorimetry (DSC)

Thermograms for each samples were recorded on a TA Instruments Q20 DSC equipped with a RCS90 chiller. All experiments were run in Tzero™ hermetic aluminum DSC pans under a nitrogen purge with a heating rate of 10 °C/min, while covering the temperature range of 40 °C to 300 °C. The instrument was calibrated using an indium standard. Thermograms were analyzed using TA Universal Analysis 2000, V 4.5A.

4.4.7 Thermogravimetric Analysis (TGA)

Thermograms for each samples were recorded on a TA Instruments Q50 TGA. All experiments were run in platinum TGA sample pans with a stainless steel mesh cover under a nitrogen purge of 50 mL/min with a heating rate of 10 °C/min, while covering the temperature range of 35 °C to 450 °C. The instrument was calibrated using the Curie points of alumel and nickel standards. Thermograms were analyzed using TA Universal Analysis 2000, V 4.5A.

4.4.8 Drop Weight Impact Sensitivity Analysis

For the analysis of the sensitivity to impact, approximately 2 mg (± 10%) of material for each sample is contained within nonhermetic DSC pans and then struck by a freefalling 5 lb drop weight. A reproducible Dh_{50}, height of the 50% probability of detonation, is obtained by utilizing the Bruceton Analysis (up-and-down method) with varying drop heights. For reference the Dh_{50} of ε-CL-20 and β-HMX are 29 and 55 cm, respectively.

4.5 References

1. Brittain, H. G., *Polymorphism in Pharmaceutical Solids*. Marcel Dekker, Inc.1999; Vol. 192.

2. Nikitina, E. V.; Starova, G. L.; Frank-Kamenetskaya, O. V.; Pevzner, M. S., 3,3'-Dinitro-5,5'-bi(1,2,4-triazole) dihydrate CIF. *Kristallografiya* **1982,** *27*, 485.

3. Haiges, R.; Belanger-Chabot, G.; Kaplan, S. M.; Christe, K. O., Preparation and characterization of 3,5-dinitro-1H-1,2,4-triazole. *Dalton Trans.* **2015,** *44*, 7586-7594.

4. Main, P.; Cobbledick, R. E.; Small, R. W. H., Structure of the fourth form of 1,3,5,7-tetranitro-1,3,5,7-tetraazacyclooctane ([gamma]-HMX), 2C4H8N8O8.0.5H2O. *Acta Crystallogr. Sect. C* **1985,** *41*, 1351-1354.

5. Nielsen, A. T.; Chafin, A. P.; Christian, S. L.; Moore, D. W.; Nadler, M. P.; Nissan, R. A.; Vanderah, D. J.; Gilardi, R. D.; George, C. F.; Flippen-Anderson, J. L., Synthesis of polyazapolycyclic caged polynitramines. *Tetrahedron* **1998,** *54*, 11793-11812.

6. Dippold, A. A.; Klapötke, T. M., Nitrogen-Rich Bis-1,2,4-triazoles—A Comparative Study of Structural and Energetic Properties. *Chem. Eur. J.* **2012,** *18*, 16742-16753.

7. Gao, H.; Shreeve, J. n. M., Azole-Based Energetic Salts. *Chem. Rev.* **2011,** *111*, 7377-7436.

8. Landenberger, K. B.; Matzger, A. J., Cocrystal Engineering of a Prototype Energetic Material: Supramolecular Chemistry of 2,4,6-Trinitrotoluene. *Cryst. Growth Des.* **2010,** *10*, 5341-5347.

9. Landenberger, K. B.; Matzger, A. J., Cocrystals of 1,3,5,7-Tetranitro-1,3,5,7-tetrazacyclooctane (HMX). *Cryst. Growth Des.* **2012,** *12*, 3603-3609.

10. Millar, D. I. A.; Maynard-Casely, H. E.; Allan, D. R.; Cumming, A. S.; Lennie, A. R.; Mackay, A. J.; Oswald, I. D. H.; Tang, C. C.; Pulham, C. R., Crystal engineering of energetic materials: Co-crystals of CL-20. *CrystEngComm* **2012,** *14*, 3742-3749.

11. *The oxygen balance for an organic material can be calculated using the following equation: -1600(2a + 0.5b - d)/MW, where a, b, c, d are the number of carbon, hydrogen, nitrogen and oxygen atoms, respectively, and MW is the molecular weight of the material.*

12. Lothrop, W. C.; Handrick, G. R., The Relationship between Performance and Constitution of Pure Organic Explosive Compounds. *Chem. Rev.* **1949,** *44*, 419-445.

13. Mustafa, A.; Zahran, A. A., Tetryl, Pentyl, Hexyl, and Nonyl. Preparation and Explosive Properties. *J. Chem. Eng. Data* **1963,** *8*, 135-150.

14. Bonifacio, S.; Festa, G.; Sorge, A. R., Novel Structured Catalysts for Hydrogen Peroxide Decomposition in Monopropellant and Hybrid Rockets. *J. Propul. Power* **2013,** *29*, 1130-1137.

15. Romantsova, O. V.; Ulybin, V. B., Safety issues of high-concentrated hydrogen peroxide production used as rocket propellant. *Acta Astronaut.* **2015,** *109*, 231-234.

16. Rusek, J. J., New decomposition catalysts and characterization techniques for rocket-grade hydrogen peroxide. *J. Propul. Power* **1996,** *12*, 574-579.

17. Gamage, N.-D. H.; Stiasny, B.; Stierstorfer, J.; Martin, P. D.; Klapotke, T. M.; Winter, C. H., Less sensitive oxygen-rich organic peroxides containing geminal hydroperoxy groups. *Chem. Commun.* **2015,** *51*, 13298-13300.

18. Gamage, N.-D. H.; Stiasny, B.; Stierstorfer, J.; Martin, P. D.; Klapötke, T. M.; Winter, C. H., Frontispiece: Highly Energetic, Low Sensitivity Aromatic Peroxy Acids. *Chem. Eur. J.* **2016,** *22*, 2582-2585.

19. Matyáš, R.; Pachman, J., Study of TATP: Influence of Reaction Conditions on Product Composition. *Propell., Explos. Pyrotech.* **2010,** *35*, 31-37.

20. Wierzbicki, A.; Salter, E. A.; Cioffi, E. A.; Stevens, E. D., Density Functional Theory and X-ray Investigations of P- and M-Hexamethylene Triperoxide Diamine and Its Dialdehyde Derivative. *J. Phys. Chem. A* **2001,** *105*, 8763-8768.

21. Landenberger, K. B.; Bolton, O.; Matzger, A. J., Two Isostructural Explosive Cocrystals with Significantly Different Thermodynamic Stabilities. *Angew. Chem. Int. Ed.* **2013,** *52*, 6468-6471.

22. Landenberger, K. B.; Bolton, O.; Matzger, A. J., Energetic-Energetic Cocrystals of Diacetone Diperoxide (DADP): Dramatic and Divergent Sensitivity Modifications via Cocrystallization. *J. Am. Chem. Soc.* **2015,** *137*, 5074-5079.

23. Pu, L.; Xu, J.-J.; Liu, X.-F.; Sun, J., Investigation on the Thermal Expansion of Four Polymorphs of Crystalline CL-20. *J Energetic Mater.* **2016,** *34*, 205-215.

24. Spek, A. L., PLATON SQUEEZE: a tool for the calculation of the disordered solvent contribution to the calculated structure factors. *Acta Crystallogr. Sect. C* **2015,** *71*, 9-18.

25. Bolton, O.; Matzger, A. J., Improved Stability and Smart-Material Functionality Realized in an Energetic Cocrystal. *Angew. Chem. Int. Ed.* **2011,** *50,* 8960-8963.

26. Bolton, O.; Simke, L. R.; Pagoria, P. F.; Matzger, A. J., High Power Explosive with Good Sensitivity: A 2:1 Cocrystal of CL-20:HMX. *Cryst. Growth Des.* **2012,** *12,* 4311-4314.

27. *Molecular volumes are calculated in Spartan14 V1.1.2 by determining the equilibrium geometry at the ground state for structures of the pure components with the semi-empirical AM1 method.*

28. Bennion, J. C.; McBain, A.; Son, S. F.; Matzger, A. J., Design and Synthesis of a Series of Nitrogen-Rich Energetic Cocrystals of 5,5′-Dinitro-2H,2H′-3,3′-bi-1,2,4-triazole (DNBT). *Cryst. Growth Des.* **2015,** *15*, 2545-2549.

29. *Cheetah 7.0 calculations were preformed utilizing the Sandia JCZS product library revision 32.*

30. Jade Plus 8.2 ed.: Materials Data, Inc., 1995-2007.

31. CrystalClear Expert 2.0 r12, Rigaku Americas and Rigaku Corporation (2011): Rigaku Americas, 9009, TX, USA 77381-5209, Rigaku Tokyo, 196-8666, Japan.

32. Sheldrick, G.M. SHELXTL, v. 2008/4; Bruker Analytical X-ray: Madison, WI, 2008.

Chapter 5: Conclusion

5.1 Summary of Work

Though considerable resources have been applied towards the synthesis of novel single component energetics, few materials have seen substantial scale up due to the rigorous requirements for performance, safety and economical production. As a result, many of the energetic compounds that are used by our military today are those established during WWII or well before. Early work in multicomponent energetic materials focused on the identification of molecular characteristics that would facilitate the formation of energetic cocrystals of non-energetic cocrystal formers and resulted in the discovery of many novel cocrystal of TNT, HMX and CL-20. While these materials all suffer from poor performance due to the underoxidation of their non-energetic components, the insight gained on the intermolecular interactions necessary for cocrystallization of energetic materials could now be broadly applied to many multi-energetic systems. The cocrystallization of two energetic materials has since been shown to produce materials that are now viable as high performance energetics. The work in this thesis focused on the multicomponent crystallization of a broad library of energetic materials (nitrobenzenes, azoles, and nitramines) in an effort to elucidate the types of intermolecular interactions that are feasible between various energetic components.

In Chapter two, three novel energetic cocrystals of DNBT (2:1 cocrystal of ANTA, a 1:1 cocrystal of DNPP, and a 2:1 cocrystal of 3,4-DNP) were discovered, all exhibiting the same hydrogen bonding motif in their structures. These three materials should be attractive ingredients for future explosive formulations. The DNBT cocrystals showcased the importance of crystal

engineering in energetic cocrystals and the potential for future development of reliable interaction for the formation of energetic cocrystals. The azole family of energetics has shown great promise as energetic cocrystal formers, and the synthon used for the formation of the three DNBT cocrystals will be a valuable tool for the design of additional cocrystalline materials of energetics.

In Chapter 3, two isostructural energetic cocrystals of TNB (2:1 cocrystals with TITNB and TBTNB) were discovered, whose formation relies on the same halogen bonding motif between the respective components. These halogen-containing cocrystals should be attractive ingredients for future munition formulations and have potential as insensitive biocidal materials. Computational evaluation of relative lattice energies played a vital role in guiding the experimental search for isostructural cocrystalline materials and predicts that a 2:1 cocrystal with TNB and TCTNB should exist if suitable synthesis conditions are discovered. Halogen bonding has been shown to be a useful and reliable crystal engineering tool with the formation of energetic cocrystals; a variety of halogen-containing energetics are already known and may offer additional scaffolds for the formation of cocrystalline materials.

In Chapter 4, two polymorphic energetic solvates (orthorhombic and monoclinic) comprised of 2:1 molar ratios of the high explosive CL-20 and the oxidizer HP were discovered and characterized. The hydrated form of CL-20, α-CL-20, was used as a guide for the synthesis of the two HP solvates, and indeed one solvate remains isostructural to α-CL-20. These solvates represent the first example of hydrogen bonding interactions between HP and the nitro moiety, and the approach will be useful for the formation of additional HP solvated materials. Calculated detonation parameters (velocity and pressure) of the two solvates are predicted to surpass the performance of all known forms of HMX and all low density forms of CL-20, with the

orthorhombic solvate even expected to exceed the properties of even ε-CL-20. The incorporation of HP into the crystal system allows for an easy and effective method for the improvement of the detonation properties, without the need for the development of new molecules. By utilizing existing hydrated energetic materials as a guide, the formation of additional isostructural HP solvates may be realized, which should possess superior performance to their pure energetic polymorphs.

This thesis sought to address the need for the development of reliable crystal engineering synthons for the development of novel multicomponent energetic systems. The three data chapters highlight the need for the discovery of strong intermolecular interactions between two energetic components through the formation of hydrogen and halogen bonding, and offer a promising route to novel energetic materials. Future work in the field will continue to focus on broadening the library of energetic materials available for multicomponent crystallization and the identification of the strong intermolecular synthons for the development of next generation energetic materials.

Appendices

Appendix A: Design and Synthesis of a Series of Nitrogen-Rich Energetic Cocrystals of 5,5'-Dinitro-2H,2H'-3,3'-bi-1,2,4-triazole (DNBT) Supplemental Information

Published: Bennion, J.C.; McBain, A.; Son, S.F.; Matzger, A. J., *Cryst. Growth Des.*, **2015**, *15*, (5), 2545-2549.

A1.1 Raman Spectroscopy of DNBT Cocrystals

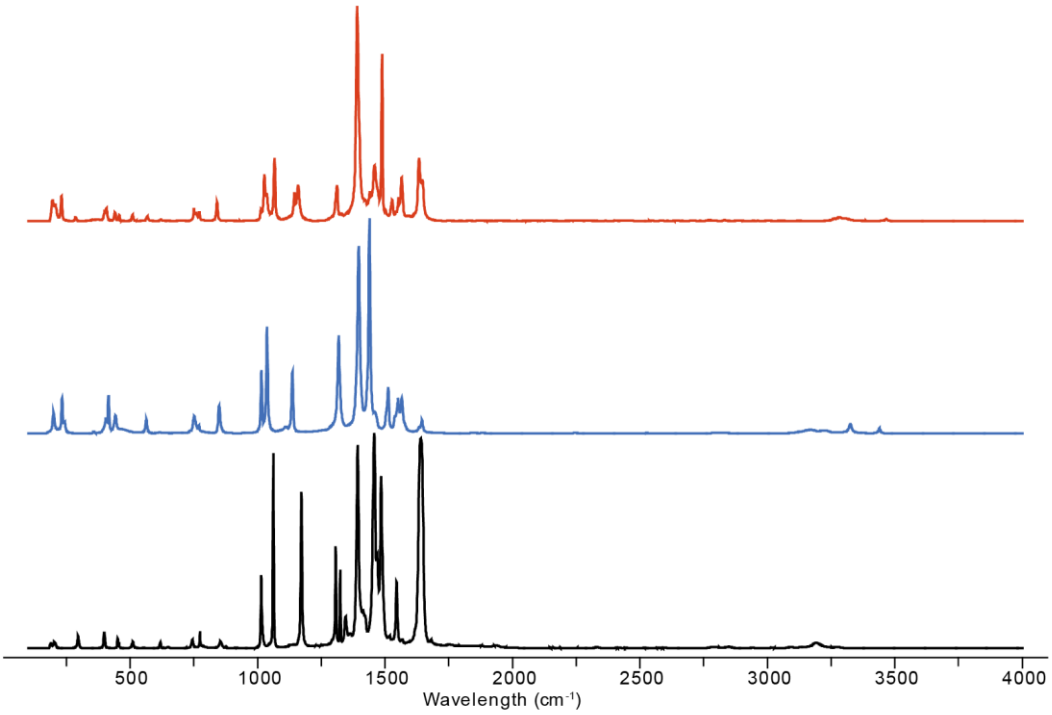

Figure A1.1 Raman spectra of **1**, α-ANTA and DNBT (from top to bottom).

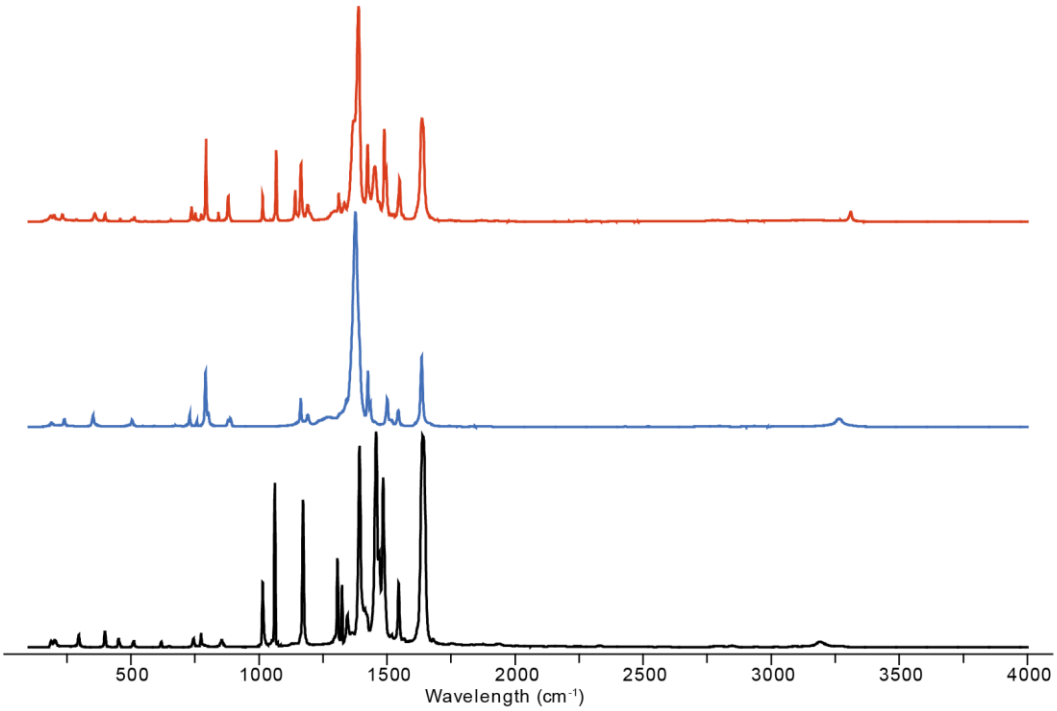

Figure A1.2 Raman spectra of **2**, DNPP and DNBT (from top to bottom).

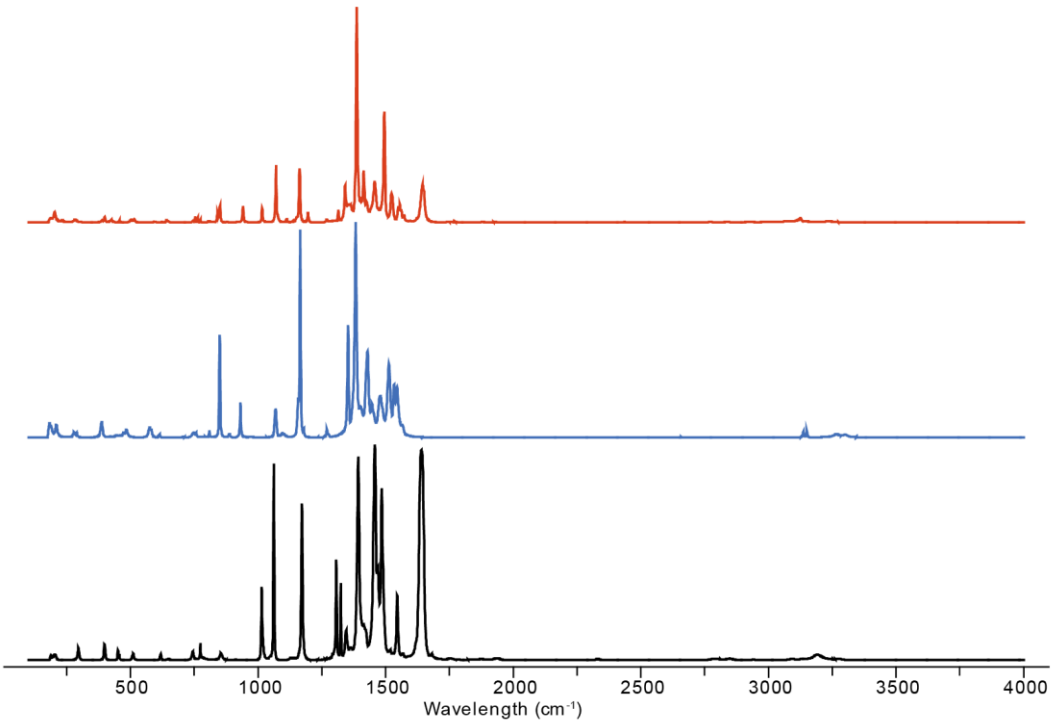

Figure A1.3 Raman spectra of **3**, 3,4-DNP and DNBT (from top to bottom).

A1.2 Powder X-ray Diffraction of DNBT Cocrystals

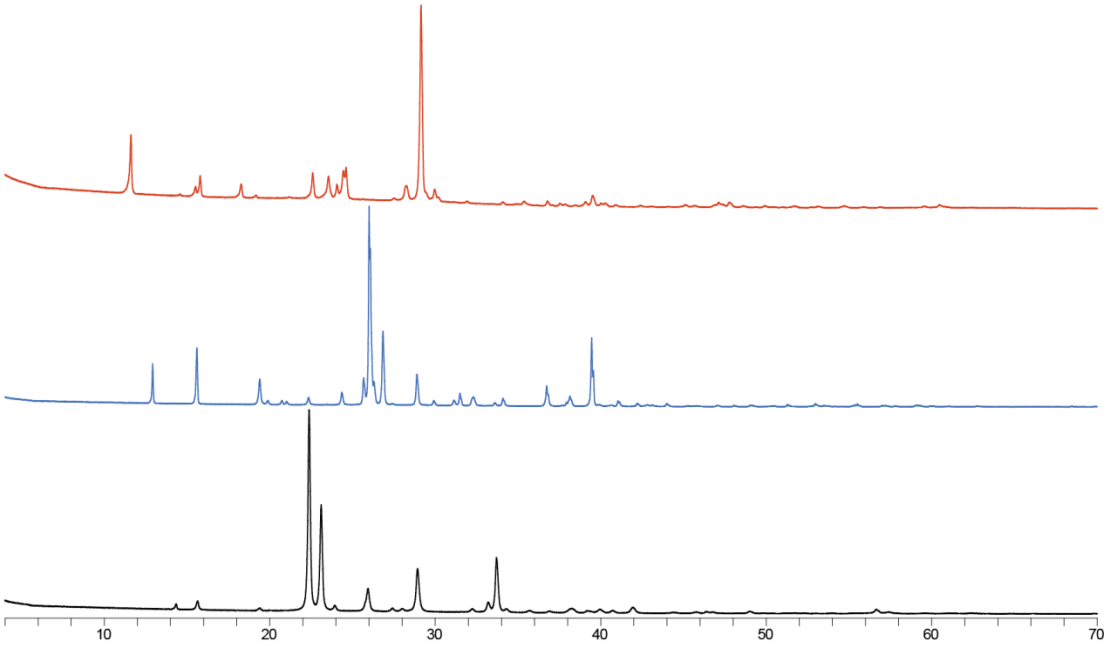

Figure A1.4 PXRD patterns of **1**, α-ANTA and DNBT (from top to bottom).

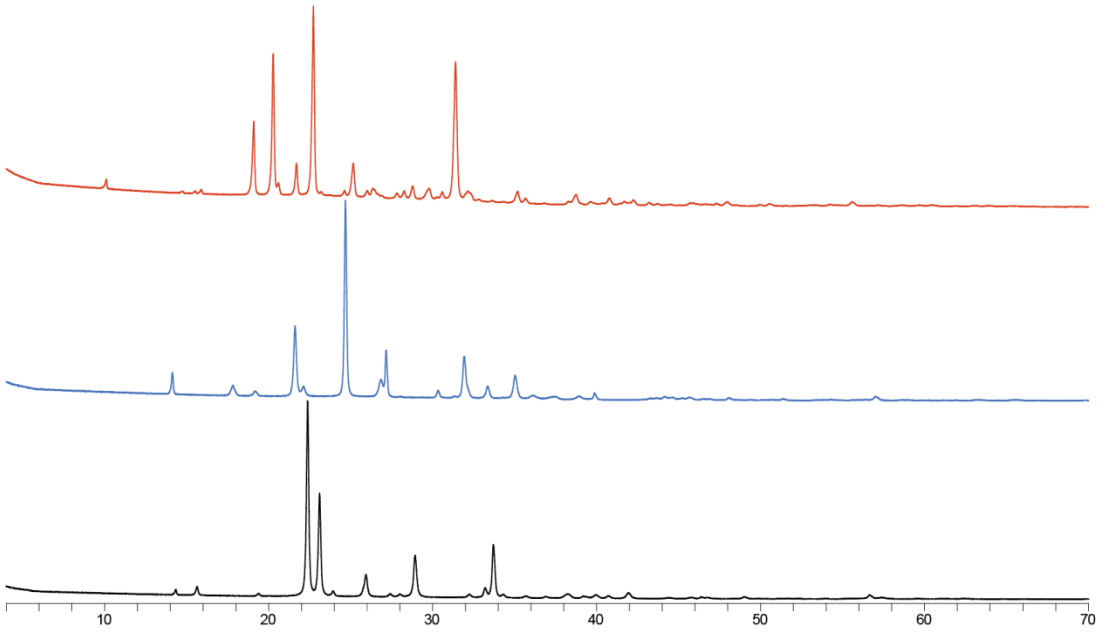

Figure A1.5 PXRD patterns of **2**, DNPP and DNBT (from top to bottom).

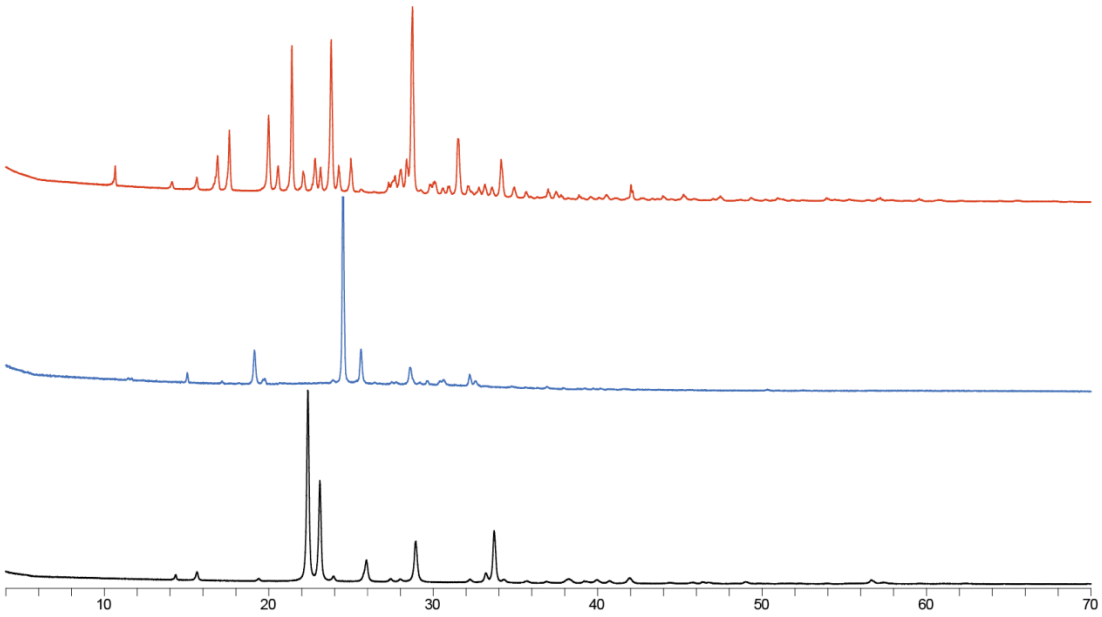

Figure A1.6 PXRD patterns of **3**, 3,4-DNP and DNBT (from top to bottom).

A1.3 ORTEP Diagrams of DNBT Cocrystals

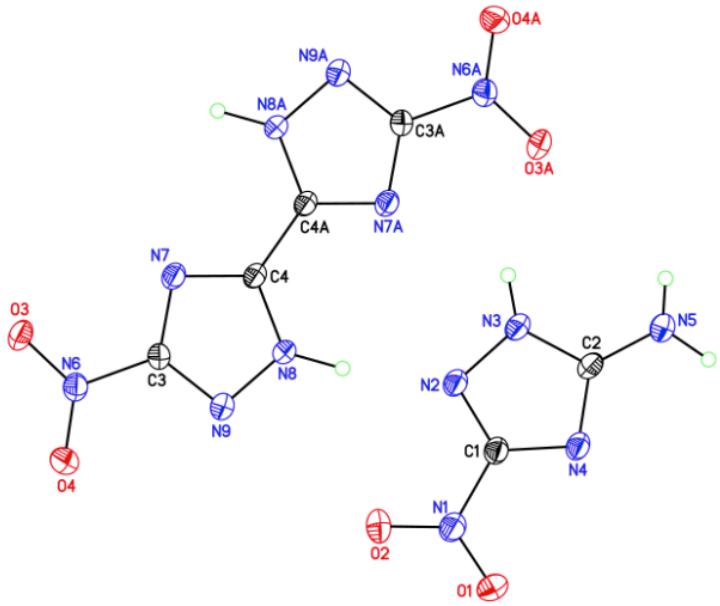

Figure A1.7 ORTEP diagram for **1** collected at 85 K with thermal ellipsoids of 50% probability.

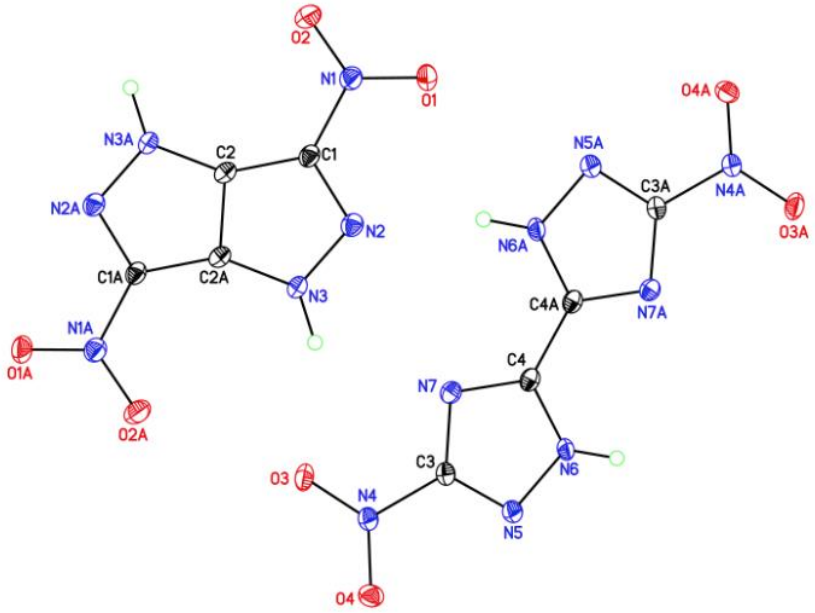

Figure A1.8 ORTEP diagram for **2** collected at 85 K with thermal ellipsoids of 50% probability.

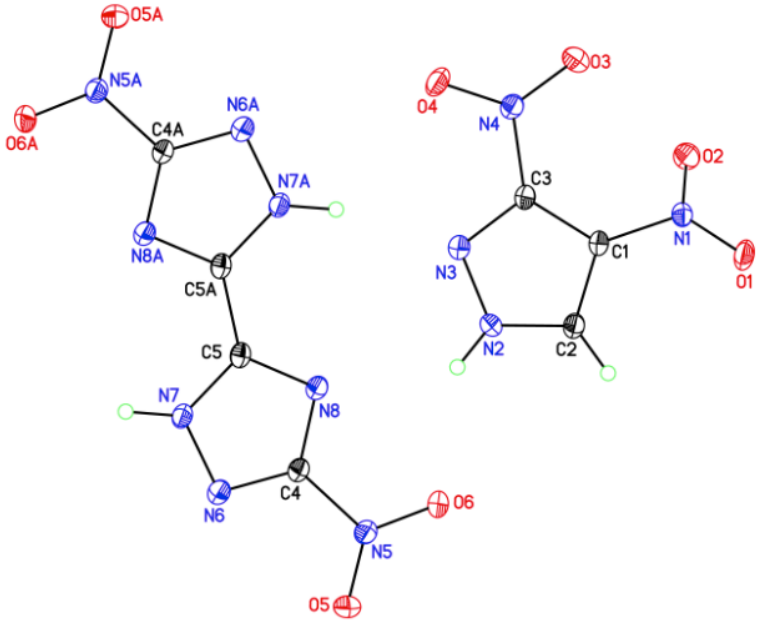

Figure A1.7 ORTEP diagram for **3** collected at 85 K with thermal ellipsoids of 50% probability.

A1.4 Differential Scanning Calorimetry of DNBT Cocrystals

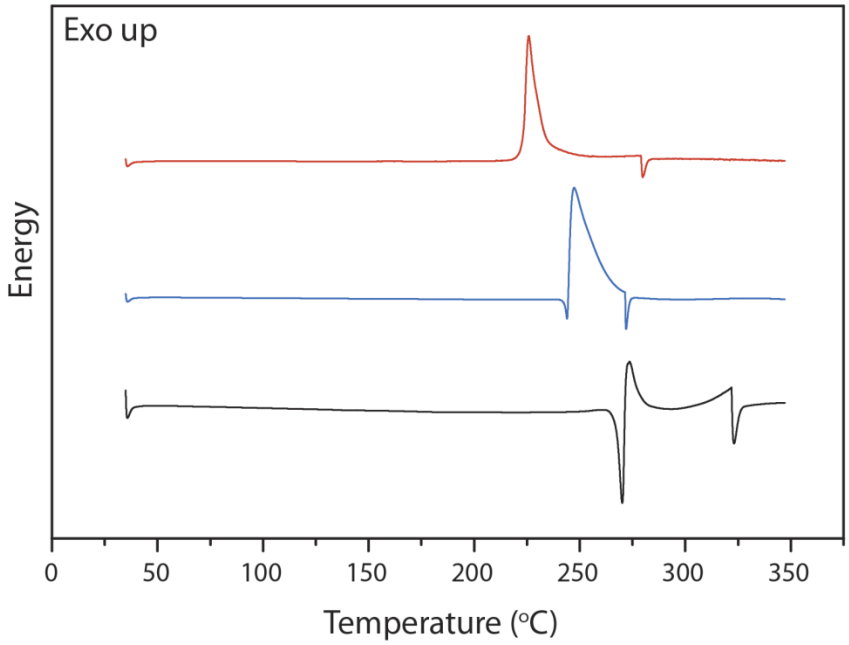

Figure A1.10 Typical DSC traces of **1**, ANTA and DNBT (from top to bottom).

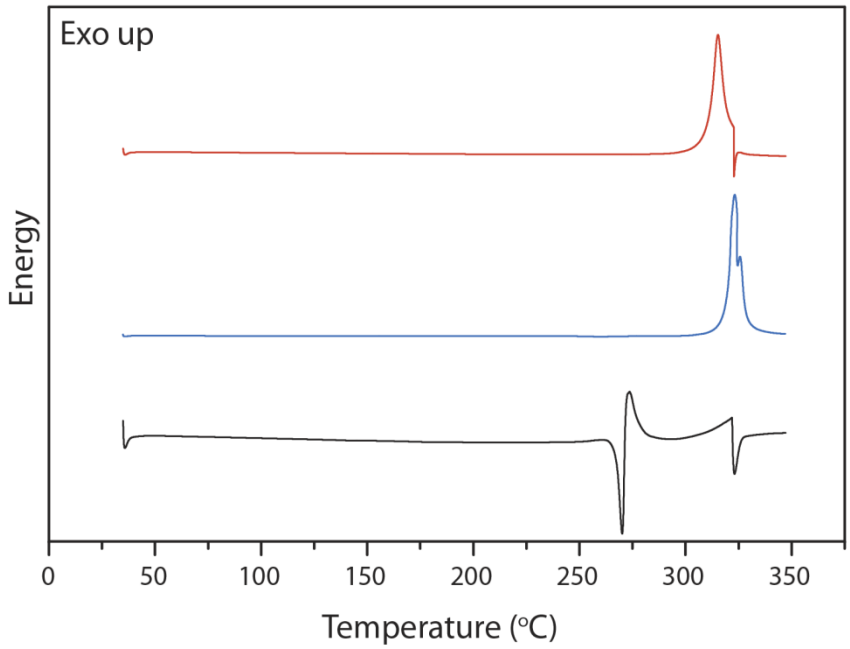

Figure A1.11 Typical DSC traces of **2**, DNPP and DNBT (from top to bottom).

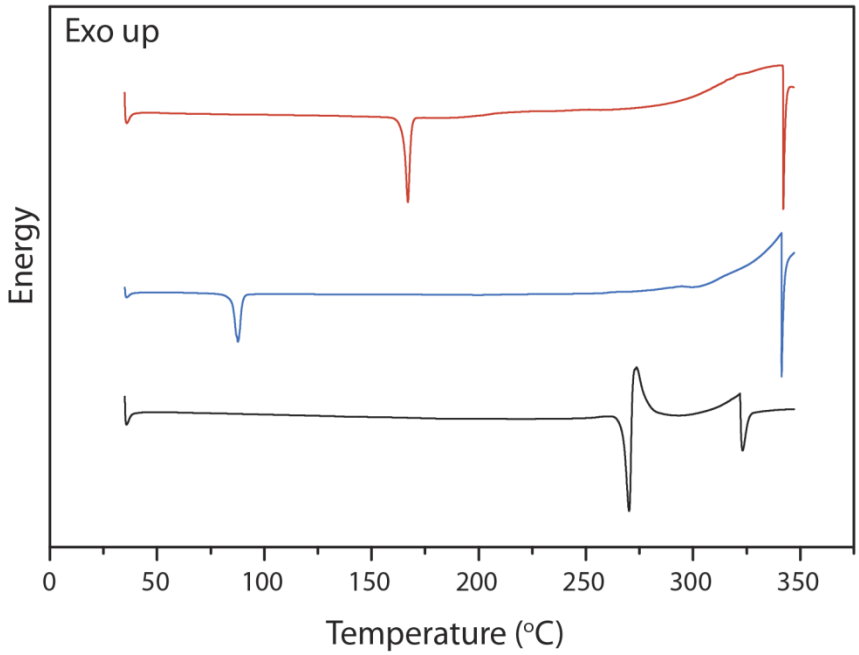

Figure A1.12 Typical DSC traces of **3**, 3,4-DNP and DNBT (from top to bottom).

Appendix B: Isostructural Cocrystals of 1,3,5-Trinitrobenzene Assembled by Halogen Bonding Supplemental Information

Published: Bennion, J.C.; Vogt, L.; Tuckerman, M.E.; Matzger, A. J., *Cryst. Growth Des.*, **2016**, *16*, (8), 4688-4693.

B1.1 Raman Spectroscopy of TNB Cocrystals

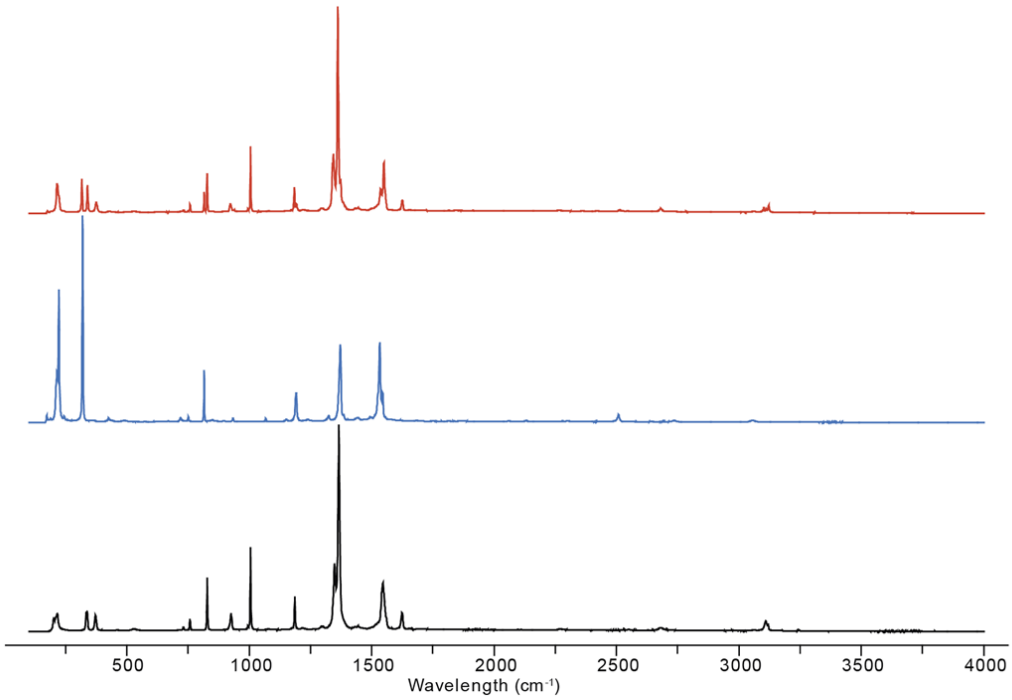

Figure B1.8 Raman spectra of **1**, TITNB, and TNB (from top to bottom).

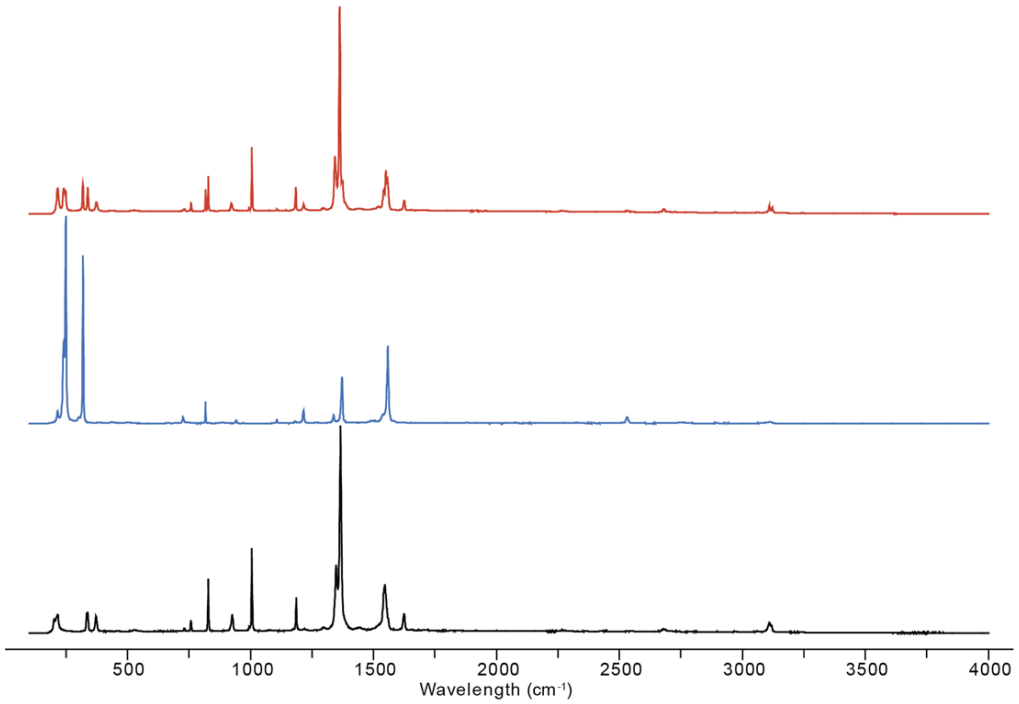

Figure B1.9 Raman spectra of **2**, TBTNB, and TNB (from top to bottom).

B1.2 Powder X-ray Diffraction Patterns of TNB Cocrystals

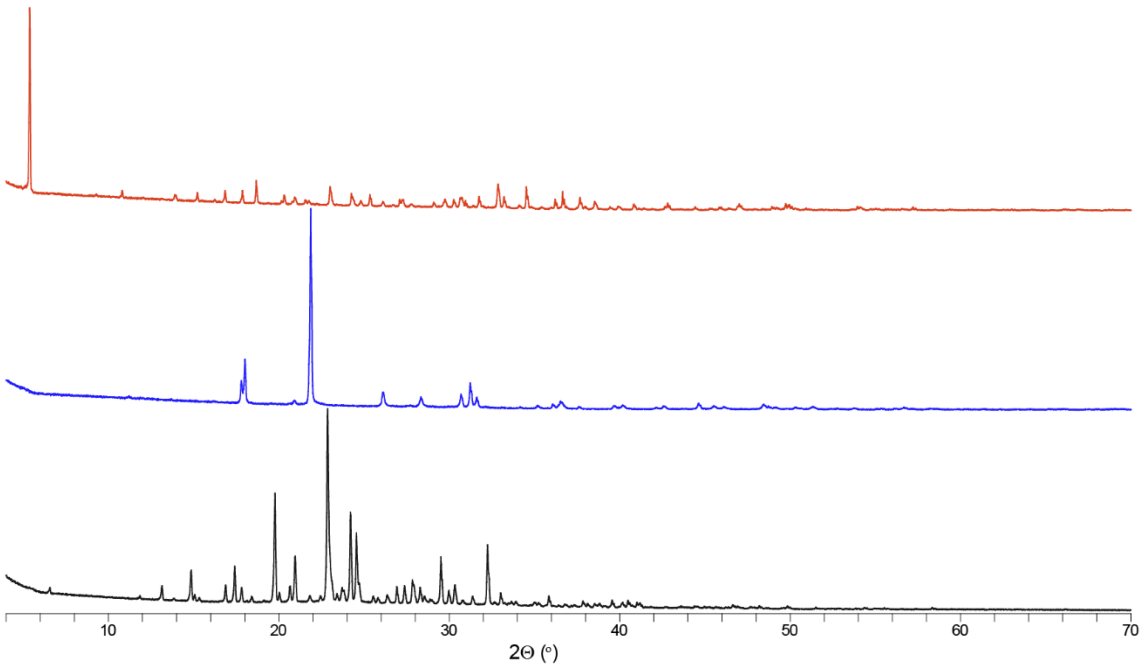

Figure B1.3 PXRD patterns of **1**, TITNB, and TNB (from top to bottom).

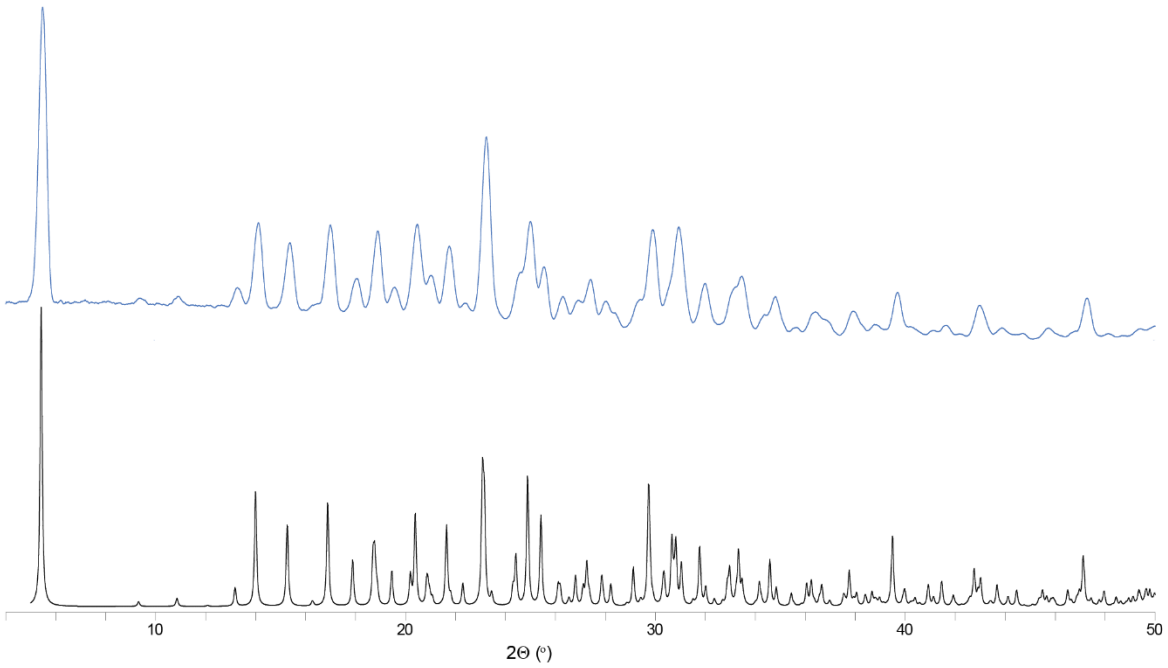

Figure B1.4 PXRD patterns of **1** and the simulated structure of **1** from the CIF (from top to bottom).

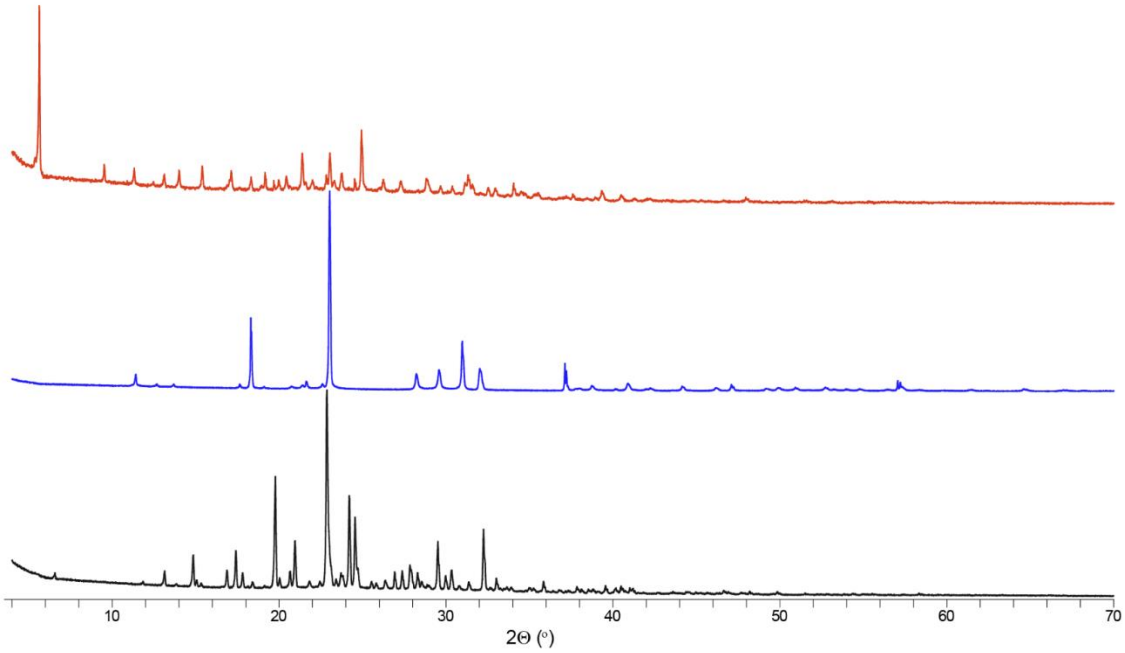

Figure B1.5 PXRD patterns of **2**, TBTNB, and TNB (from top to bottom)

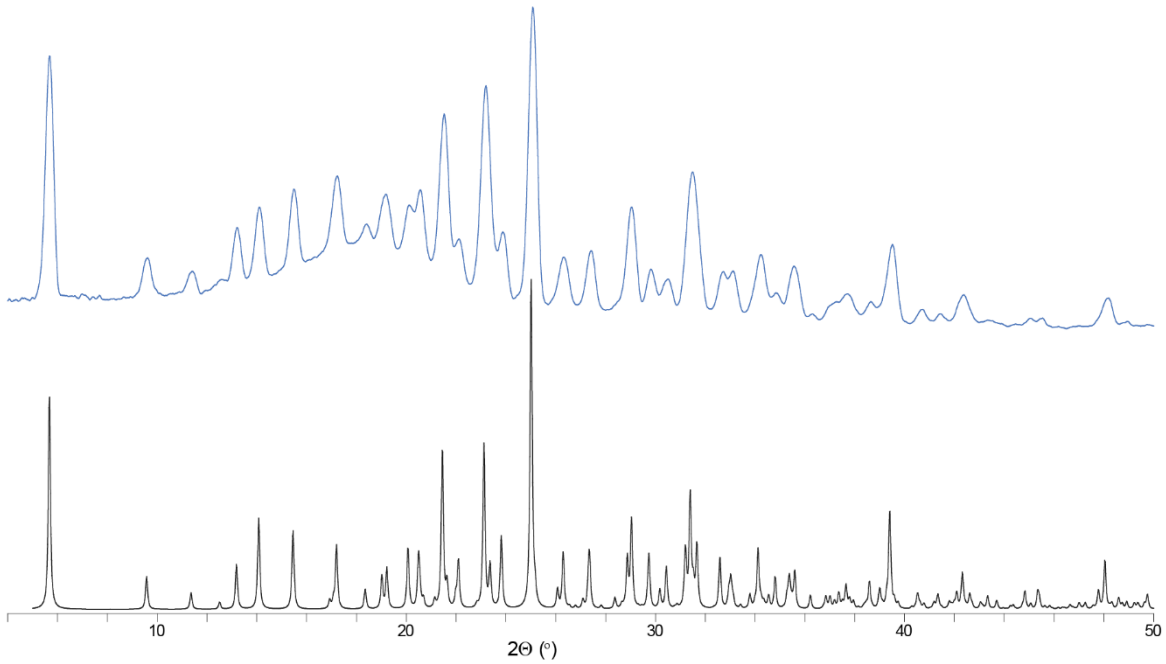

Figure B1.6 PXRD patterns of **2** and the simulated structure of **2** from the CIF (from top to bottom).

B1.3 ORTEP Diagrams of TNB Cocrystals

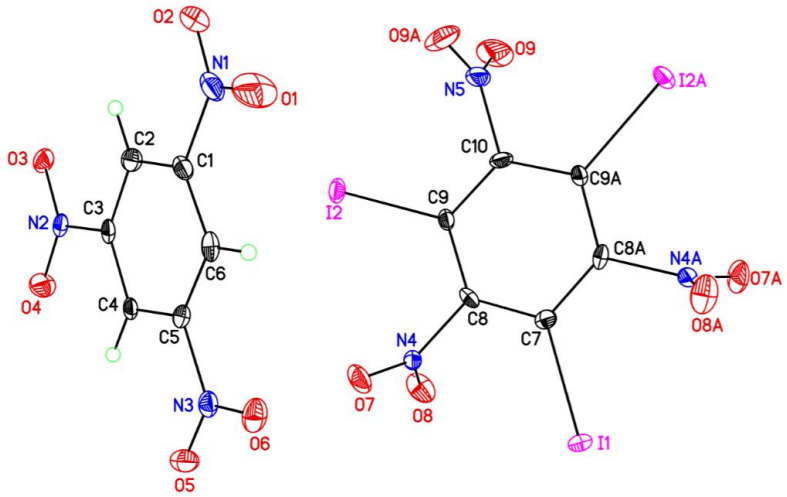

Figure B1.7 ORTEP diagram for **1** collected at 85 K with thermal ellipsoids of 50% probability.

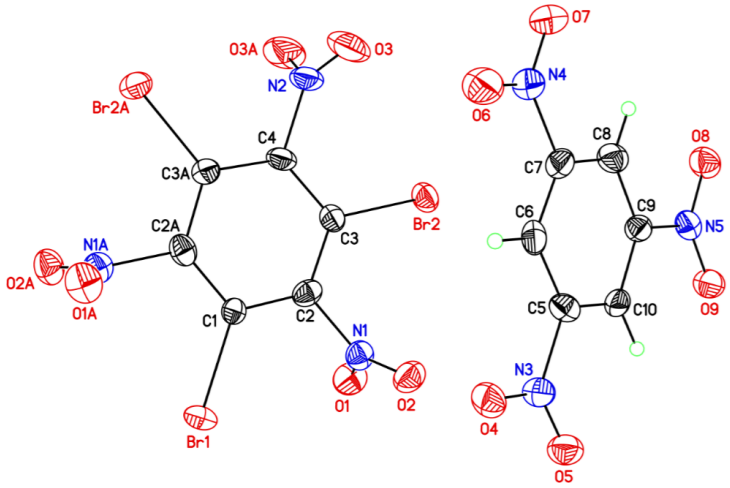

Figure B1.8 ORTEP diagram for **2** collected at 85 K with thermal ellipsoids of 50% probability.

B1.4 Differential Scanning Calorimetry of TNB Cocrystals

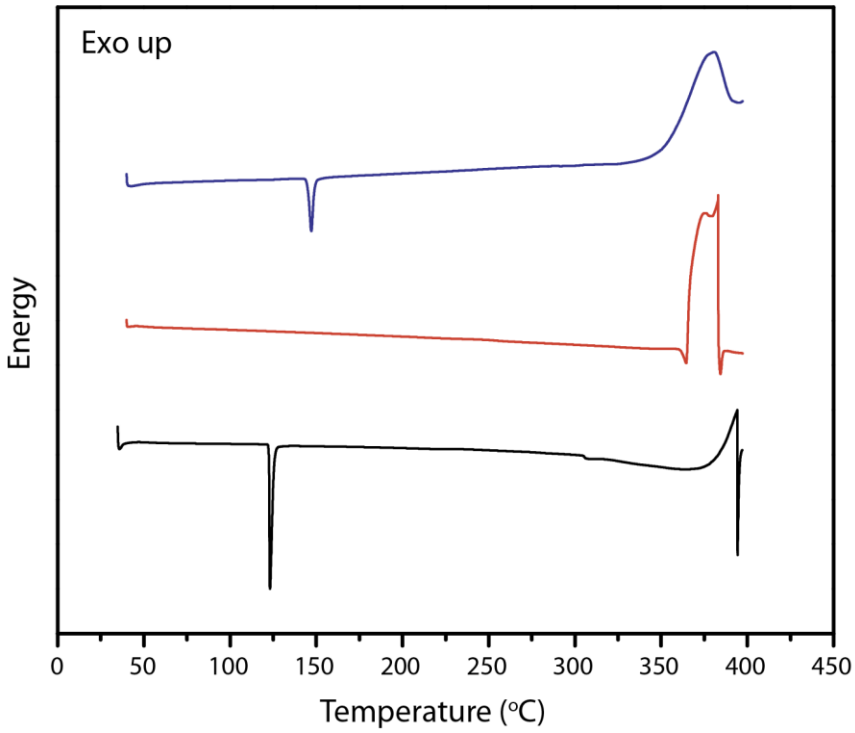

Figure B1.9 Typical DSC traces of **1**, TITNB, and TNB (from top to bottom).

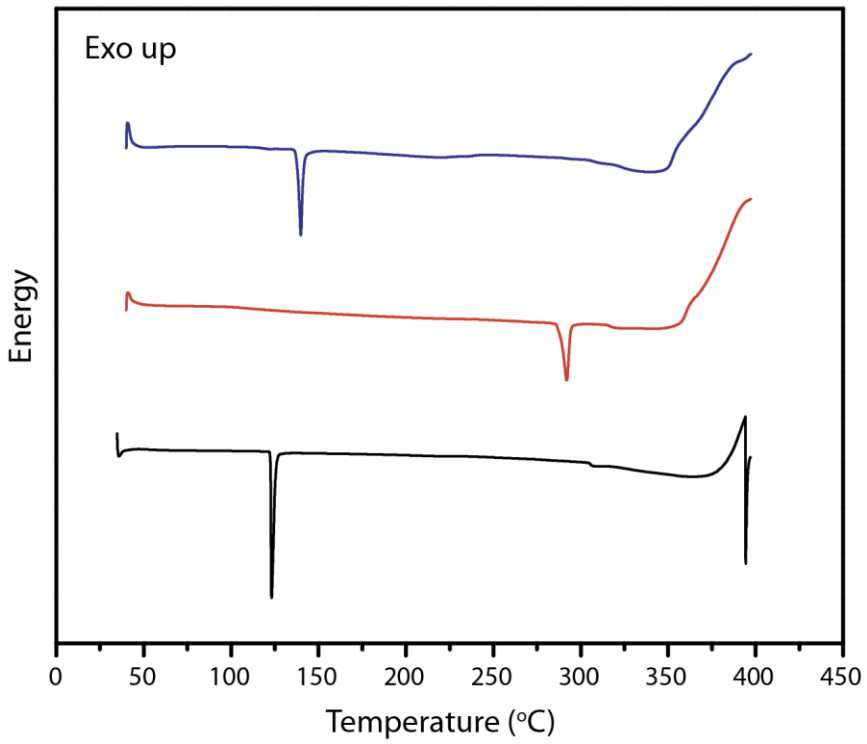

Figure B1.10 Typical DSC traces of **2**, TBTNB, and TNB (from top to bottom).

B1.5 Computational Optimizations of Unit Cells for TNB Cocrystals/Proposed Cocrystal and Coformers

Table B1.1 Optimized Cell Parameters for TNB Polymorphs

Cell parameters (Å, °)		**a**	**b**	**c**	**β**	**Molecular Volume (Å^3)**	**Relative Energy (kJ/mol)**
Form I	Observed [a]	12.587	9.684	26.860	90.0	204.6	
	Calculated [b]	12.800	9.781	27.113	90.0	212.2	+0.6
		(1.7%)	(1.0%)	(0.9%)	(0.0%)	(3.7%)	
Form III	Observed [a]	12.896	5.723	11.287	98.19	206.1	
	Calculated [b]	12.992	5.911	11.178	99.82	211.4	0.0
		(0.7%)	(3.3%)	(-1.0%)	(1.7%)	(2.6%)	

[a] Experimental structures from TNBENZ11 and TNBENZ13 for Form I and III, respectively.[1] [b] Relative deviations from experimentally observed values.

Table B1.2 Optimized Cell Parameters for TXTNB Crystals

Cell parameters (Å, °)		**a**	**b**	**c**	**α**	**β**	**γ**	**Molecular Volume (Å^3)**
TITNB	Observed [a]	*10.906*	*9.951*	*12.857*	*90.00*	*92.75*	*90.00*	*348.4*
	Calculated [b]	11.000	9.981	12.764	90.00	92.77	90.00	349.9
		(0.9%)	(0.3%)	(-0.7%)	(0.0%)	(0.0%)	(0.0%)	(0.4%)
TBTNB	Observed [c]	*10.042*	*9.625*	*12.572*	*90.00*	*94.83*	*90.00*	*302.7*
	Calculated [b]	9.941	9.719	13.122	90.00	93.16	90.00	316.4
		(-1.0%)	(1.0%)	(4.4%)	(0.0%)	(-1.8%)	(0.0%)	(4.5%)
TCTNB	Observed [d]	*12.137*	*12.181*	*11.694*	*100.39*	*100.10*	*78.02*	*274.4*
	Calculated [b]	12.014	12.284	12.062	101.11	100.31	79.39	282.9
		(-1.0%)	(0.8%)	(3.1%)	(0.7%)	(0.2%)	(1.7%)	(3.1%)

[a] Experimental structure from WUGVUR.[2] [b] Relative deviations from experimentally observed values. [c] Experimental structure from HUFXAJ.[2] [d] Experimental structure from WANMON.[3]

Table B1.3 Optimized Cell Parameters for TNB/TXTNB Cocrystals

Cell parameters (Å, °)		a	b	c	β
2:1 TNB/TITNB	Observed [a]	32.174	9.838	9.431	90.0
	Calculated [b]	32.540	9.918	9.611	90.0
		(0.9%)	(0.8%)	(1.9%)	(0.0%)
2:1 TNB/TBTNB	Observed [a]	30.451	9.601	9.752	90.0
	Calculated [b]	31.096	9.734	9.854	90.0
		(2.1%)	(1.4%)	(1.0%)	(0.0%)
2:1 TNB/TCTNB	Calculated	30.488	9.608	9.994	90.0

[a] Experimental structures reported in this work [b] Relative deviations from experimentally observed values.

Table B1.4 Calculated System Energy per Asymmetric Molecule Unit

System	(kJ/mol)
TNB Form I	-424460.24
TNB Form III	-424460.89
TITNB	-509850.88
TBTNB	-525288.18
TCTNB	-537685.14
2:1 TNB/TITNB [a]	-1358782.82
2:1 TNB/TBTNB [a]	-1374216.90
2:1 TNB/TCTNB [a]	-1386614.15

[a] Energy per asymmetric unit (2 TNB + 1 TXTNB)

B1.6 References

1. Thallapally, P. K.; Jetti, R. K. R.; Katz, A. K.; Carrell, H. L.; Singh, K.; Lahiri, K.; Kotha, S.; Boese, R.; Desiraju, G. R., Polymorphism of 1,3,5-Trinitrobenzene Induced by a Trisindane Additive. *Angew. Chem. Int. Ed.* **2004,** *43*, 1149-1155.

2. Landenberger, K. B.; Bolton, O.; Matzger, A. J., Energetic–Energetic Cocrystals of Diacetone Diperoxide (DADP): Dramatic and Divergent Sensitivity Modifications via Cocrystallization. *Journal of the American Chemical Society* **2015,** *137*, 5074-5079.

3. Gerard, F.; Hardy, A.; Becuwe, A., Structure of 1,3,5-trichloro-2,4,6-trinitrobenzene. *Acta Cryst. C* **1993,** *49*, 1215-1218.

Appendix C: Hydrogen Peroxide Solvates of 2,4,6,8,10,12-Hexanitro-2,4,6,8,10,12-Hexaazaisowurtzitane Supplemental Information

Published: Bennion, J.C.; Chowdhury, N.; Kampf,J.W.; Matzger, A. J., *Angew. Chem. Int. Ed.*, **2016**, *55*, 13118-13121.

C1.1 Powder X-ray Diffraction of CL-20 Solvates

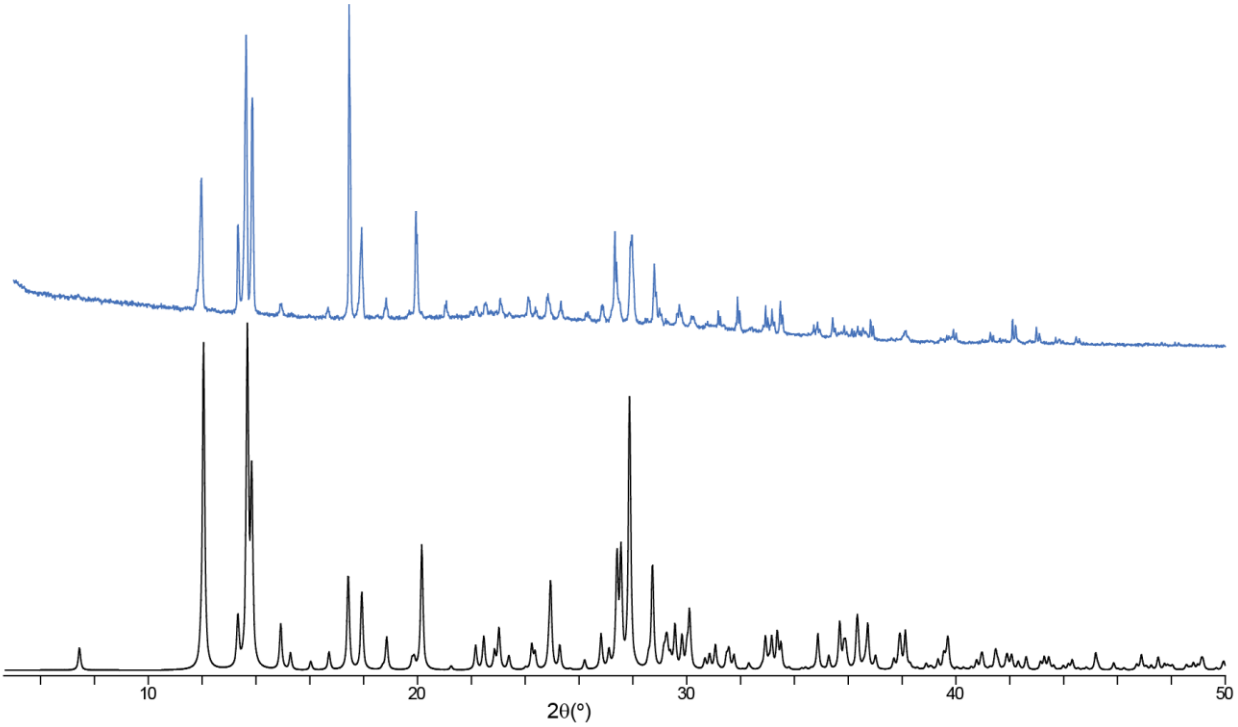

Figure C1.10 Powder patterns of **1** and the simulated structure of **α-CL-20** from the CIF (from top to bottom).

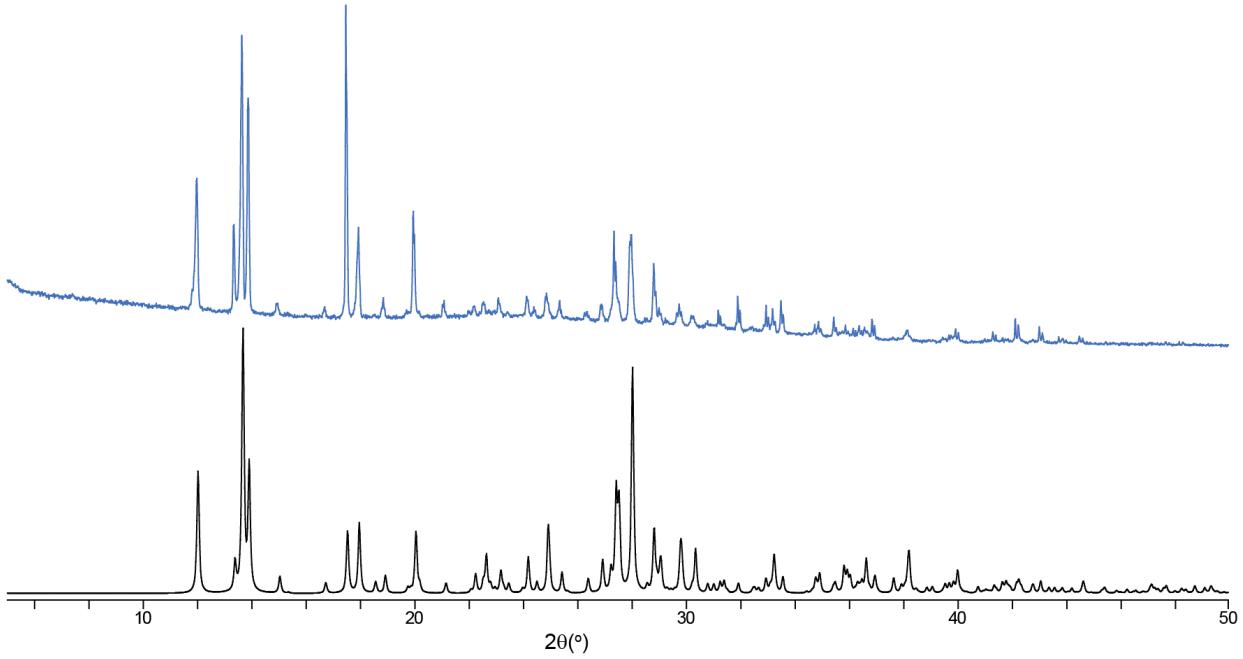

Figure C1.2 Powder patterns of **1** and the simulated structure of **1** from the CIF (from top to bottom).

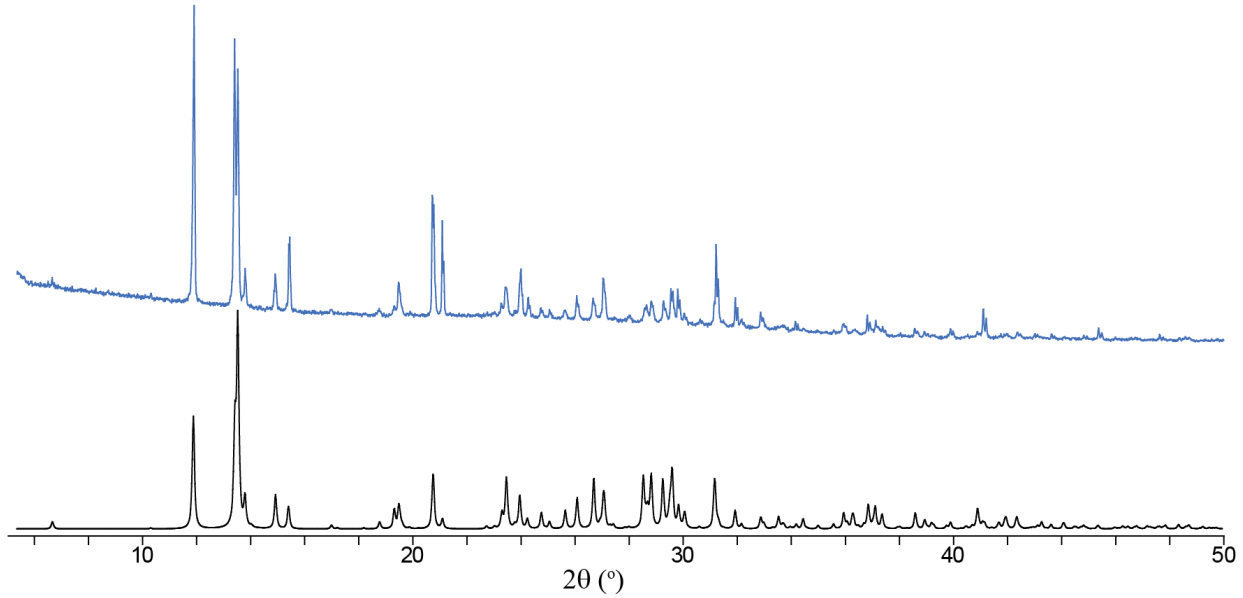

Figure C1.3 Powder patterns of **2** and the simulated structure of **2** from the CIF (from top to bottom).

C1.2 Raman Spectroscopy of CL-20 Solvates

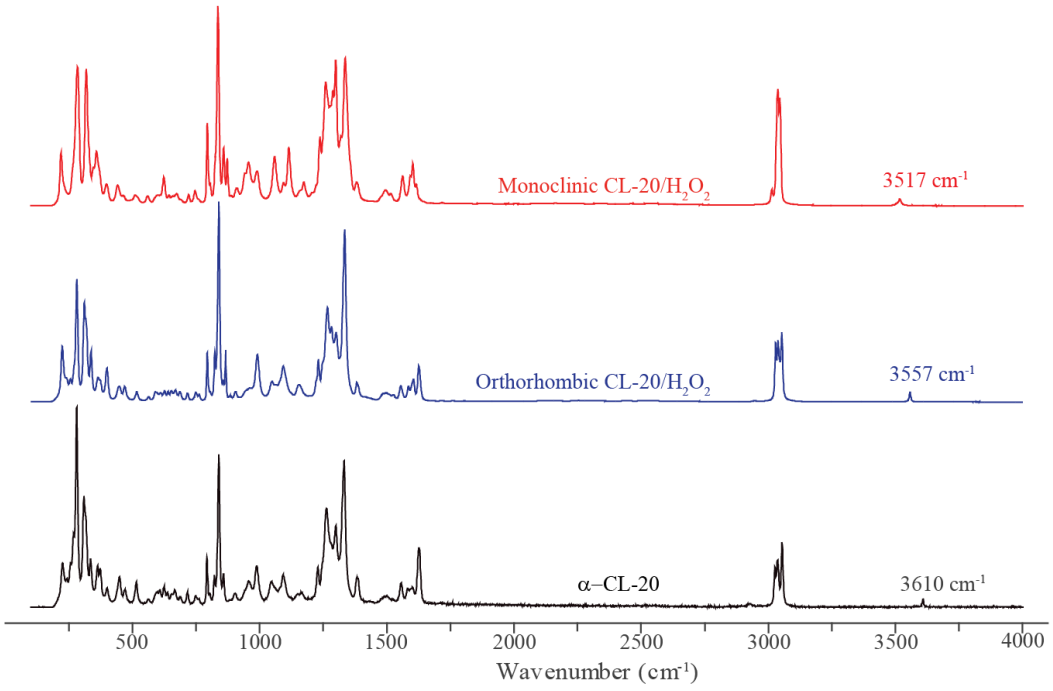

Figure C1.4 Full range (100-4000 cm^{-1}) Raman spectra of α-CL-20, **1** and **2** (from bottom to top).

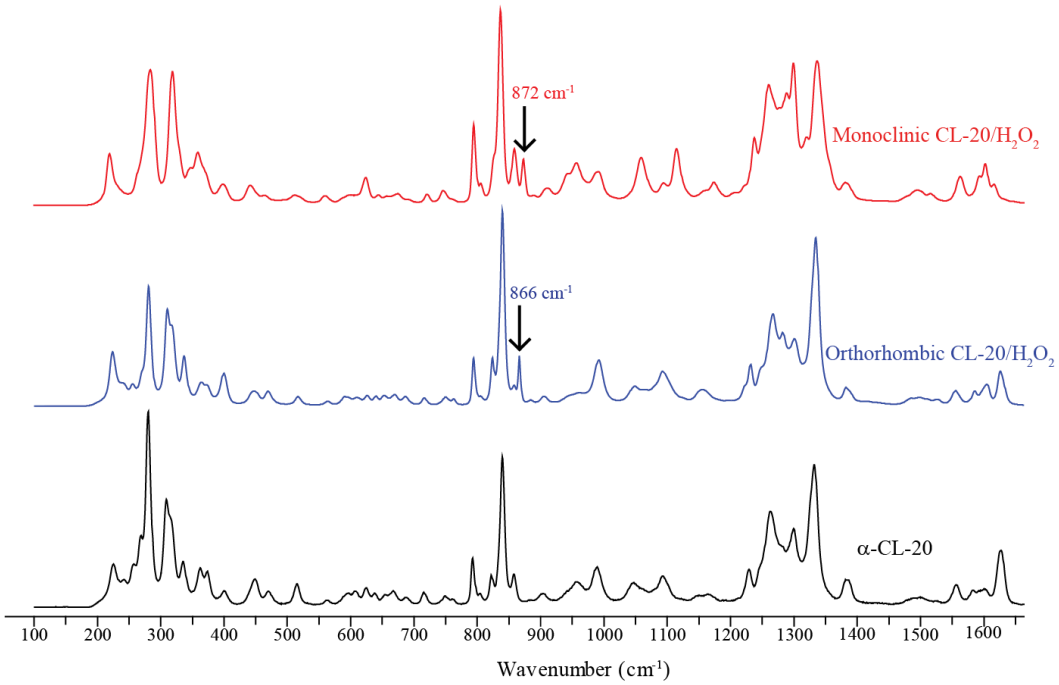

Figure C1.5 Zoomed in (100-1650 cm^{-1}) Raman spectra of α-CL-20, **1** and **2** (from bottom to top). Pure HP O-O peak is at 879 cm^{-1}.

C1.3 ORTEP Diagrams of CL-20 Solvates

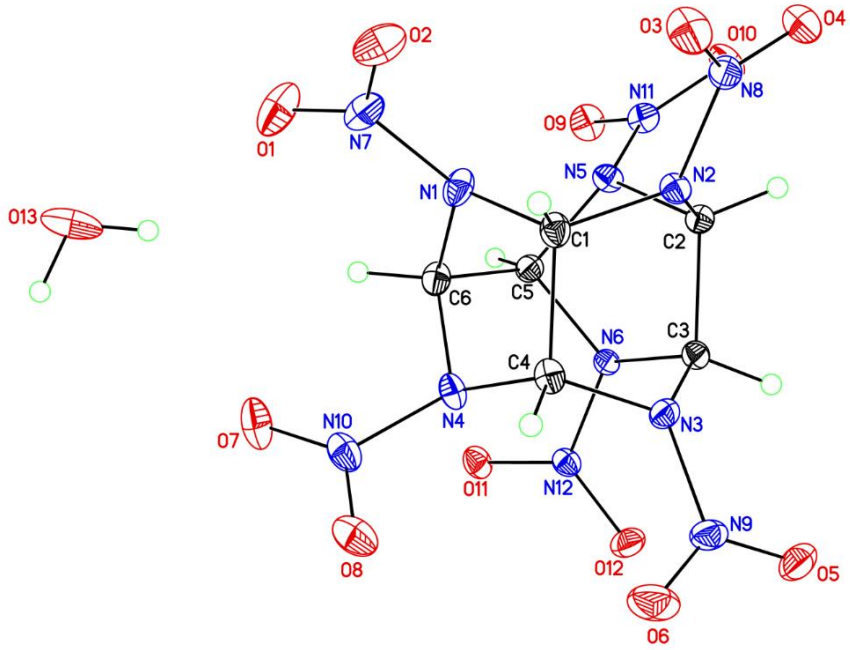

Figure C1.6 ORTEP diagram for **α-CL-20** collected at 85 K with thermal ellipsoids of 50% probability.

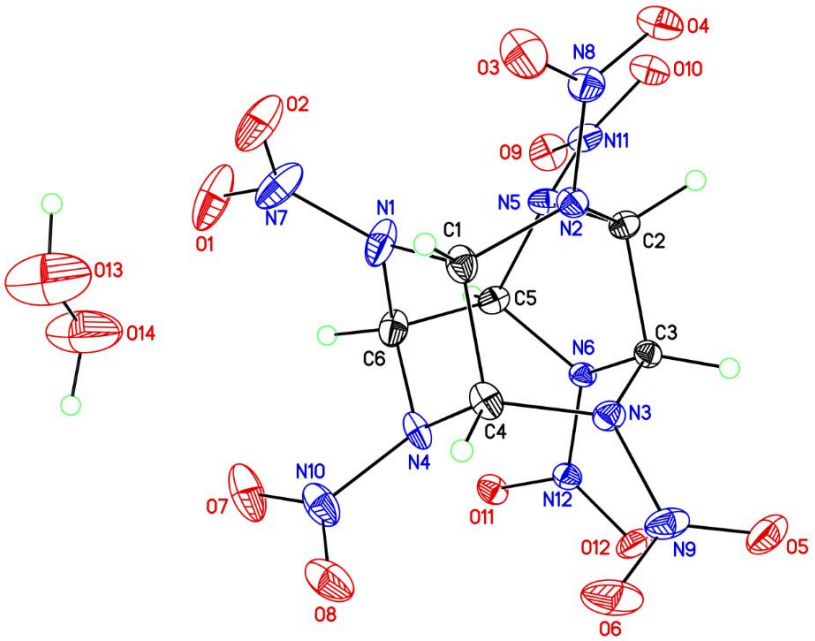

Figure C1.7 ORTEP diagram for **1**, orthorhombic, collected at 85 K with thermal ellipsoids of 50% probability.

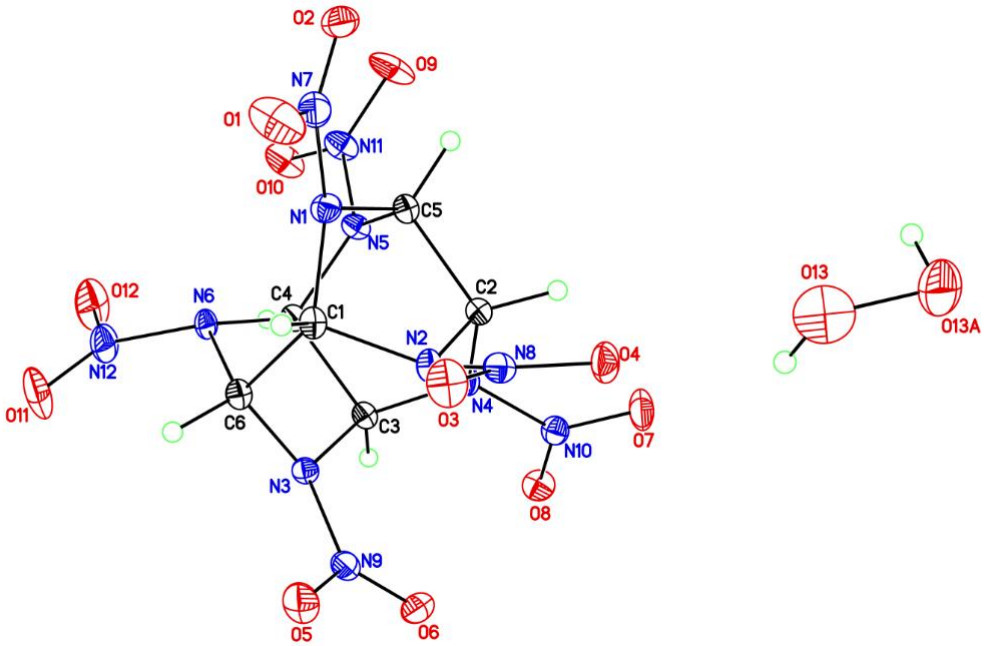

Figure C1.8 ORTEP diagram for **2**, monoclinic, collected at 85 K with thermal ellipsoids of 50% probability.

C1.4 Differential Scanning Calorimetry of CL-20 Solvates

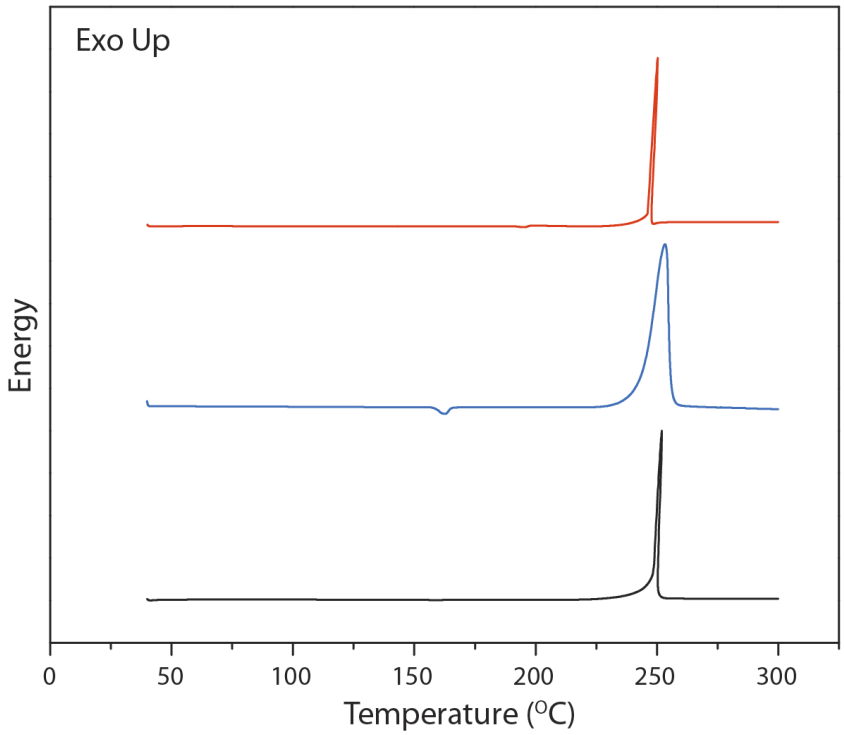

Figure C1.9 Typical DSC traces of α-CL20, **1** and **2** (from bottom to top).

C1.5 Thermogravimetric Analysis of CL-20 Solvates

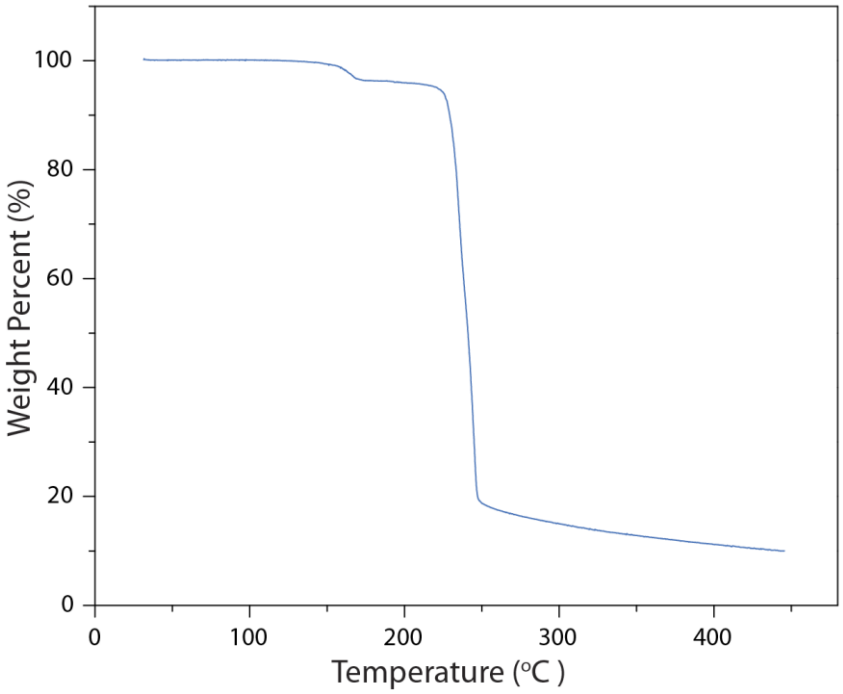

Figure C1.10 Typical TGA traces of **1**.

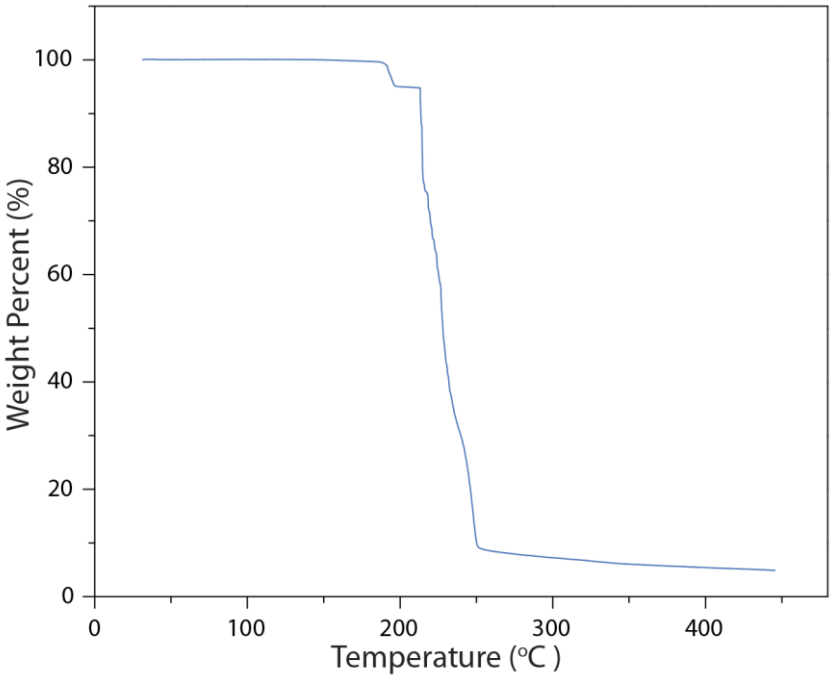

Figure C1.11 Typical TGA traces of **2**.